# Polymer NdFeB hard-magnetic scanner for Biomedical Scanning Applications

by

Manu Gopal Pallapa Venkataram

A thesis
presented to the University of Waterloo
in fulfillment of the
thesis requirement for the degree of
Doctor of Philosophy
in
Systems Design Engineering

Waterloo, Ontario, Canada, 2014

# AUTHOR'S DECLARATION

I hereby declare that I am the sole author of this thesis. This is a true copy of the thesis, including any required final revisions, as accepted by my examiners.

I understand that my thesis may be made electronically available to the public.

# Abstract

Micromirror scanners are the most significant of the micro-optical actuator elements with applications in portable digital displays, automotive head-up displays, barcode scanners, optical switches and scanning optical devices in the health care arena for external scanning diagnostics and in vivo scanning diagnostics. Recent development in microscanning technology has seen a shift from conventional electrostatic actuation to electromagnetic actuation mechanisms with major advantages in the ability to produce large scan angles with low voltages, remote actuation, the absence of the pull-in failure mode and the acceptable electrical safety compared to their electrostatic counterparts. Although attempts have been made to employ silicon substrate based MEMS deposition techniques for magnetic materials, the quality and performance of the magnets are poor compared to commercial magnets.

In this project, we have developed novel low-cost single and dual-axis polymer hard magnetic micromirror scanners with large scan angles and low power consumption by employing the hybrid fabrication technique of squeegee coating to combine the flexibility of polydimethylsiloxane (PDMS) and the superior magnetic performance of fine particle isotropic NdFeB micropowders. PCB coils produce the Lorentz force required to actuate the mirror for scanning applications.

The problem of high surface roughness, low radius of curvature and the magnetic field interaction between the gimbal frame and the mirror have been solved by a part PDMS-part composite fabrication process. Optimum magnetic, electrical and time dependent parameters have been characterized for the high performance operating conditions of the micromirror scanner. The experimental results have been demonstrated to verify the large scan angle actuation of the micromirror scanners at low power consumption.

# Acknowledgements

I would like to thank the people who have led me to reach this point in my career. My parents, my teachers, my family, my colleagues and my friends have shaped me into what I am and what I am able to do today. They have been a huge influence in my personal and academic development.

Firstly I would like to thank my supervisor Prof. John Yeow, who has given me the freedom to conduct research and has provided me with an unrestricted environment. His technical guidance and continuous support has been paramount in the culmination of this work. I am fortunate to have worked with him and hope to continue this relationship from which I have benefitted over the years of my doctoral studies. I would also like to thank my masters' supervisor Prof. Ash Parameswaran for his guidance during my masters and his valuable knowledge which has helped me throughout my doctoral studies.

I kindly thank my internal committee members, Prof. Nasser Lashgarian Azad, Prof. Eihab Abdel-Rahman and Prof. William Melek for providing me with positive feedback and support. I sincerely thank Prof. Siyuan He for agreeing to be the external examiner for my defense.

I would like to thank all my lab members particularly Yanhui Bai, Lawrence Wong, Mehdi Shahini, Morteza Ahmadi, So-Ra Chung, Sangtak Park, Shruti Nambiar, Albert Chen, Mohamed Aly Saad Aly, Zhenhao Li and Chen Hui.

I would also like to thank Kate Busse, Vicky Lawrence, Colleen Richardson, Kristen Deckert, Tariq Naqvi (late), Carrie Gilmour, Angie Muir, Mahindra Sangar, Orion Bruckman, Zivojin Pantic of the Systems Design Engineering staff who have been extremely helpful and supportive throughout these four years.

In regards to the work undertaken in this project, I would like to thank Mr. Jim Herchenroeder of Magnequench International Inc. for donating the MQFP-12-5 micropowder which is the critical part

of this work. Dr. Henry Lee and Yimin Zhou of the ECTI microfabrication cleanroom of Toronto who have been extremely accommodating innumerable times during my day long fabrication for the first generation micromirror.

I would also like to thank my friends Ajit Khosla, Plinio Morita and Shankar Raman Dhanuskodi who have given me moral support in difficult times. During my PhD I had the opportunity to be a teaching assistant of which I enjoyed every minute. I would like to thank my students who take the time to acknowledge me when I meet them in the buildings and hall ways.

My late mother and my father have been great role models to me and I must thank them for being unconditional in their love. I would also like to thank my brother and sister-in-law who have given me strength and support.

This acknowledgement is incomplete without the mention of my loving and caring wife, Shwetha Subramanya, to whom I owe a great deal. She has stood by me during both the happiness and hardships that I had to endure. Her understanding nature is second to none especially during my long and irregular working hours. She has filled me with light in the darkest sides of the moon which has given me that extra strength to achieve the goals that are fueled by my passion.

I would like to thank all those (my sincere apologies to those whose name I might have missed to mention) who have supported me in this journey.

# Dedication

To my parents

# Table of Contents

# List of Figures

# List of Tables

# Chapter 1: Introduction

## 1.1 Outline

This section presents the organization of the materials appearing in this thesis. Chapter 1 explains the motivation behind the work done in this project. Further the research objectives intended towards the progress of the project are discussed.

In Chapter 2, permanent magnetic materials are introduced with the focus on the advantages of permanent magnetic materials, the evolution of magnetic materials and the magnetic force principles relevant to the development of magnetic microactuators. Further, the prior art in electromagnetic scanners is reported and their limitations are discussed.

In Chapter 3, polymer magnetic actuators based on magnetic filler materials are introduced. The conventional and hybrid techniques involved in the fabrication of polymer magnetic actuators are discussed. This is followed by the reporting of the prior art performed in the fabrication of polymer composite magnetic films and magnetic actuators.

In Chapter 4, the design and fabrication of the polymer hard magnetic scanner used in this work is detailed. Critical conditions affecting the fabrication of good polymer magnetic films, the fabrication process flow in regards to the three designs of the polymer hard magnetic micromirror and the designs of the planar actuating microcoils is presented. The method of integration of the polymer hard magnetic mirror and the planar actuating microcoils is discussed.

In Chapter 5, the experimentation performed for the magnetic measurements of the microcoils and magnets, the elastic measurements of the polymer composite material and the surface roughness measurements are presented. In addition the simulations performed to determine the microcoil magnetic field and the resonant frequencies of the micromirror designs are also presented.

In Chapter 6, the results of the magnetic, mechanical, elastic and surface roughness experiments that were performed are presented. Analysis of the experimental results in regards to the magnetic and mechanical performance of the single axis and dual axis micromirror scanner is reported.

In Chapter 7, the summary of the work done is discussed along with the limitations and challenges faced in the duration of the project. Further, the future work to be undertaken in order to optimize the system for the integration into a biomedical scanning instrument is proposed.

## 1.2 Motivation

Micro mirror scanners are integrated into various systems such as barcode scanners, projection devices, smart-phones and more importantly into biomedical devices for optical scanning. While these micro actuators are chosen for their miniature sizes, the actuation is a critical figure of merit. In microscanners this figure of merit is characterized by the scan angle. A higher scan angle implies a wider range of scanning. In addition a low power consumption device is also an important requirement. Typical scanning mirrors are actuated by electrostatic actuation due to established fabrication techniques. There are critical flaws in the electrostatic actuator system for micromirror scanners such as pull-in and the necessity of high voltages in the range of hundreds of volts. Due to the scaling laws of magnets, miniature magnetic actuators offer high actuation displacement with moderate power consumption, no pull-in failure mode and the added advantage of long range actuation compared to similar scanners actuated via electrothermal, electrostatic or piezoelectric phenomenon.

Polymer composites based on permanent magnetic bonded powders exhibit immense potential for applications in microactuators and sensors with magnetic performances comparable to their fully dense counterparts. While fabrication and integration of magnetic devices based on bonded magnetic

powders is challenging via conventional deposition and electrochemical growth techniques, hybrid fabrication offers a promising alternative.

The core motivation of the work done in this project is to develop a polymer hard magnetic mirror that combines the high magnetic performance of permanent hard magnetic bonded powders and flexibility of polymers to result in a micromirror with large actuation and low power consumption. The attributes of this scanner will include bidirectional actuation, high energy density for large angular displacement, low power consumption with low heat dissipation, simple fabrication and acceptable electrical safety.

## 1.3 Research Objectives

The research objectives defined to develop a polymer hard magnetic mirror combining the high magnetic performance of permanent hard magnetic bonded powders and flexibility of polymers are as follows:

- To identify the magnetic micropowder with high magnetic performance and the polymer matrix with high elasticity and inter-compatibility
- To develop a low cost fabrication process for polymer magnetic actuators without the use of expensive patterning and deposition techniques.
- To manufacture master molds via standard lithography (silicon) and laser ablation (Plexiglas)
- To develop a low-cost polymer magnetic composite with high magnetic performance properties, high volume loading ability and ease of deposition into the master molds.
- To design and test magnetic and electrical parameters of various configuration excited planar microcoils

- To determine surface roughness and radius of curvature characteristics of the micromirror scanner to ensure good optical performance.
- To experimentally determine the static and dynamic operating modes for the single and dual-axis micromirror scanners

## 1.4 Contributions

The outcomes and the contributions of the research are listed as follows

- The development of a low-cost fabrication process to manufacture hard magnetic polymer microactuators based on PDMS and isotropic bonded NdFeB micropowder using the hybrid fabrication technique of squeegee coating micromolding.
- The development of an all polymer magnetic structural micromirror scanner with single and dual axis actuation feature with large scan angle and low power consumption.
- The mitigation of the high surface roughness and low radius of curvature problem using a surface modification technique based on the micropipetting of undoped PDMS.
- The reduction of the inter-magnetic influence emerging from the close proximity of the magnetic structures by developing a part-PDMS part-polymer composite fabrication technique for the dual axis micromirror scanners.
- The experimental comparison of the single axis no gimbal micromirrors, single axis outer frame micromirrors with and without the magnetic frame and dual axis outer frame inner gimbal micromirrors with and without the magnetic frame in regards to their static and dynamic responses for scanning applications.

# Chapter 2: Permanent Magnets and Actuators

## 2.1 Permanent Magnetic Materials for Microactuators

Microelectromechanical systems have brought about a revolution in the miniaturization of machines, sensing equipment, medical diagnostics and lab work, energy harvesters, robotic automation and space applications. The current trends suggest micromechanical systems pervading into many terrestrial and extra-terrestrial fields and applications. The typical mechanisms for MEMS actuators and sensors are electrostatic [1], piezoelectric [2], electrothermal [3], electromagnetic [4], magnetostrictive [5], pneumatic [6] and hydraulic [7]. The advantages of MEMS based sensors and actuators are heralded by batch fabrication and miniaturization. Miniaturization reduces effective power consumption in actuators and improves sensitivity in sensors since lower surface area or volumes result in faster reactions due to chemical dynamics. Although a lot of focus is shown on electrostatic, thermal and piezoelectric principles for sensing and actuation, the use of magnetic MEMS is not popular. The critical reason behind this as mentioned by Guckel [8] is that although magnetic MEMS possess immense potential, the fabrication and integration of magnetic MEMS present major challenges. Several researchers have built upon a strong case by using a variety of magnetic materials, innovative and efficient designs to propagate the use of magnetics in MEMS in the development of magnetic microactuators and microsensors [9-27]. While magnetic MEMS fabrication and integration have a lot of magnetic material contenders, better sensors and actuators are designed with materials with higher magnetic performance properties. The best magnetic properties are of hard magnetic materials or commonly known as permanent magnetic materials.

The prime advantage of permanent magnets is the inherent energy that they possess. While typical energy sources are drained with continuous use, such as batteries, the energy of a hard magnet is not depleted as no net-work is done by a magnet on its surroundings because of its open circuit operation.

The hard magnetic actuation technique asserts its dominance in large gap applications due to its ability to generate large forces. As the force generated for actuation is wireless or tetherless, the actuators can be deployed in harsh and hazardous environments due to their robustness [28]. Although typical macro controllers and drivers to actuate magnetic actuators are available on-the-shelf and are low cost, miniaturization of the magnetic devices allows assimilation into various fields where small size and geometry are critical factors for integration. Of particular interest to microactuators is that permanent magnetic devices typically possess low voltage actuation, generation of constant magnetic field without heat dissipation and most importantly there is no external power requirement to produce a constant magnetic field.

The performance of all magnetic materials (soft or hard) is associated with four major figures of merit. These are the (1) *remanence Br* or the measure of the remaining magnetization of the magnet when the driving field is dropped to zero, the (2) *coercivity Hc* which is the measure of the demagnetizing or reverse field needed to drive the magnetization of the magnet to zero, the (3) *energy product* which is the product of the remanence and the coercivity and the (4) *temperature stability* of the magnet which reflects the processing temperatures. The temperature defines the operating temperature and the maximum temperature that the magnet can sustain after which the magnetic domains cease to exist and remagnetization will not revive the magnet. This maximum temperature before demagnetization is the Curie temperature of the magnet [29].

These figures of merit are typically illustrated in a hysteresis loop (Figure 2-1), which is a multivalued plot of the magnetization and demagnetization of a magnet. Of particularly importance is the second quadrant which is known as the demagnetization curve. The values of $H_c$ and $B_r$ and the shape of this curve determine the usefulness of a material as a permanent magnet. The largest

rectangle under the demagnetization curve represents the maximum energy product of the magnet which is considered to be the best single index of quality of a permanent magnet material.

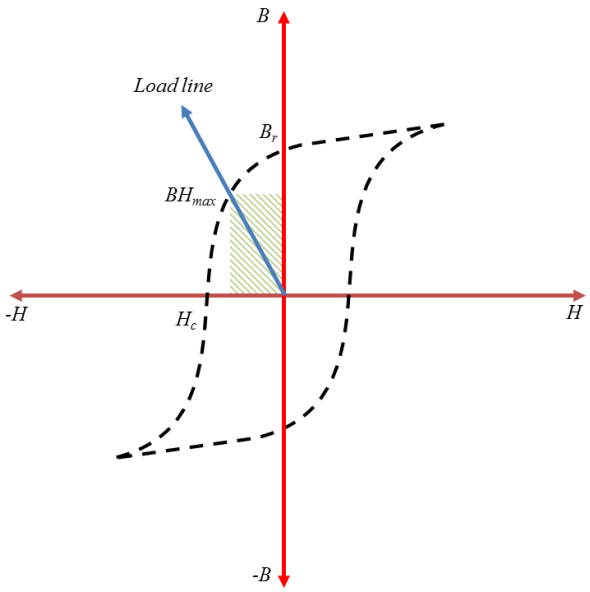


Figure 2-1: Hysteresis plot of a typical magnetic material

The operating point of the magnet is determined by the intersection of the load line with the demagnetization curve whose slope is given by $-\left(\frac{1-N_d}{N_d}\right)$, where $N_d$ is the demagnetizing factor of the magnet and depends on the geometry of the magnet which is altered by the design of the magnet. For the most efficient use of a material the geometry of the magnet should be shaped such that the load line passes through the point at which the *BH* product has its maximum value ($BH_{max}$). The performance of magnetic materials is largely dependent on temperature, with the magnetization curves degrading with increase in temperature.

## 2.2 Evolution of Permanent Magnetic Materials

Magnetic steels were the earliest (1885) commercially manufactured permanent magnets. They were typically alloys of carbon, iron and manganese with coercivities of 100 Oersted. Magnetic steels were

manufactured by conventional metal melting, casting and annealing methods. Their coercivities were improved by the addition of cobalt and chromium, resulting in a maximum coercivity of 230 Oersted. They were associated with temperature and metallurgical instability at normal temperatures. The use of these magnetic steels have become scarce since the emergence of better magnetic materials having lesser cost and better magnetic properties [29].

Commercial magnets that followed magnetic steels *viz.* transition metal alloy magnets, hard ferrite or ceramic magnets and rare earth transition metal alloy magnets were based on fine particles and have been categorized as modern magnetic materials. The manufacturing techniques changed from inclusion hardened techniques to fine particle manufacturing techniques such as sintering and casting. Sintering is the compaction of fine alloy powder in a die and then fusing the powder into a solid material with heat and high pressures in an aligning magnetic field [30]. The high temperatures and pressures during the sintering process results in uniform fine grains which greatly improves physical and magnetic properties. These techniques allowed the manufacturing of isotropic and anisotropic grade magnets. In depth treatment of the manufacturing processes can be found in the detailed texts [29, 30].

Alnico magnets were one of the first modern magnetic materials and were developed in 1930s. Having their permanent magnetism based on shape anisotropy, alnico magnets were manufactured by casting or sintering of metal powders. They were composed primarily of iron, nickel and cobalt and smaller quantities of aluminum and copper. Having coercivities almost double compared to magnetic steels (400 Oersted), alnico magnets have good corrosion resistance, good temperature stability, high mechanical strength and higher remanence. Since they are prone to demagnetization due to vibration and shock and have low coercive force and low energy product, alnicos have been replaced by permanent magnetic ferrites and rare earth transition metal alloys.

Magnetic ferrites developed in the 1950s were the first magnetic materials with the permanent magnetism based on crystalline anisotropy. Hard ferrite magnets are typically composites of iron oxide and either barium carbonate ($BaCO_3$) or strontium carbonate ($SrCO_3$). The manufacture process involves the ball milling of the alloy to reduce the particle size followed by pressing dry and sintering to obtain the final magnet. They are also known as ceramic magnets since they are made by powder metallurgical methods and their material properties are similar to ceramic materials. Commercial ferrite magnets have a maximum value of $BH_{max}$ of 3.5 MGOe or 28 kJ/m$^3$. Ceramic magnets have a high coercive force, good corrosion resistance and high temperature tolerance. They have a low energy product and low mechanical strength in bulk. An interesting phenomenon is that the ferrites shown an increase in coercivity with increase in temperature.

Rare earth (RE) magnets are typically alloys of lanthanide elements with transition metals and/or boron. The two most commercially popular rare earth magnets are samarium cobalt and neodymium iron boron. Samarium cobalt magnets were developed in the late 1960s and their permanent magnetism is based on the crystalline anisotropy of the material. Manufacture of SmCo magnets involves the melting and casting of the alloy followed by crushing and grinding to produce powders of small particle sizes (~ 10 μm). This powder is aligned in a magnetic field and compressed in a die and finally sintered. Samarium cobalt rare earth magnets are oxidation resistant, have higher energy products compared to ceramic and alnico magnets and have the best temperature resistance compared to all hard magnets but are characterized with a very low mechanical strength. $SmCo_5$ have energy products of 20MGOe or 160kJ/m$^3$. Among transition metal alloys Co-Pt is another modern magnetic material with energy products of up to 10MGOe but they are the most expensive commercially available permanent magnet. The concern over the cost and availability of samarium and cobalt led to the use of iron instead of cobalt with various RE elements. But the manufacture of RE-Fe compounds

was challenging due to their reactivity and their low operating temperatures. The two challenges were overcome by the addition of boron to increase the Curie temperature by 200$^{o}$C to 300$^{o}$C. NdFeB magnets based on crystalline anisotropy were developed in the early 1980s. NdFeB magnets have adopted the same manufacturing technique as for SmCo magnets. Neodymium iron boron rare earth magnets have the highest energy product compared to all the hard magnets. They have a very high coercive force and a moderate temperature resistance. They are easily oxidized, have low mechanical strength and low corrosion resistance. Cost-wise Fe is cheaper than Co and Nd is cheaper than Sm. They have energy products from 20 to 50 MGOe that is 160kJ/m$^3$ to about 400kJ/m$^3$. Nowadays the process of rapidly quenched NdFeB is being used to manufacture NdFeB bonded magnets compared to the conventionally sintered NdFeB process since the rapidly quenched NdFeB is not affected by oxidation. The table 2-1 compares the figures of merit of the major magnetic materials.

**Table 2-1: Comparison of the magnetic properties in magnetic materials**

| | Magnetic Steels | AlNiCo | Ceramics or Ferrites | Rare earth transition metal alloys | |
|---|---|---|---|---|---|
| | | | | Samarium Cobalt | Neodymium-Iron-Boron |
| Coercive force $H_c$ [kA/m] | **Poor** | **Low** | **Moderate** | **High** | **High** |
| Remanence $B_r$ [T] | **High** | **High** | **Low** | **High** | **High** |
| Maximum Energy Product $BH_{max}$ [kJ/m$^3$] | **Poor** | **Moderate** | **Low** | **High** | **High** |
| Temperature Stability $T_c$ [$^0$C] | **High** | **High** | **Moderate** | **High** | **Poor** |

## 2.3 Magnetic Physical Force Principles

Employing permanent magnets to design devices and machines with magnetic sensors and work driven actuators are typically based on the following physical force principles [31].

*a. Coulomb force principles*

Actuators based on Coulomb force convert magnetostatic energy to mechanical work. The devices typically work in the attraction mode defined by a constant force or in the repulsion mode defined by a force across a distance. The forces and torques are proportional to the intrinsic magnetization of the permanent magnet $Bi^2$. Actuators typically working on the Coulomb force principles are reed switches, micromanipulators, micromagnetic couplers, micromagnetic bearings and micromagnetic separators. As sensors they can be used as on-chip magnetometers. They possess the advantage of stable position in case of power disruption compared to electromagnets.

*b. Faraday principles*

These devices work on the principle of conversion of mechanical energy to electrical energy. The change in magnetic flux within a conductor turn is linked to the induced or generated voltage which is proportional to the flux density *B*. Typical examples of actuators following the Faraday principle are micromotors, microgenerators, microphone and most moving coil type actuators. The use of permanent magnets compared to conventional windings are beneficial since permanent magnets take lesser space and have higher precision to result in rapid acceleration of the motors or generators. Application of this principle is associated with the need for some sort of wound conductor.

*c. Lorentz force principles*

Based on the conversion of electrical energy to mechanical energy, this principle is best suited for micro actuators. As the principle is based on the interaction between current and magnetic flux to

produce a linear force or torque, planar coils interacting with permanent magnets provide the simplest configuration to develop microactuators. Here the force is proportional to the air gap flux density *($B_g$)*, the coil conductor length *(l)* and the current *(i)* flowing through the conductor. A permanent magnet with higher flux density improves the force and actuation times. Typical examples of actuators using the Lorentz force principle are micropositioners, especially in hard disk memory access and the print hammer actuation in line printers, fluid control valves and pumps in microfluidics, micro steppers and servomotors, micromirrors, optical switches and micro scanners.

## 2.4 Prior art in Magnetic Scanners

MEMS Micromirror scanners have been developed based on electrostatic [32], electromagnetic [33], electrothermal [34], magnetostrictive [35], piezoelectric [36, 37], shape memory alloys [38], pneumatic and hydraulic [39] actuation mechanisms. In the following section the focus is on MEMS electromagnetic scanners that have been previously published. The magnetic mechanism of actuation, the mirror dimensions, the mirror performance and the intended application are briefly compared.

One of the earliest (1994) works on magnetically actuated scanners was a 2-D electromagnetic scanner demostrated by Asada et al [40]. The mirror was bulk fabricated from a 200 µm thick substrate and was actuated electromagnetically using 16 µm thick electroplated copper coils. The inner plate which resulted in y-axis motion was 4 x 4 mm2 and the outer frame causing the x-axis motion was 7 x 7 mm2. This scanner had a scanning angle less than 3 degrees in x-axis and less than 1 degree for y-axis at 35mA coil current. Another early scanner fabricated through bulk-silicon micromachining was demonstrated by Miller and Tai [41]. The design combined a $4 \times 4$ $mm^2$ bulk micromachined single layer crystal silicon plate and a $3 \times 3$ $mm^2$ magnetic thin film of Permalloy for the electromagnetic actuation. The scanning angle was about 60 degrees and was achieved using a 30 turn planar copper coil with a current of 30mA. Judy and Muller [42] presented their work on

magnetically actutated addressable microstructures. Their design consisted of a (430 × 130 × 15) $\mu m^3$ NiFe plate attached to (400 × 2.2 × 2.2) $\mu m^3$ polysilicon torsional beams. The integrated coil was 10 turns and with a current of 500mA and the actuator was propped 45 degrees out of plane.

Miyajima et al. at Olympus [43] have developed MEMS 1-D scanners with mirror size (4.2 × 3.0) $mm^2$ for insertion into commercial laser scanning confocal microscope. Ahn and Kim [44] demonstrated a mirror working with mirror dimensions of (3.5 × 3.5) $mm^2$ and an outer frame of (5.7 × 5.7) $mm^2$ with two rotational axes. Using Lorentz forces as the actuation mechanism measured resonant frequencies of 380 Hz and 150 Hz reported maximum scan angles (total optical scan range) was 5.44 degrees at 30mA in resonance for inner axis and 51.34 degrees at 130 mA in resonance for the outer axis. A combined electrostatic/electromagnetic 2-D scanner was developed by Microvision Inc. for retinal scanning displays [45, 46]. The mirror of size 1.4 mm achieved a mechanical scan angle of 6.7 degrees horizontal and 4.8 degrees vertical. The mirror employed electromagnetic actuation for the outer frame to provide vertical or slow axis actuation and electrostatic actuation for the inner mirror axis to provide horizontal or fast axis actuation.

Bintoro [47] show an electromagnetic surface micromachined actuator on a single silicon wafer with CMOS compatibility. The design consisted of an gold microcoil, NiFe membrane with supported legs and a Co-Pt permanent magnet. The overall diameter of the membrane was 1600 μm with an overall height of 600 μm. The actuation current was in range of -0.25 to 0.3A for a displacement range of -71 μm to 28.3 μm. Bernstein et al [48] demonstrated a two axis low voltage (1-3V), magnetically actuated micromirror designed for an OCT endoscope actuation using small coils (#50 AWG wire. 390 turns – 35-40 ohms) in proximity of a moving mirror which contained a small permanent magnet (NdFeB magnet of size 0.6 mm × 0.8 mm × 0.18 mm glued on to mirror). The MEMS mirror was

fabricated using a SOI wafer and only 2 photo-steps. The scan angles achieved on both axes was +/- 20 degrees mechanical.

Cui et al [49] fabricated a micromirror based magnetic sensor for non-destructive experiments by using a SOI wafer process to electroplate a Permalloy layer on one side of micromirror. They achieved a magnetic field detection sensitivity of about 1 degree of mirror deflection per $10^{-4}$ tesla of field intensity. Chang-Hyeon Ji et al [50] demonstrated the use of radial magnetic field rather than the conventional lateral magnetic field to fabricate a gimbaled single crystal silicon micromirror with a single turn electroplated metal coil with a concentric permanent magnet assembly (NdFeB magnets: thickness 1 mm) composed of two concentric permanent magnets and an iron yoke. The magnetic field was oriented to produce 45 degrees to the horizontal and the vertical scan axis to achieve a biaxial magnetic actuation. With a mirror size of 1.5mm in diameter, a maximum optical scan angle of 8.8 degrees horizontal and 8.3 degrees vertical was achieved.

Urey et al [51] showed a very simple Lorentz force type actuator fabricated on FR 4 boards. The FR-4 mirrors have dimensions of 5 mm × 5 mm and achieve a scan angle of 17 degree at 1.8 kHz and 140 degrees at 417 Hz driven at 50mA with an effective magnetic field of 150 mT. Cho and Yoon [52] demonstrated a Lorentz force type micromirror without permanent magnets. The design consisted of a mirror plate and torsion bar made of bulk silicon using SOI, actuation coils made of electroplated gold. Performance showed maximum static deflection angles +/- 4.2 for x-axis actuation and +/-9.2 for y-axis actuation. Actuation voltages were below 3V. Lai and Tsou [53] reported an assembled tiny permanent magnet on a supporting beam to couple with a fixed solenoid coil for driving a micromirror plate in vibration for a Laser scanning micromirror device. With a 5V peak to peak alternating voltage, the scanning micromirror was able to achieve 11.2 degrees at a resonant frequency of 4434 Hz.

## 2.5 Summary

In most of the aforementioned works the use of bulk or surface micromachining requires the use of exotic magnetic materials and complicated deposition techniques of the magnetic materials in a cleanroom environment. Some of the designs use the integration of commercial monolithic magnets to provide the necessary actuation. These works require specific deposition techniques and several photolithography steps and release steps. Realization of electromagnetic actuators for MEMS applications demands high magnetic performance, minimal temperature effects, chemical stability and ease of fabrication. The use of soft magnetic materials has been undertaken with conventional microfabrication techniques such as sputtering, evaporation and electroplating of soft Ni, Fe, and Co alloys to enable sensors, actuators and micromachines. However the magnetic properties, particularly the permeability, coercivity and energy density are far lower than bulk hard magnet properties.

# Chapter 3: Polymer Permanent Magnets and Actuators

## 3.1 Bonded Permanent Magnets

*Bonded magnets*

Fully dense permanent magnetic materials particularly the sintered ones are very hard and brittle which pose a problem of not being able to easily machine the magnets. To overcome this limitation bonded magnets were developed. Bonded magnets are hard magnetic particles (ferrites, transition metal alloys and rare earth transition metal alloys) which are bonded with resins to result in powders or bonded powders. The advantage of manufacturing bonded magnets was to gain mechanical flexibility to allow shape complexity in addition to their magnetic properties, to help in corrosion resistance and to have a control over the magnetic geometries and direction of magnetic fields of the final manufactured magnet. This gives rise to magnetic actuator designs previously not possible. While the magnetization of these bonded magnets are reduced compared to the magnetic alloy, the coercive field is not affected. This is mainly due to the addition of the resin which reduces the packing density of the magnets.

Typical binders used are thermosetting binders such as epoxy resin, thermoplastic binders such as polyamides (nylon) and elastomers such as nitrile rubbers [54]. While the magnet manufacturing process largely remains the same, compression molded magnets use thermosetting binders, injection molded magnets use thermoplastic binders and extruded magnets use elastomer binders. These bonded powders are either anisotropic or isotropic. In anisotropic powders which have better magnetic properties in a given direction, an alignment field is necessary during the manufacturing process. Isotropic bonded powders have equal magnetic properties in all directions and require no alignment field during the manufacturing process.

Bonded ferrites are typically manufactured using injection molding and rubber bonded magnets. While injection molding results in the best magnets with highest volume capability compression molding offers the highest energy product. $SmCo_5$ bonded powders are typically made from injection molding while the $Sm_2Co_{17}$ is made from both injection and compression molding.

NdFeB magnets are typically made by the rapidly quenching process which overcomes the oxidation problem resulting from conventional sintering of NdFeB magnets. These inherently isotropic powders are made by compression molding, injection molding or extrusion molding. The anisotropic grade powders are made by either compression molding or injection molding

The table below gives the different bonded powders, their magnetic nature and energy product.

**Table 3-1: Magnetic material properties of bonded magnetic powders [55]**

| Material | $H_c$ [kA/m] | $B_r$ [T] | $BH_{max}$ [kJ/m$^3$] | $T_c$ [$^0$C] |
|---|---|---|---|---|
| Ferrites bonded | 92-155 | 0.15-0.2 | 3-8 | 450 |
| SmCo bonded | 650-800 | 0.6-0.8 | 55 | 870 |
| NdFeB bonded | 550 | 0.7 | 85 | 310 |

## 3.2 Conventional and Hybrid Fabrication Techniques

*a. Conventional magnetic MEMS based fabrication techniques*

Conventional magnetic MEMS fabrication techniques employ planar deposition of magnetic materials onto substrates, predominantly silicon. The techniques include physical depositions such as sputtering [56], evaporation [57] and pulsed-laser deposition [58, 59] and electrochemical deposition such as electroplating [60-63]. Electroplating typically has the limitation of forming grain boundary defects. To achieve thick films is a challenge owing to the slow electroplating rates. Due to the high reactivity of rare-earth elements electroplating in an aqueous environment is not possible. SmCo

magnets have been sputtered [64, 65] but the deposition rates are slow and must have an annealing step which restricts the substrate to those which can take higher temperatures such as silicon, glass or alumina. Fabrication of NdFeB magnets or magnetic films with conventional MEMS techniques are always associated with the problem of oxidation and additional protective coatings such as tungsten, copper and niobium are mandatory, leading to the inclusion of an extra fabrication step [66]. While pulsed laser deposition results in thick NdFeB layers the deposition areas are small and the energy products are low. SmCo and NdFeB thick patterning and etching has been tried. Ion beam etching is slow and wet chemical etching is associated with poor etch control resulting in large over-etching. Another problem with sputtering or electroplating films is that there are large intrinsic stresses that develop due to the annealing step. Thicker the film fabricated by these techniques results in lower magnetic performance and this is due to the variations of grain size and shape.

*b. Hybrid fabrication techniques of magnetic materials*

To overcome the limitations of conventional magnetic MEMS fabrication techniques, several hybrid fabrication techniques have been suggested. These techniques involve starting with bonded magnetic powders as the filler materials into polymers resins, inks or photopatternable polymers. The composites can be spin coated, screen printed, squeegee coated, inkjet printed, drop-casted, replica molded or taped casted. These methods give rise to complex shapes and dimensional geometries to make interesting magnets with interesting end applications as microsensors and microactuators. Batch fabrication with rapidity and low cost can be achieved using the hybrid fabrication techniques. Following are the brief description of the hybrid procedures.

### 3.2.1 Replica Molding [67]

Replica molding involves the fabrication of a master which is typically fabricated by standard lithography or laser ablation followed by the casting of a liquid precursor against the mold. The

patterned structures are obtained by curing and demolding the structures from the mold material. The advantage of replica molding is that the substrate does not have to be rigid. Further replica molding against elastomeric masters largely increase the ease of separation, minimizes the damage to master while demolding, protects smaller features from tearing or breakage and promotes the reusability of the master. Both anisotropic and isotropic powders can be used with an appropriate magnetization step. Curing temperatures of the casted composite will determine the substrate that can be employed for fabrication.

### 3.2.2 Squeegee Coating [68]

Cavities of predetermined depths are etched into a rigid substrate and the uncured composite is poured into the cavities. By moving a piece of glass with a flat smooth edge across the substrate, the extra composite is taken away and finally cured. The cavities can be fabricated similar to replica molding by standard lithography or laser ablation or focused ion beam etching. The advantages are the production of uniform films with various thicknesses by varying the depth of the cavity in the substrate. Both anisotropic and isotropic powders can be used with an appropriate magnetization step.

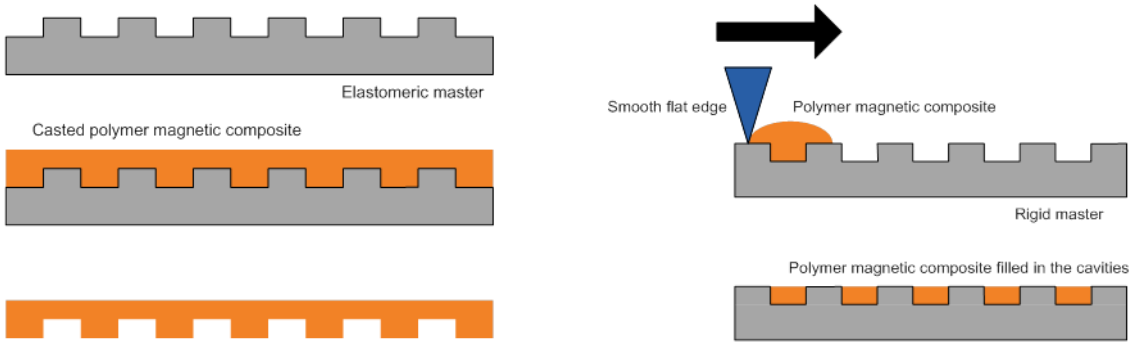


(a) (b)

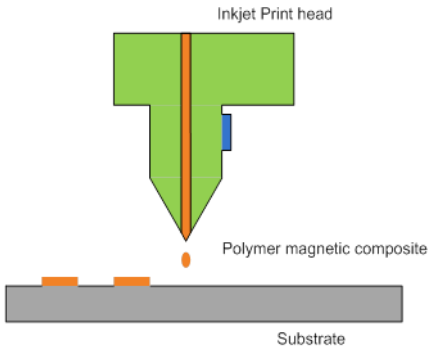


(c)

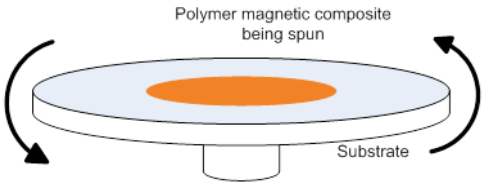


(d)

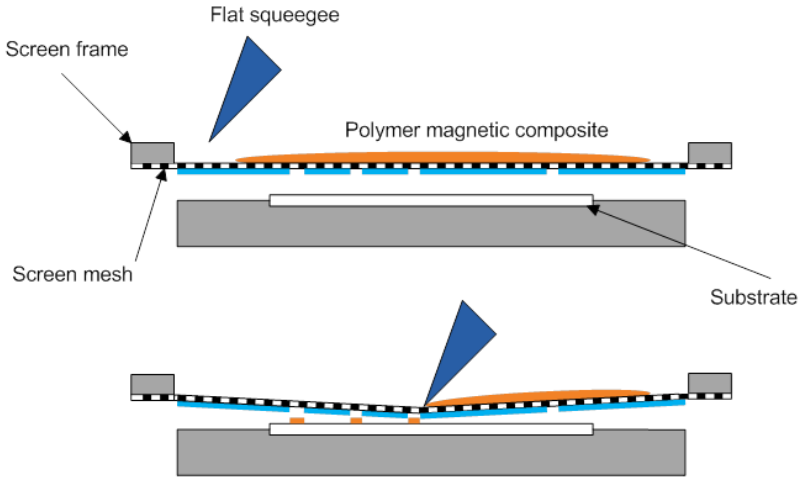


(e)

Figure 3-1: Viable hybrid polymer composite fabrication techniques (a) replica molding; (b) squeegee coating; (c) inkjet printing; (d) spin casting; (e) screen printing

### 3.2.3 Inkjet Printing [69]

With a low viscosity magnetic composite ink, inkjet printing offers good control over lateral geometries and the thickness of the exact geometry can also be controlled with the number of printing passes. The advantage of using inkjet printing is that there is no need for demolding or extra chemical

techniques such as etching. With the right technique, sandwich layers and devices can be fabricated. This method is characterized with serial manufacture of structures compared to parallel fabrication of replica or squeegee coating techniques.

### 3.2.4 Spin Casting [70]

This technique is ubiquitous to film deposition in the MEMS community. Preparation of thick films is possible via spin casting. Bonded powders can be sonicated into holding polymers and their viscosity is reduced by adding solvents and spinning. The added solvent can be removed by a baking step to result in either thin films or thick films depending on the parameters of spinning. The patterning of the films into the required geometry is performed by photolithography. Both anisotropic and isotropic powders can be used with an appropriate magnetization step.

### 3.2.5 Screen Printing [71, 72]

The technique of screen printing has been established and largely used by the printed circuit board industry. Screen printing uses a pattern designed on the mesh of a screen fabric. When a squeegee wipes across the surface of the screen fabric, the ink is forced through the open areas of the screen onto the substrate positioned under the screen. The image in the open areas is transferred onto the substrate. The substrate can be flexible like cloth or rigid like FR-4. The bonded powder must be prepared into an ink with low viscosity. Both anisotropic and isotropic powders can be used with an appropriate magnetization step.

## 3.3 Prior Art in Polymer Composite Magnets using hybrid fabrication techniques

### 3.3.1 Ferrite Polymer Magnets

Lagorce and Allen in their work [73] use Sr-ferrite powder mixed in Dupont PI-2555 polyimide. The particle size of the $SrFe_{12}O_{19}$ was between 1.15 and 1.5 µm. The particles were filled in the polyimide matrix in an 80 volume%. An external magnetic field is employed to compensate the reversible remanence loss due to exposure of the material to the polyimide cure temperature. The polymer magnets were manufactured by screen printing or spin casting followed by photolithography to make a structure with a disk polymer magnet over a flexural polyimide. The magnets were 250 µm in width and 100 µm in thickness. A maximum deflection of 25 µm in both directions was achieved by actuation via Lorentz force using planar coils. In their continued work [74] they fabricated screen printed ferrite discs on copper cantilevers actuated by planar coils. Epoxy resin was used as opposed to polyimide and in addition a ball mill rotating at 4-5 rpm for 72 hours was used to reduce the particle size for better fill ability. 80% volume loading of strontium ferrite powder was mixed with epoxy by ball milling. Following the addition of curing agent to make the liquid composite in to a solid composite, the composite was deposited and patterned the magnets using screen-printing into circular disks of 90 µm thickness and 2-4 mm in diameter onto the free end of a copper cantilever beam and actuated using a planar coil. The highest deflection of 25 µm was achieved for a beam of length 6mm width 1mm and thickness 19.5 µm upon which was a magnet of diameter 4mm. In comparison the larger actuator was able to achieve the deflection due to the reduced particle size resulting in better magnetic properties.

Cho and Ahn in their work [75] use Sr-ferrite powder and a room temperature curable epoxy resin called Devcon and filled 45% volume of the magnetic particles in a paste with the particle size about

1 μm. The paste was filled into cylindrical molds made from AZ PLP 100 photoresist by a rubber or metal squeezer. The final magnets were 65 μm thick with lateral dimensions from 50 to 200 μm. These magnets were mounted on a silicon substrate and actuated by Lorentz forces generated by an electromagnet resulting in a maximum deflection of 70 μm.

Feldmann et al in their works [76-78] presented the use of barium, strontium ferrite, samarium cobalt and NdFeB particles embedded in photopatternable resists (SU-8 and AZ9260). The SU-8 magnetic particle composites which were patterned by UV depth lithography could not hold high concentration of magnetic particles due to constraint of UV visibility necessary for crosslinking of the deposited film. In comparison they used a lift off technique to fabricate molds for screen printing. The composite to be screen printed was filled to 90% by weight resulting in much stronger magnetic structures. They design a monolithic Lorentz force actuator that was actuated by electroplated copper structure and achieved a maximum deflection of 300 μm.

Rozenberg et al. in their work [79] use magnetically anisotropic strontium ferrite particles in 25-30% volume loading into an epoxy resin Poxipol and 80% volume loading into an epoxy resin Structalit. The particles were in the form of flat plates with a diameter of 1 μm. They used screen printing to fabricate magnetic films of thickness from 10 μm to few 100 μm. The curing of the magnets was performed in the presence of a magnetic field of 2.4kOe to orient the individual magnetic particles in preassigned directions in order to obtain highest magnetization in the out-of-plane direction.

Remi et al. in their work [80] use strontium ferrite powder of particle size 1.8 -2.3 microns added to 3180 and mixed with a homogenizer (T18 Ultra Turrax) for uniform dispersion resulting in a greater particle uniformity than hand-mixing. They reported limitations in curing and etching and adhesion with volume percentages above 20%. They achieved a magnetic film by photocuring over a magnet. They present the best performance of a 10% strontium ferrite/3108 composite with sample magnetic

films of 2.25 $mm^2$ in area and 100 µm thick. The aligned composites had 74 $emu/cm^3$ remanence after saturation compared to 28 $emu/cm^3$ for the non-aligned films.

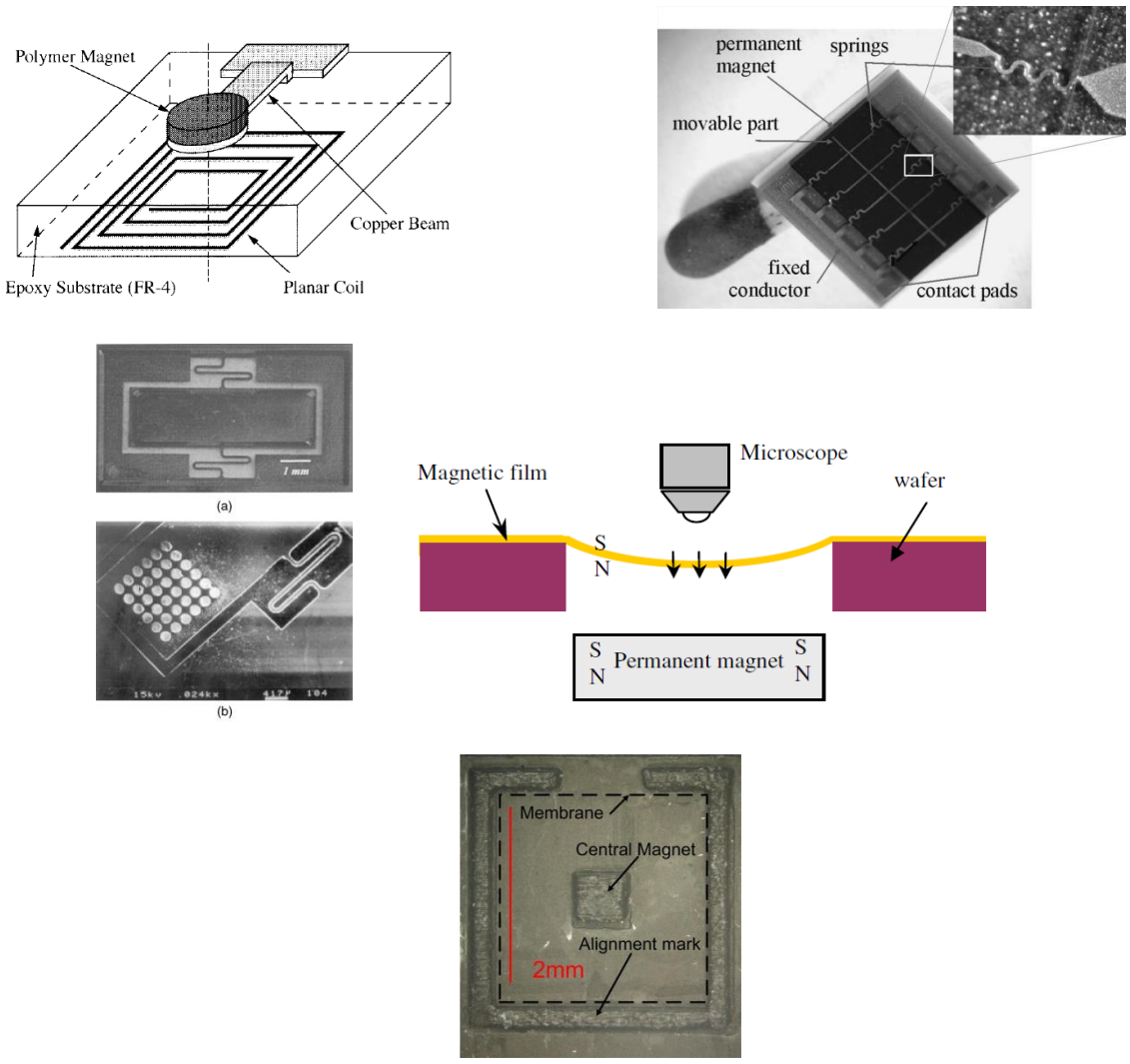


Figure 3-2: Microactuators in literature based on polymer composite hard magnets

### 3.3.2 Samarium Cobalt Polymer Magnets

Dutoit et al. in their work [81] use $Sm_2Co$ powder ball milled to reduce the particle diameters to 10 µm. The particle grains were treated with epoxysilane to avoid oxidation and also to improve mixing with polymers. The milled $Sm_2Co_{17}$ powder was embedded in a SU-8 photoepoxy in a 60% volume

loading and mixed at 15000 rpm for 10 minutes. An aligning 3000 G magnetic field was used to align the easy axis of the grains. The sensors, 35 µm thick were placed on a cylindrical hall sensor without magnetic flux concentrators and Au bonded on a PCB. The complete setup functioned as a gearwheel position sensor and mentioned that 1mVpp signal was obtained at 0.25 mm from the gearwheel.

### 3.3.3 Neodymium Iron Boron Polymer Magnets

Pawlowski and Topfer in their work [82] NdFeB bonded powders MQP-B and MQP-Q and wet milled for several hours in a porcelain mill with steel balls (7 mm diameter) in a mixture of organic solvents. The final medium particle size was about 10 µm. This powder was dispersed into a resin dissolved in a mixture of organic solvents. The loading of magnetic powder in the ink was varied from 70 to 91 wt%. The final inks were screen printed onto soft iron, alumina, glass and silicon. Dimensions varied from 50 by 50 $mm^2$ to 100 µm and thickness varied from 10 µm to 50 µm obtained by multiple screen printing. In their following work [83] used MQP-B and Q and S powders dispersed in a resin dissolved in a mixture of organic solvents. Using the doctor blade method they report a maximum concentration of 84-95 wt% magnetic powder to obtain a tape castable slip film.

Wang et al. in their work [84] fabricated elastic magnetic films by screen-coating or screen printing, moulding and squeegee coating. They used hard barium ferrite powder which is a ceramic and two types of NdFeB powders. The coercivity for hard barium ferrite powders was 4109 Oersted, for NdFeB I it was 1947 Oersted and for NdFeB II it was 3418 Oersted. They used a permanent magnet to produce a non-uniform external magnetic field. They mention that the best technique they found was squeegee coating. The permanent magnet had a field of 0.21 Tesla and it resulted in a deflection of 125 µm only for the NdFeB films and nothing for the hard barium ferrite films.

Romero et al. in their work [85] disperse NdFeB anisotropic microparticles on a PMMA solution at room temperature at low magnetizing fields. They use an alternative process called flash annealing

[86, 87] to overcome the limitation of high temperature processing. A mixture of the polymer and magnetic particles in a 70 % volume density was deposited using an ink-jet printer with high gas pressure at the nozzle and cured at temperature 150$^{o}$C and/or UV light. They report a single film thickness of 0.1 mm per pass of the ink-jet printer. They use a rain dropping technique with a mechanical shaker over a solution of PMMA and solvent (chloroform, ethyl acetate or tetrahydrofurane). They applied a magnetic field during the drying up process to make anisotropic magnetic thick films oriented to the long direction of the applied magnetic field of 500 Oersted. Their A films had a maximum Hc of 1.36 T and a Mr of 0.47 T with a BHmax of 5.2MGOe for the out of plane magnetization. B films had Hc 1.24 T and Mr of 0.67 T and BHmax of 8.7 MGOe. The C films had Hc of 1.33 T and Mr of 0.65 T and a BHmax of 8.8 MGOe all for the out of plane magnetization of the samples.

Wang et al. in their work [88] used wax powder particles introduced as a binder agent for dry packing NdFeB powder in pre-etched trenches in a silicon wafer to manufacture magnets in the 100 μm to 1mm range. They also report that only a small amount of wax powder (2 to 6.5%) can effectively lock the magnetic powder to form micromagnets with improved coercivities. The fabricated magnets were 500 x 500 x 320 μm$^3$ with Coercivity of 737 kA/m and a maximum energy product of 16.6kJ/m$^3$. The use of dry pressing magnetic particles to produce micro-magnetic structures with superior magnetic properties has also been shown by Bowers [89], Tzu-Shun Yang [90] and Oniku [91].

Khosla et al. in their work [92] use MQFP-15 ultrasonically dispersed in SU8-3010 polymer to fabricate magnets of length 5mm width 200 μm and height 30 μm by UV lithography. The remanent magnetization (Mr) of 62.80 and coercivity $H_x$ of 5290 G at 72 weight percent of the MQFP-15 isotropic powder was reported. They report that the MQFP-12-5 offers up to 4 times the magnetic remanence of isotropic ferrite powders and 2 times the remanence of anisotropic ferrite powders. In

an extension of the work Hilbich et al. [93] use PMMA Plexiglas as a mold to deposit a composite polymer of PDMS and MQP-12-5 (75% by weight). This composite was magnetized in a magnetic field of 2.5T to produce permanent bidirectional magnetization. The actuator was a 3 to 8 mm square membrane and was actuated using hard disk microcoils. The intended application was into microfluidic lab-on-a-chip devices. A final deflection of 100 μm was achieved with the 3 to 8 square membranes for magnetic fields ranging from 52 to 62 mT.

Weber et al in their work [94] use two techniques to make polymer magnets for integration into a silicon micromirror. The first technique involves spin-coating of the polymer magnets made by hard magnetic neodymium powder (MQP-S-11-9) mixed with an epoxy resin with low viscosity (Araldit 2020). The hard magnetic powder is isotropic with a particle size ranging from 35-50 μm. They claim that the maximum fill ratio of magnetic particles in the polymer to lead to homogeneous substrates is about 80% by weight. The final film was about 70-80 μm thickness. They cut out 600 by 600 μm pads of mass 180 micrograms and the pads were magnetized in a magnetic field of 1000 kA/m (that is 1000G or 0.1 T). The second technique involved pressing of polymer magnets. The pressing was performed to increase the fill ratio of the isotropic powder into the epoxy resin. They claim that the fill ratio achieved was 87.5% by weight and this increases the magnetic force by 15%. They magnetized this fill with a field of 2500 kA/m (that is 2500G or 0.25 T). They achieved a deflection angle of 9 degrees for a static field of 8mT for the first technique fabricated magnets and 2mT for the second fabricated magnets. They mention that for resonance performance the 9 degrees is achieved at 6 μT.

## 3.4 Summary

In order to fabricate and develop high performance polymer magnetic microactuators, several critical parameters must be considered. These parameters include the selection of the magnetic filler material

with fine particle size, high starting magnetic properties and chemical compatibility with the matrix material. The matrix material must have a high volume loading ability with appropriate viscosity and inertness. In regards to the mold substrate care must be taken in selecting an appropriate substrate that is chemically inert to the polymer hard magnetic composite and must be thermally and magnetically compatible with the processing technique. In addition both the filler and matrix materials must have chemical process compatibility, temperature compatibility and magnetic compatibility. The next section details the critical factors affecting the preparation of high performance polymer hard magnetic composites.

# Chapter 4: Design and Fabrication of Polymer Composite Hard Magnetic Micromirrors

Typical requirements to develop a bidirectional magnetic actuator are a moving beam or membrane actuated via an external magnetic field. Four possible configurations based on the physical principle of Lorentz force actuation employing permanent magnets, microcoils and soft-magnetic membranes are discussed in [47]. The first configuration consists of a soft magnetic membrane actuated by a top and bottom microcoil. The second configuration consists of a soft magnetic membrane between a permanent magnet and a top microcoil. The third configuration consists of an integrated permanent magnet on a beam actuated by a top and bottom microcoil. Finally, the fourth configuration consists of a microcoil embedded into a cantilever beam with a permanent magnet below the beam.

While these configurations presented are intended for standard MEMS fabrication, our work presents the modification of the soft magnetic beam or membrane structure into a polymer hard magnet fabricated via squeegee coating and actuated using microcoils. The design configuration of the magnetic circuit with magnetic micropowder embedded in a PDMS matrix and actuated by microcoils results in achieving an actuator with simpler fabrication technique and larger actuation compared to soft magnetic actuators or conventionally fabricated hard magnetic actuators.

## 4.1 Critical Factors Affecting Good Polymer Composite Preparation

In order to achieve good magnetic films and structures via hybrid bonded powder fabrication consideration must be made of the filler bonded magnetic powders used, the polymer matrix used, the volume percentage of the filler loaded into the polymer matrix and the effect of magnetic field during fabrication.

### 4.1.1 Composite Filler Material

It has been illustrated that among the available bonded powders, NdFeB powders possess the highest energy product. Although this is a strong argument for their use to fabricate better performance actuators, NdFeB powders suffer from low temperature processing and operation. Bonded samarium cobalt powders offer high energy products and a higher resistance to high temperature processing but they are associated with higher costs. Bonded ferrite powders offer moderate energy products and temperature stability with a lower cost but require higher saturation magnetization to make useful magnetic actuators. While anisotropic bonded powders typically possess higher magnetic performance properties, employing such powders as opposed to isotropic powders involves the requirement of a particle aligning magnetic field during the curing step to maximize the magnetic strength of the final magnet. Material selection depends on the strength of the required magnet, the required processing conditions and the cost.

### 4.1.2 Polymer Matrix Material and Loading Density

The binders typically used in the manufacture of bonded powders can be used as the polymer matrix to make homogenous magnetic composites. The choice of the polymer matrix determines the processing and temperature of the final cured composite, the structural rigidity or elasticity. A critical factor to be considered for the choice of the polymer matrix is based on its ability to accept large volume loading of filler material. Typically there are additions to improve dispersion via dispersion allowing agents. Although the intrinsic coercivity $(H_{ci})$ of the magnetic powder loaded into a polymer matrix is unaffected, the magnetization magnetic moment per unit volume decreases [95]. Polyimide matrices offer a high temperature processing ability due to the superior thermal stability of polyimide. Any reversible remanence losses occurring due to high temperature (below the Curie temperature) curing of polyimide are mitigated by the exposure to an external magnetic field. Epoxy resins and

silicones offer low temperature processing to manufacture hard magnetic actuators but have the advantage of fabricating elastic and flexible magnets. Wax powder particles have also been used as a binder agent for dry packing NdFeB powder. The volume percentage can be drastically increased by using the dry packing method.

### 4.1.3 Volume Loading

The amount of filler material being loaded or doped into the polymer matrix determines the strength of the resulting magnet. While loading the filler materials to high volume or weight percentage results in better magnetic properties, the usability of the composite in spin casting, inkjet printing or screen printing is seriously limited due to high viscosities. Employing low viscosity epoxy resins are preferred in hybrid techniques such as screen printing and inkjet printing that require the composite ink to have low viscosity. Magnetic remanence of polymer magnets is proportional to the fill factor and anisotropy of the filler powder [96]. Parallels can be drawn from the macro-manufacture of magnets wherein stronger fully dense magnets are manufactured from pressing or compacting the powder to increase the fill density into the polymer matrix. In addition, the particle size of the bonded powders has an effect on the final magnetic composite. The maximum powder content into a polymer matrix can be obtained if the tap density (bulk density after compaction) is comparable to the fine-milled powder is compared to the materials density. It has also been shown that by using a combination of larger and smaller particles, the tap density is increased since the smaller particles are loaded into larger particles. The optimum powder particle packing formulated by Andreasen and Anderson [97] is expressed by the equation

### 4.1.4 Effect of Magnetic Field during Composite Cure

The biggest problem of obtaining high magnetic properties from bulk magnetic material to thin films is the directional non-equivalence of the film's magnetic characteristics wherein the out-of-plane film

magnetic characteristics is worse than the in-plane film magnetic characteristics [29]. The lateral film dimensions are way bigger than its thickness and it is difficult to magnetize a film on its edge. Fabrication with the starting material as an anisotropic hard magnetic powder results in a magnet with better magnetic properties. While using isotropic hard magnetic powder the direction in ease of magnetization must be determined and the appropriate perpendicular biasing field or longitudinal biasing field must be applied. In the case of anisotropic hard magnetic powders dispersed in a polymer matrix it is beneficial to apply a magnetic field during the curing process wherein the uncured composite crosslinks into a rigid structure. The application of a magnetic field during curing eventually results in the particles aligning in the direction of ease of magnetization. Once the curing process is complete the composite structure is magnetized to its saturation magnetization to have a final product with better magnetic performances.

## 4.2 First Generation Micromirror Design and Fabrication

The design of the first generation micromirror consisted of a two torsion bar polymer magnetic structure with a square reflective aperture of gold. The mirror was suspended above rectangular planar coils that provide actuation by Lorentz forces.

### 4.2.1 Single axis straight torsion bar micromirror

The micromirror aperture was designed with a square dimension of 4mm × 4mm and the torsion bars were 4mm in length and 400 μm in width. The entire polymer composite structure had a thickness of 250 μm which was defined by the spin step of the mold fabrication. The polymer composite structure was suspended by two cylindrical Plexiglas anchors of 1mm diameter and 1mm and 2mm in height. The design schematic of the single axis straight torsion bar micromirror with the dimensions is shown in the Figure 4-1.

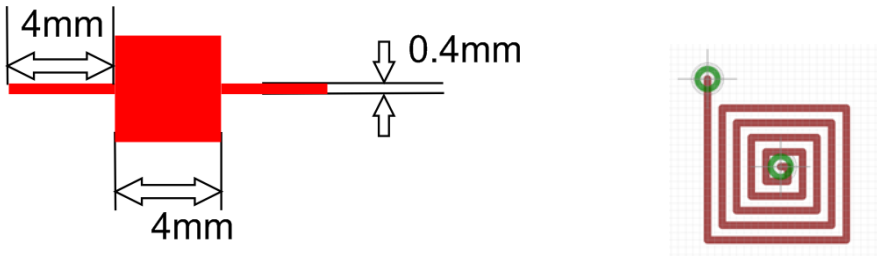


Figure 4-1: Design schematic of the first generation single axis micromirror and microcoil

### 4.2.2 First generation micromirror fabrication

The polymer magnetic structure size is defined by the dimensions of the master mold onto which the polymer magnetic composite is micromolded. Factors affecting the size include the optical lithography resolution, the incident laser beam spot on the mirror aperture, the planar coil configuration and the manual demolding viability. As the demolding of the cured polymer composite is performed manually, smaller sizes risk damage to the structure of the mirror. The fabrication schematic is shown in the Figure 4-2.

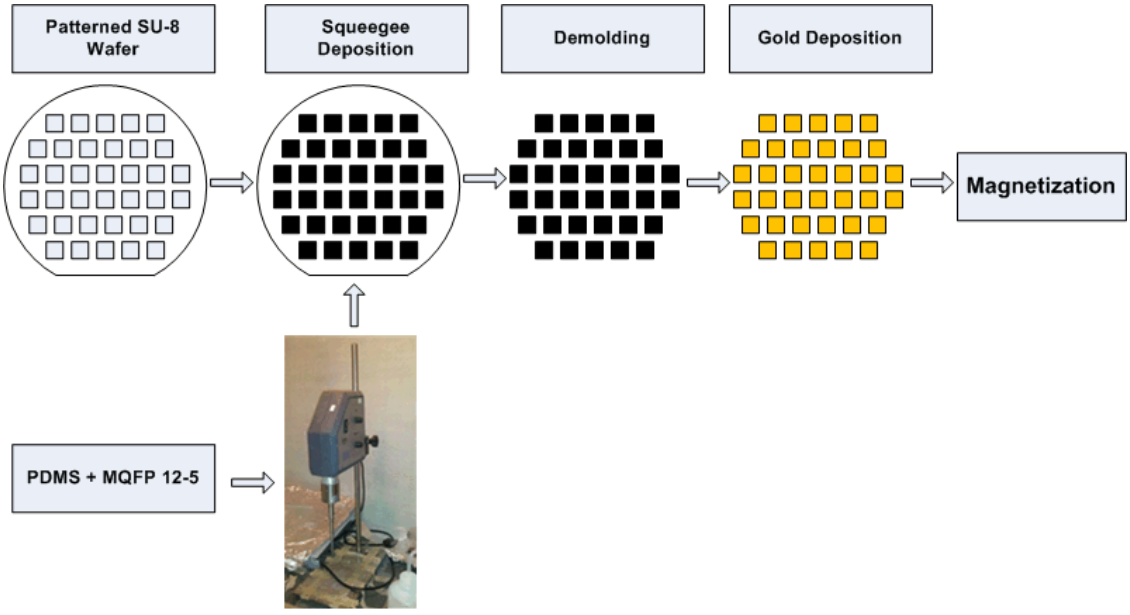


Figure 4-2: Schematic of the first generation micromirror fabrication

The first generation fabrication consisted of a combination of standard photolithography and soft lithography. This consisted of three steps *viz.* mirror mold fabrication, polymer magnetic composite preparation and planar coil integration. The process flow of the fabrication is shown in the Figure 4-3.

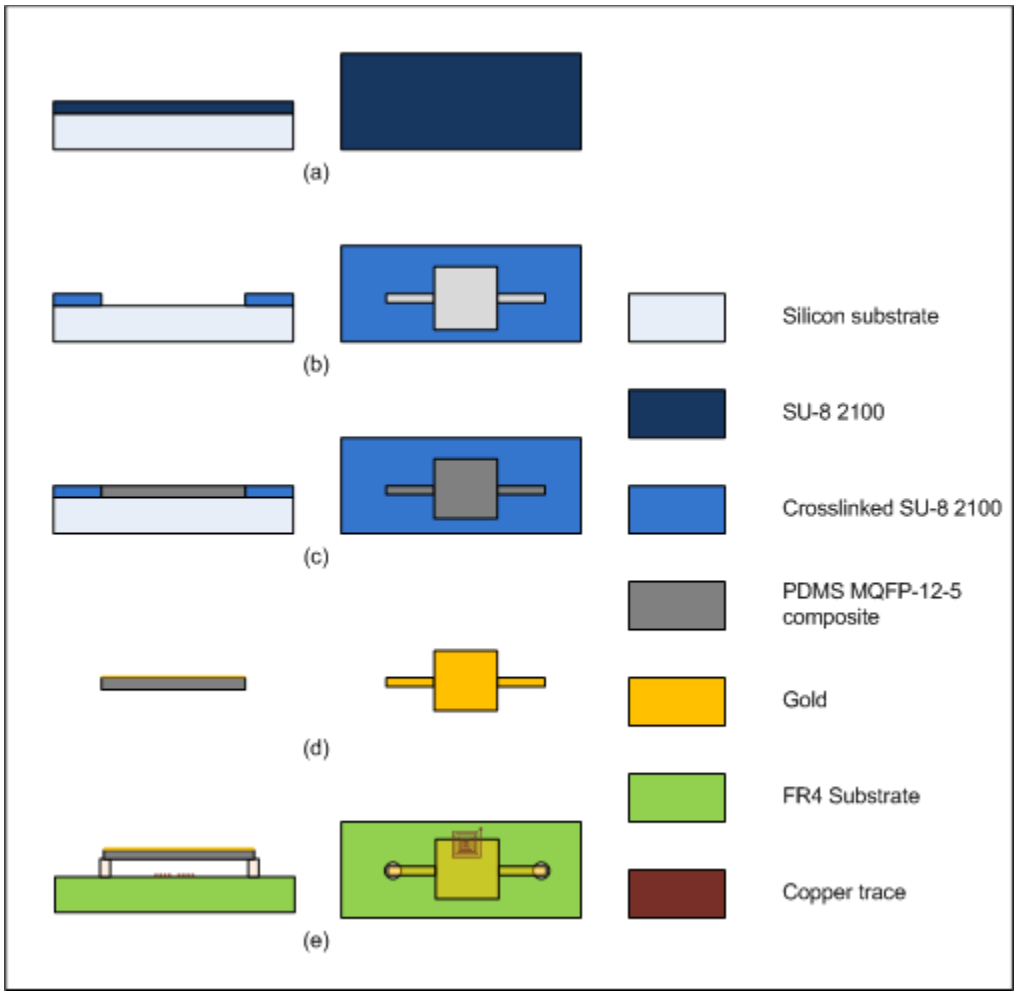


Figure 4-3: Fabrication process flow for the first generation micromirror

The mirror mold fabrication was performed by standard photolithography of SU-8 2100 [98] (a negative tone photoresist) on a 4 inch, <100> silicon wafer. The wafers were procured from University Wafer USA. SU-8 has been used extensively as a mold material in microfluidics and prototyping of MEMS structures due to its inertness and biocompatibility.

SU-8 2100 was procured from MicroChem Inc and the processing spin speed, pre-exposure bake, exposure energy, post-exposure bake and developing times were followed as recommended by the supplier to achieve a layer thickness of 250 µm. Polydimethylsiloxane (PDMS) was used as the polymer matrix due to its Young's modulus, binding compatibility and convenience of preparation of composite polymer materials compared to similar polymer matrices such as SU-8, PMMA or polyimide. The PDMS (Sylgard 184 Elastomer kit) [99] was procured from Dow Corning USA and used as per the suppliers recommendations without any modification. The magnetic filler material was chosen to be MQFP-12-5 [100]. MQFP-12-5 is a low cost bonded neodymium isotropic magnetic micropowder with a particle size D50 of 5 µm. The MQFP-12-5 magnetic powder was donated by Magnequench International Inc.

A cleaned <100> n-type 4 inch silicon wafer is used as the mold substrate. A 250 µm layer of SU-8 2100 is spin coated using a desktop spin coater (Laurell technology WS-400 lite series spin coater). To achieve a layer of 250 µm the spin parameters selected were Speed: 1250 rpm; time: 90seconds: ramp: 176 rpm. This is followed by a three step pre-exposure baking on a hot plate (Fisher Scientific Isotemp Hot Plate) to reduce the stress in the thick SU-8 layer. The first pre-bake was at 60 $^0$C for a duration of 30 minutes followed by the second pre-bake at 75 $^0$C for a duration of 30 minutes and finally the third pre-bake at 90 $^0$C for a duration of 60 minutes. After the pre-bake, the SU-8 film is flood exposed over a mylar mask for 50 seconds using a SUSS MA6 mask aligner. To ensure complete crosslinking of the thick SU-8 layer a two-step post-exposure bake was performed. The first bake was at 65 $^0$C for a duration of 30 minutes and the second bake was at 90 $^0$C for a duration of 60 minutes. The exposed and fully crosslinked SU-8 is developed to the end-point using SU-8 developer (MicroChem Inc.) for 20 minutes under manual agitation. The end-point of development is confirmed

by spraying isopropyl alcohol. If there is a white residue observed while spraying isopropyl alcohol the wafer is further developed. The Figure 4-4 shows the complete mold required to fill in the polymer composite.

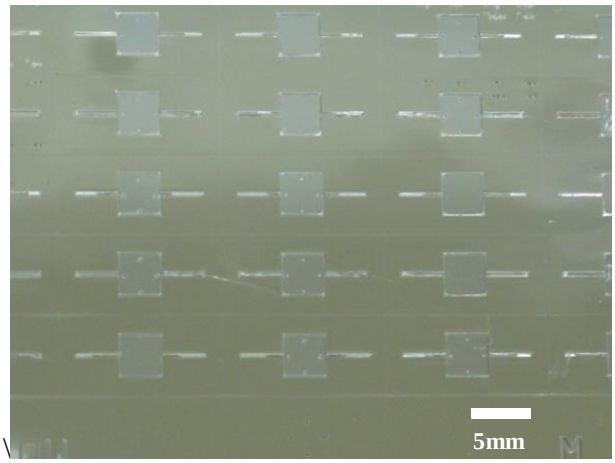


Figure 4-4: Patterned SU-8 2100 mold

The preparation of the polymer hard magnetic composite is initiated by the preparation of PDMS. The base elastomer and curing agent (Dow Corning USA) were mixed in a ratio of 10:1 by weight using a glass rod. The mixed base elastomer and curing agent is placed in a vacuum chamber for 30 minutes to remove any air bubbles resulting from manual mixing. The isotropic magnetic powder MQFP-12-5 ($(Nd_{0.7}Ce_{0.3})_{10.5}Fe_{83.9}B_{5.6}$) donated by Magnequench International Inc. (now Molycorp, Magnequench Inc), is doped in the degassed PDMS matrix at a weight percent of 80% and manually mixed with a glass rod. To ensure uniform dispersion an ultrasound horn tip probe is immersed into the composite at an operating frequency of 40 kHz for ten minutes. The resulting composite is filled into the previously fabricated mold by squeegee coating. The excess composite is removed using a rubber scrapper. The mold filled with polymer composite is placed in a vacuum chamber for degassing and is further cured at 80 $^0$C for 120 minutes. The cured polymer magnetic structures are carefully demolded by manually peeling them off the wafer using precision tweezers. A 100nm reflective gold layer is

deposited by e-beam evaporation (BOC Edward's A306). The uniform dispersion of the magnetic micropowder into the PDMS matrix is illustrated in the Figure 4-5.

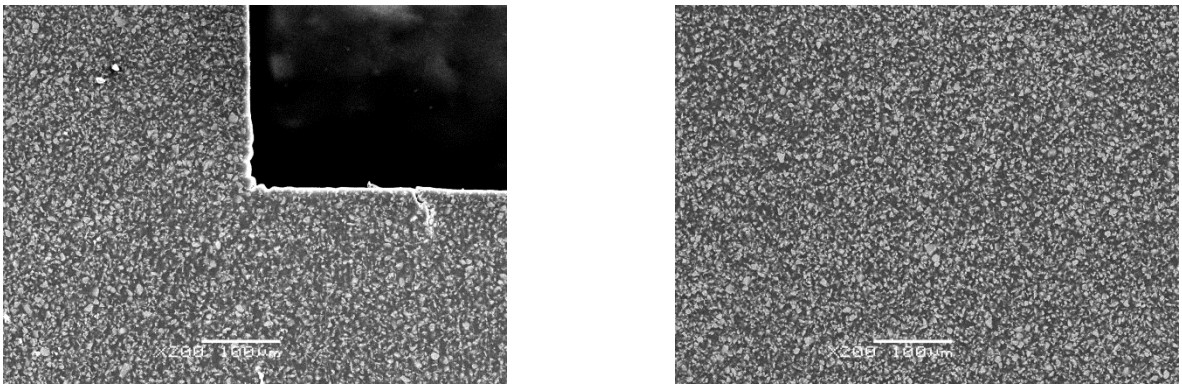

Figure 4-5: SEM images showing the uniform dispersion of magnetic microparticles

### 4.2.3 First generation microcoil design

The optimum gap spacing between the mirror and the planar coils was determined by finite element modeling of the magnetic field generated for varying values of current. The distance at which the maximum magnetic flux density was generated at a current of 0.95A was chosen for the design of the gap spacing Plexiglas anchors. The planar coils made of copper were designed with a trace width and spacing of 254 μm (10 mils). The copper traces had a trace thickness of 35.56 μm (1.4 mils at 1Oz copper). This thickness of copper has a limitation of ampacity or the maximum current that the trace can carry. The maximum current ampacity for the external copper traces of the planar coil according to the ANSI/IPC-2221/IPC-2221A design standards [101] is determined by the equation, $I = 0.048 \times dT^{0.44} \times A^{0.725}$, where $I$ is the current passing through the segments in Amps, $dT$ is the rise in temperature above the ambient in $^0$C and $A$ is the cross-sectional area in mils$^2$. Considering a temperature rise of 25 $^0$C and a cross-sectional area of 14 mils$^2$, the maximum current or ampacity through the copper traces is calculated to be 1.34 A. For the safety of the planar coil a maximum

current of 0.95A was used in the actuation experiments. The peak magnetic flux density generated at the center of the planar coil at 0.95A current is 1.6mT.

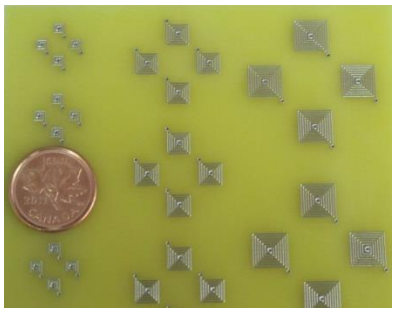

Figure 4-6: Rectangular planar coils on FR-4 substrate

### 4.2.4 Magnetization of the Polymer Composite Structures

Magnetization is performed using a dipole electromagnet (GMW Associates, Dipole Electromagnet, 3470) [102]. Demolded samples are magnetized under a field of 1.8 Tesla. Magnetization prior to e-beam evaporation is detrimental to the magnets due to high temperature inside the chamber. High temperatures above or close to the maximum operating temperatures (80 – $100^0$C) of the magnetic powder demagnetize the magnets.

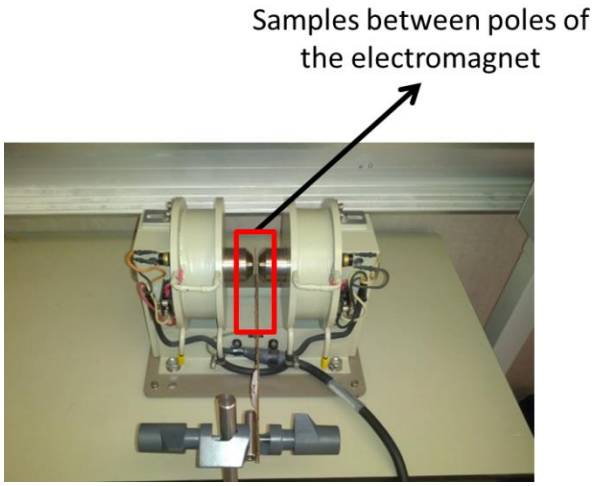


Figure 4-7: GMW 3470 electromagnet employed to magnetize the polymer magnetic composite

The magnetized micromirrors are integrated on the FR-4 substrate by using a two-part epoxy onto the Plexiglas cylinders. The mirrors are suspended such that the maximum magnetic field generated at the center of the microcoil is aligned to the edge of the square aperture with an inside offset. The integrated micromirror on top of the FR-4 substrate is shown in the Figure 4-8.

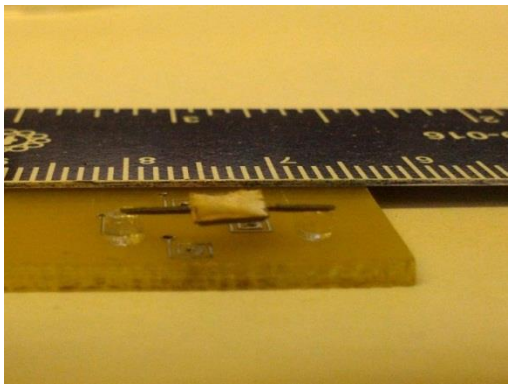

Figure 4-8: Integrated first generation micromirror

## 4.3 Second Generation Micromirror Design and Fabrication

The first generation design was associated with challenges in integration of the micromirror and the coil substrate. Gluing of the tip of the torsion bars to the cylindrical Plexiglas anchors required extreme patience and often resulted in the reflective surface to roll and not be parallel to the planar coils. To solve this instability and integration challenge the second generation design of the polymer composite mirror includes an outer frame around the straight torsion bar and mirror aperture. The outer frame provides stability to the mirror and also promotes ease of integration of the mirror structure above the planar coils that provide actuation by Lorentz forces. The design of the planar microcoils is modified to spiral coils to increase the magnetic flux density to result in larger actuation.

### 4.3.1 Single axis outer frame straight torsion bar micromirror

The schematic of the single mirror is illustrated in the figure below. The torsion bar and mirror aperture dimensions are same as the first generation design (square aperture of 4mm × 4mm; torsion

bars of 4mm length and 400 µm width). The frame has a longer side of 14mm and a shorter side of 12mm. The lateral thickness around the frame is 1mm and the height of the frame is defined by the depth of laser ablation for the entire structure which is 250 µm. The design schematic is illustrated in the Figure 4-9.

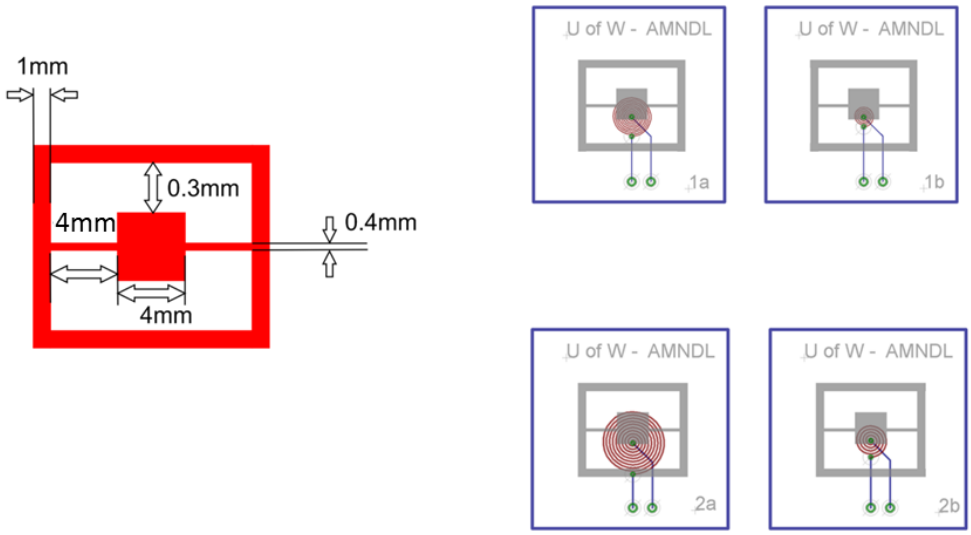


Figure 4-9: Design schematic of the second generation single axis micromirror and microcoils

### 4.3.2 Dual axis design with inner and outer gimbal frames straight torsion bar micromirror

Similar to the single axis mirror, the dual axis mirror has the same dimensions of torsion bar and mirror aperture as the first generation design. This design has one gimbal frame and an outer frame. The inner torsion bars attached to the mirror aperture define the deflection in the alpha axis while the gimbal frame and outer torsion bars define the deflection in the beta axis. The entire structures are mounted on a Plexiglas frame as aforementioned. The gimbal frame is designed with different opposite thicknesses. The frame sides attached to the outer torsion bars have a thickness of 400 microns and a length of 11.16 mm. The other two sides of the frame have a thickness of 1mm. The

design is done such to increase the area influenced by the Lorentz forces generated by the planar coil to aid larger deflection in the beta axis. The schematic of the dual axis mirror is illustrated in the Figure 4-10.

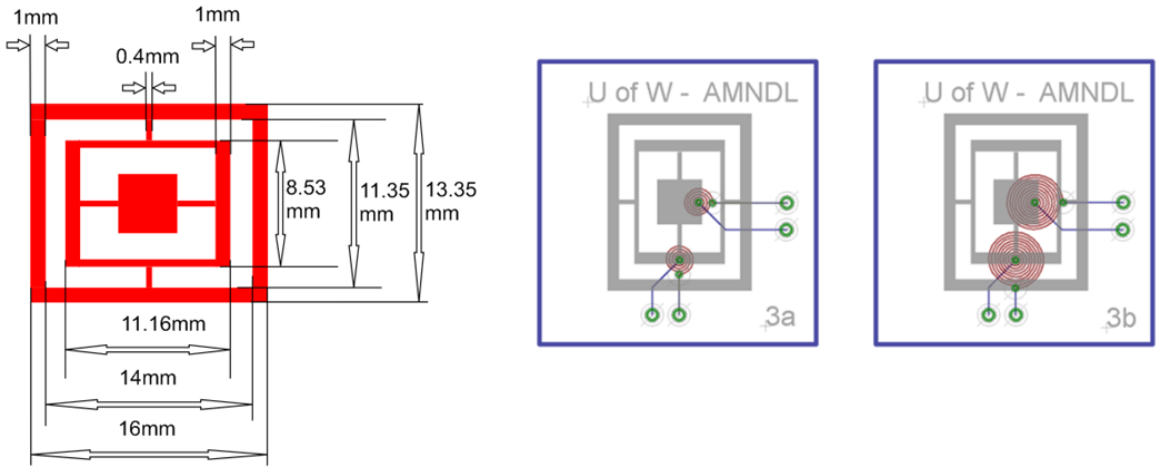


Figure 4-10: Design schematic of the second generation dual axis micromirror and microcoils

### 4.3.3 Second generation micromirror fabrication

The second generation of the polymer hard magnetic composite mirror was fabricated by retaining the composite preparation method and squeegee coating method while changing the method of mold fabrication. This results in a low-cost fabrication process without the need for any photolithography steps. The entire structure including the frame, torsion bars and mirror aperture are magnetic and made from the same polymer composite hard magnetic material.

The mold against which the mirror is casted was fabricated by laser ablation of Plexiglas using a $CO_2$ laser. A universal laser system VERSALASER 2.4 [103] was used to ablate Plexiglas. The patterns were designed in COREL draw (version 10). The laser ablation is defined by two parameters namely power and speed. These parameters allow for different thickness ablation of any material. To achieve a 250 µm thick structure, a power of 25% with a speed of 25% was used. These parameters were

determined by experimentation since commercial Plexiglas has different densities depending on the thickness of the material and type of Plexiglas. The laser ablated molds with the polymer composite filled in through squeegee coating is shown in the figure below along with the schematic of fabrication.

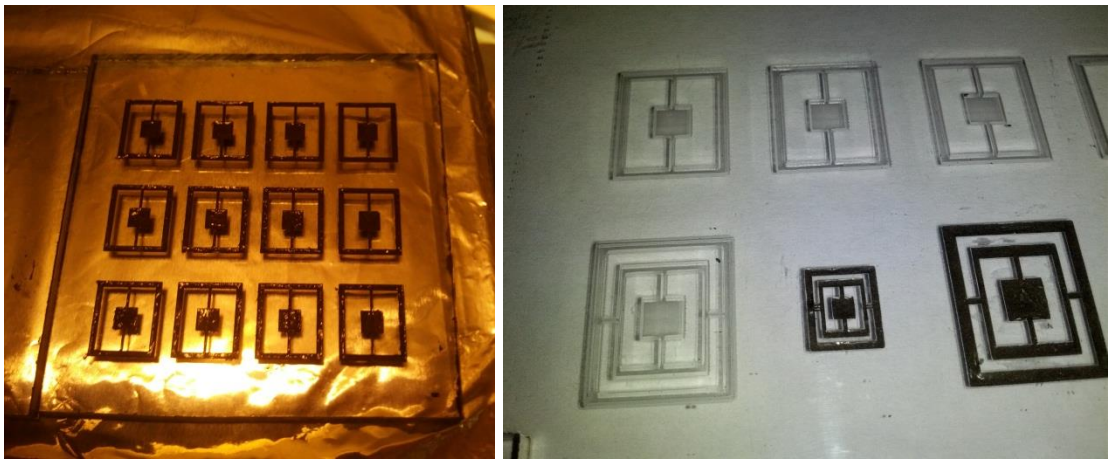

Figure 4-11: Micrograph showing the Plexiglas molds for single and dual axis micromirrors

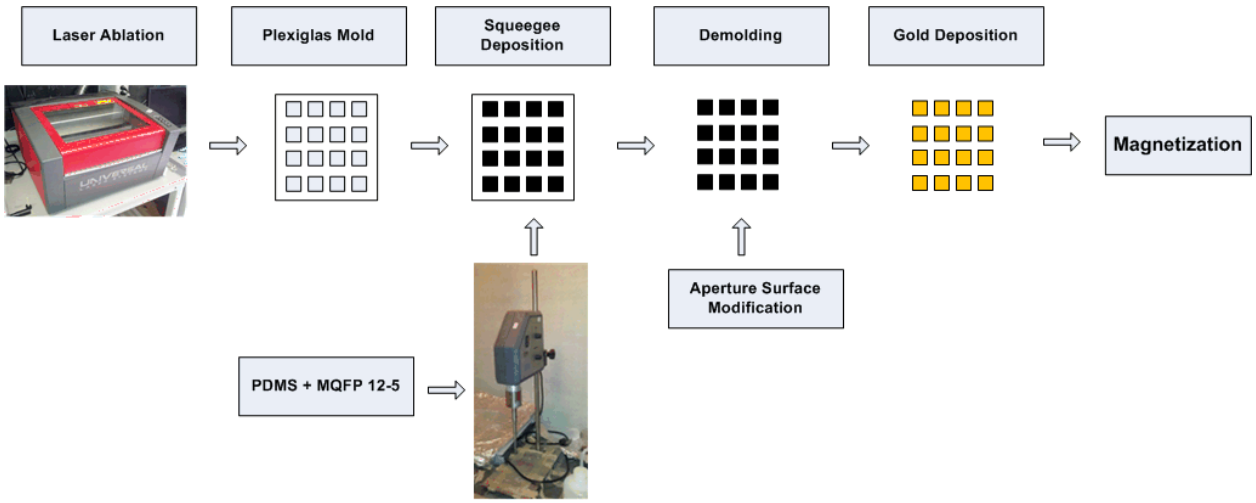


Figure 4-12: Schematic of the second generation micromirror fabrication

Following the curing of the polymer magnetic composite, the structures are demolded using precision tweezers and a gold reflective layer of 100 nm is deposited by e-beam evaporation. Further the samples are magnetized using the GMW 3470 electromagnet under a field of 1.8 Tesla. The anchor frame upon which the gimbal frame and mirror structure sits on was also fabricated out of Plexiglas using the laser ablation machine. Using the laser ablation machine gives a huge advantage of fabricating many molds with various design parameters such as torsion bar width, mirror width, frame width. While the same may be possible by photolithography, the cost is higher and a cleanroom is mandatory. With the laser machine, in lab fabrication can be done which improves the turn-around time for device fabrication. The integration of the anchor frame and the mirror structure is performed same as the first generation. Two part epoxy glue was used to fix the mirror structure on the Plexiglas anchor frame. The micrographs of the single axis and dual axis micromirrors are illustrated in the Figures 4-13 and 4-14.

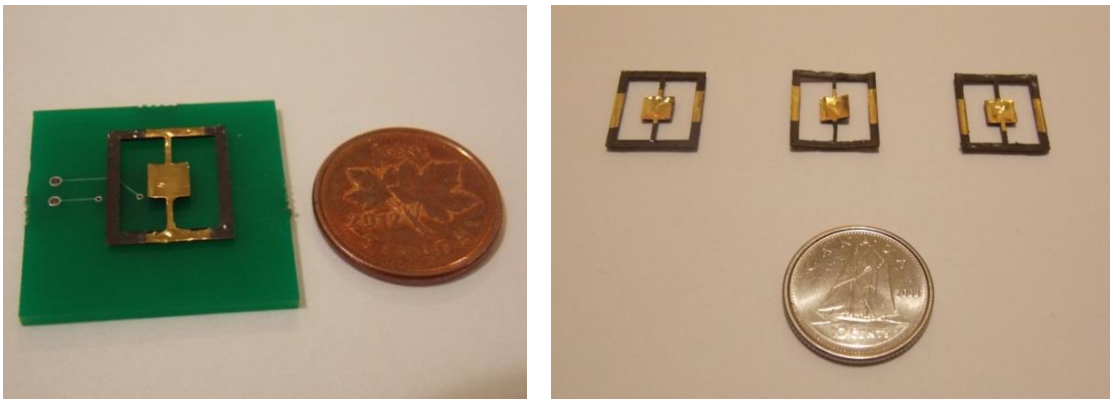

Figure 4-13: Micrograph of the fabricated second generation single axis micromirror

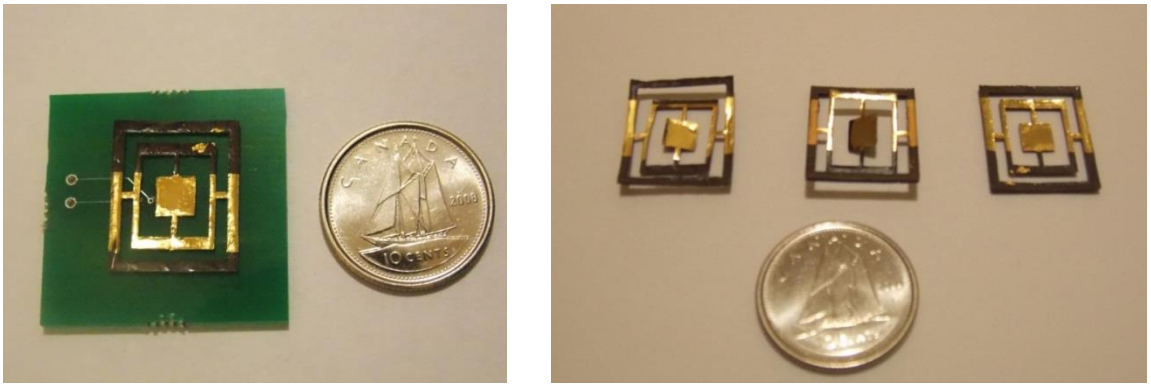

Figure 4-14: Micrograph of the fabricated second generation dual axis micromirror

### 4.3.4 Second generation microcoil design

To increase the magnetic flux density generated by the planar coils a circular spiral design was employed. The new designs of the planar coils had a trace width and spacing of 127 µm and 200 µm with the same copper thickness of 35.56 µm (35.56 µm at 1Oz copper). The coils were designed in the PCB design software, EAGLE and manufactured by myroPCB Inc. [104]. The dual axis mirror with the gimbal frame needed two planar coils to actuate the mirror in both alpha and beta axes. While the first planar coil is located below the mirror aperture, the second planar coil is located below the center of the thicker edge of the gimbal frame. The Figure 4-15 shows the fabricated PCB spiral microcoils. The white silk screen was designed in the layout to assist in the precise integration of the micromirror over the microcoils. The table 4-1 details the axis of actuation, trace width, pitch, number of turns and resistance of each of the seven designs of the spiral microcoils.

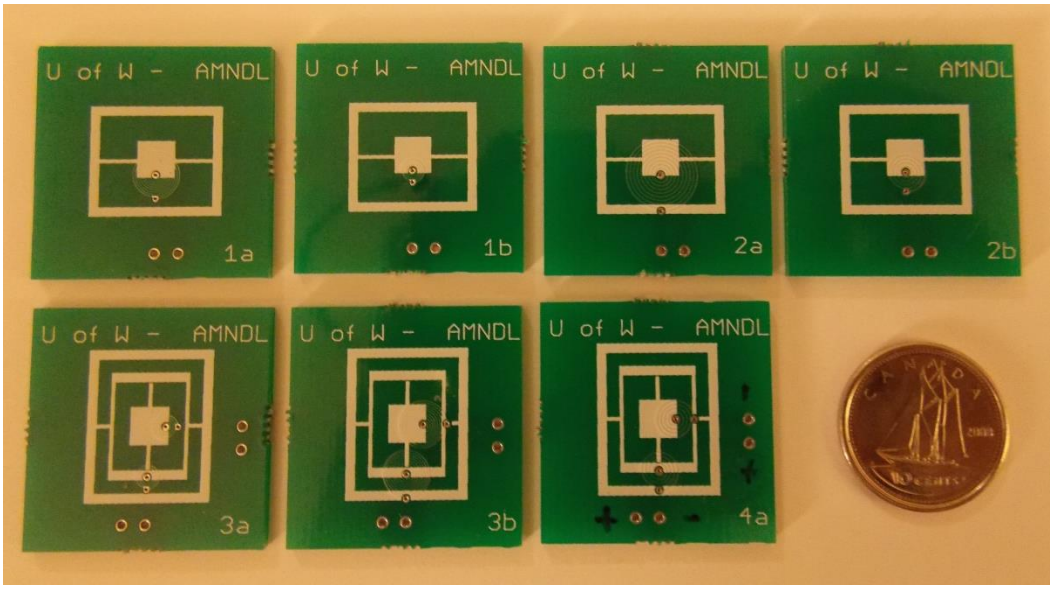


Figure 4-15: Planar microcoils for the second and third generation micromirrors

Table 4-1: Second generation planar microcoil parameters

| Design | Actuation | Trace width | Pitch | Turns | Resistance |
|---|---|---|---|---|---|
| 1a | Single axis | 127µm | 127µm | 10 | 0.6Ω |
| 1b | Single axis | 127µm | 127µm | 5 | 0.4Ω |
| 2a | Single axis | 200µm | 200µm | 10 | 0.6Ω |
| 2b | Single axis | 200µm | 200µm | 5 | 0.5Ω |
| 3a | Dual axis | 127µm | 127µm | 5 | 0.5Ω |
| 3b | Dual axis | 127µm | 127µm | 10 | 0.6Ω |
| 4a | Dual axis | 200µm | 200µm | 5 | 0.4Ω |

## 4.4 Third Generation Micromirror Design and Fabrication

Magnetization of the second generation micromirror revealed that at equilibrium condition, the intermagnetic forces between the inner gimbal and outer frame influence the angular deflection of the moving parts due to their inherent magnetic flux density. The third generation design is characterized by a non-magnetic frame. While the dimensions of the torsion bars, mirror apertures, inner frames and outer frames have the same dimensions, the outer frames in both the designs are non-magnetic. Since the outer frames are magnetic as in the previous designs, the outer frames influence the angular deflection of the moving parts due to their inherent magnetic flux density. The planar coils are located in the same positional locations as the previous design. As previous the entire structures are mounted on a Plexiglas frame.

### 4.4.1 Single axis outer frame, straight torsion bar micromirror and dual axis with inner gimbal and outer frame straight torsion bar micromirror

The design schematics of the third generation single axis and dual axis micromirror are illustrated in the figure below. The transparent frame consists of undoped PDMS and the design in red is represented by the polymer magnetic composite. The inner torsion bars attached to the mirror aperture define the deflection in the alpha axis while the gimbal frame and outer torsion bars define the deflection in the beta axis. The entire structures are mounted on a Plexiglas frame as aforementioned. The gimbal frame is designed with different opposite thicknesses.

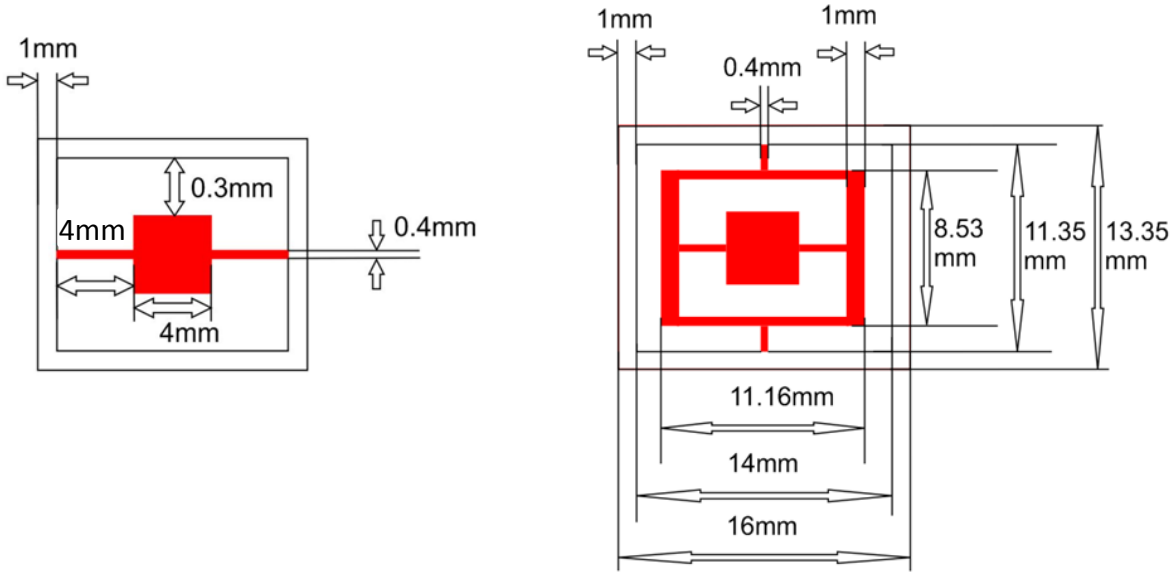


Figure 4-16: Design schematic of the third generation single and dual axis micromirror

### 4.4.2 Third generation micromirror fabrication

Previous figures show the deformation of the mirrors at equilibrium condition after magnetization. Undoped PDMS is used to fabricate the non-magnetic outer frames. The laser ablated molds used in the second generation fabrication are used for the third generation fabrication. In order to fabricate non-magnetic frames the inner torsion bars and mirror aperture for the single axis mirror and the inner torsion bars, mirror apertures, gimbal frame and outer torsion bars for the dual axis mirror are prepared first. The prepared polymer composite is filled into the mold by squeegee coating only in the required areas. Following this the polymer composite is completely cured under room temperature for a period of 48 hours. Undoped PDMS is prepared by mixing the base elastomer and the curing agent in the ratio of 10:1 by weight. Following manual mixing the resulting micro bubbles are removed by degassing the PDMS in vacuum. The PDMS is carefully filled into the remaining areas again via squeegee coating and cured at room temperature for a duration of 48 hours. Once the curing is

completed the structures are demolded from the Plexiglas mold carefully using tweezers. The fabrication schematic and the completely fabricated single axis and dual axis micromirrors are illustrated in the figures below.

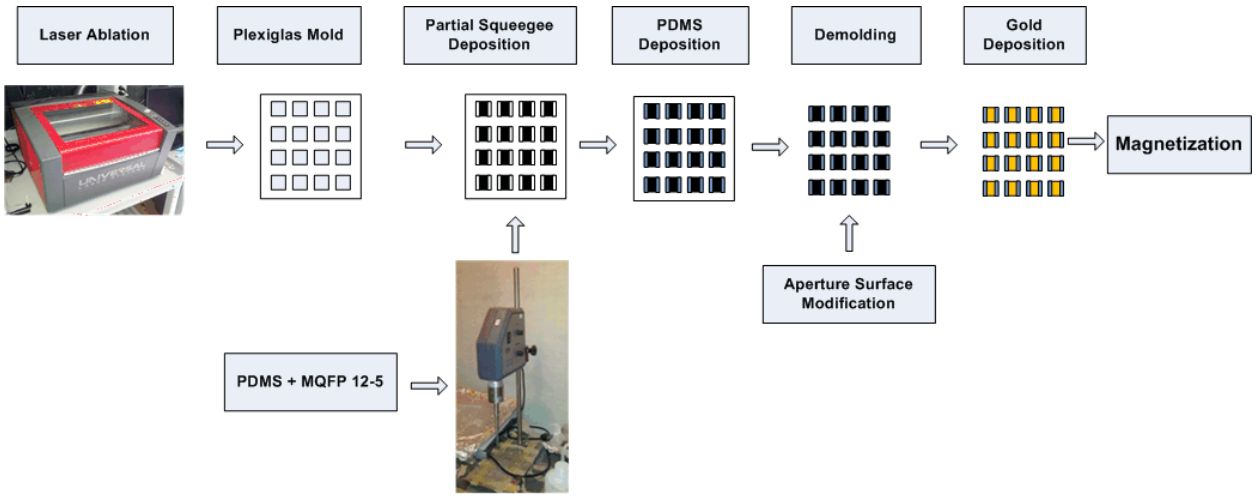


Figure 4-17: Schematic of the third generation micromirror fabrication

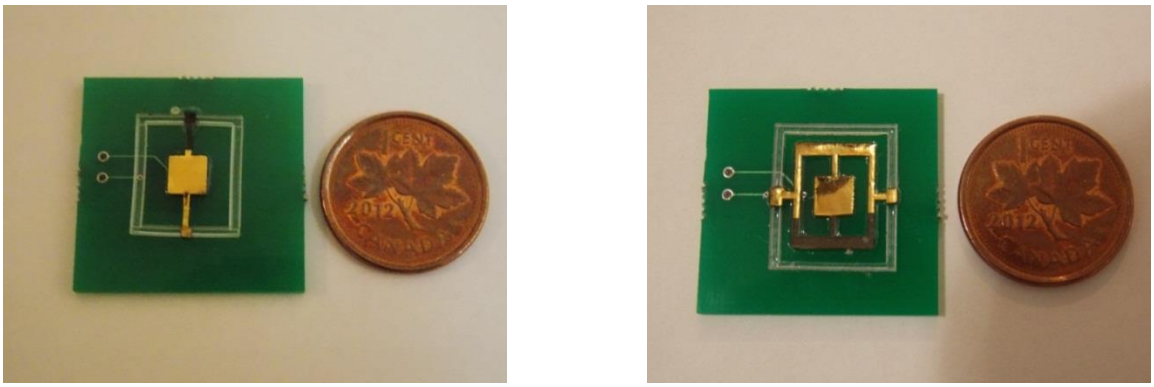

Figure 4-18: Micrograph of the fabricated third generation single axis and dual axis micromirror

## 4.5 Summary

Three generations of micromirror scanners have been designed and fabricated using the hybrid fabrication technique of squeegee coating against a master mold. The first generation micromirror

was fabricated against a photolithographically patterned SU-8 2100 master mold and was actuated using 254 μm rectangular planar microcoils. This design showed limitations in the stability after integration of the mirror structure on the microcoil. The second generation was designed with an outer frame which provides the necessary stability for the micromirror. The second generation micromirror was fabricated against a laser ablated Plexiglas master mold and was actuated using 200 μm spiral planar microcoils for the single axis micromirror and using 100 μm spiral planar microcoils for the dual axis micromirror. Although the stability issue was solved, the influence of the magnetic flux density of the outer frame and mirror aperture for the single axis micromirror and the influence of the magnetic flux density of the outer frame, gimbal and mirror aperture for the dual axis micromirror resulted in the deformation of the mirror at equilibrium condition. To overcome this limitation the third generation micromirrors were fabricated with non-magnetic undoped PDMS outer frames and actuated by the Lorentz forces generated by the spiral planar microcoils.

# Chapter 5: Simulation and Experimentation

In order to determine the operating parameters of the micromirror scanner and the magnetic field intensities of the planar microcoils finite element modeling of the mirror and the planar coils were performed using the multi-physics simulation software COMSOL 3.5a. Resonant frequency analysis, planar coil magnetic flux density analysis and angular deflection analysis were performed. The modeling process in COMSOL involves the predefinition of the physics application modes, the definition of the multiphysics problem, the usage of the physical properties of the model and the extraction of design parameters using postprocessing tools. The typical modeling steps involved in creating a model in COMSOL are the creation of the model geometry, the defining of physics on the domain and at the boundaries, the meshing of the created geometric model, the solving of the physical model and the postprocessing of the solution.

## 5.1 Microcoil magnetic flux density simulations

The magnetic flux density generated by the microcoil actuates the micromirror scanner through Lorentz forces. Since the magnetic flux density generated by any magnetic material or device is inversely proportional to the cube of the distance, it is important to determine the maximum magnetic flux density at a given coil current. This distance of maximum magnetic flux density for a given coil current is the gap spacing between the magnetic micromirror and the planar coils.

The modeling steps followed in the simulation of both the rectangular planar coils and the spiral planar coils are similar for the exception of the starting model geometries. The *Magnetostatics* application mode under the *AC/DC* module was selected for the analysis. This application mode provides the analysis of electric and magnetic potentials. The weak constraints were turned off while the constraint type was set to be ideal. The geometries of the model were designed according to the

dimensions illustrated in the design section of both the rectangular and spiral microcoils. The Figure 5-1 shows the created geometries for both the microcoils with five turns.

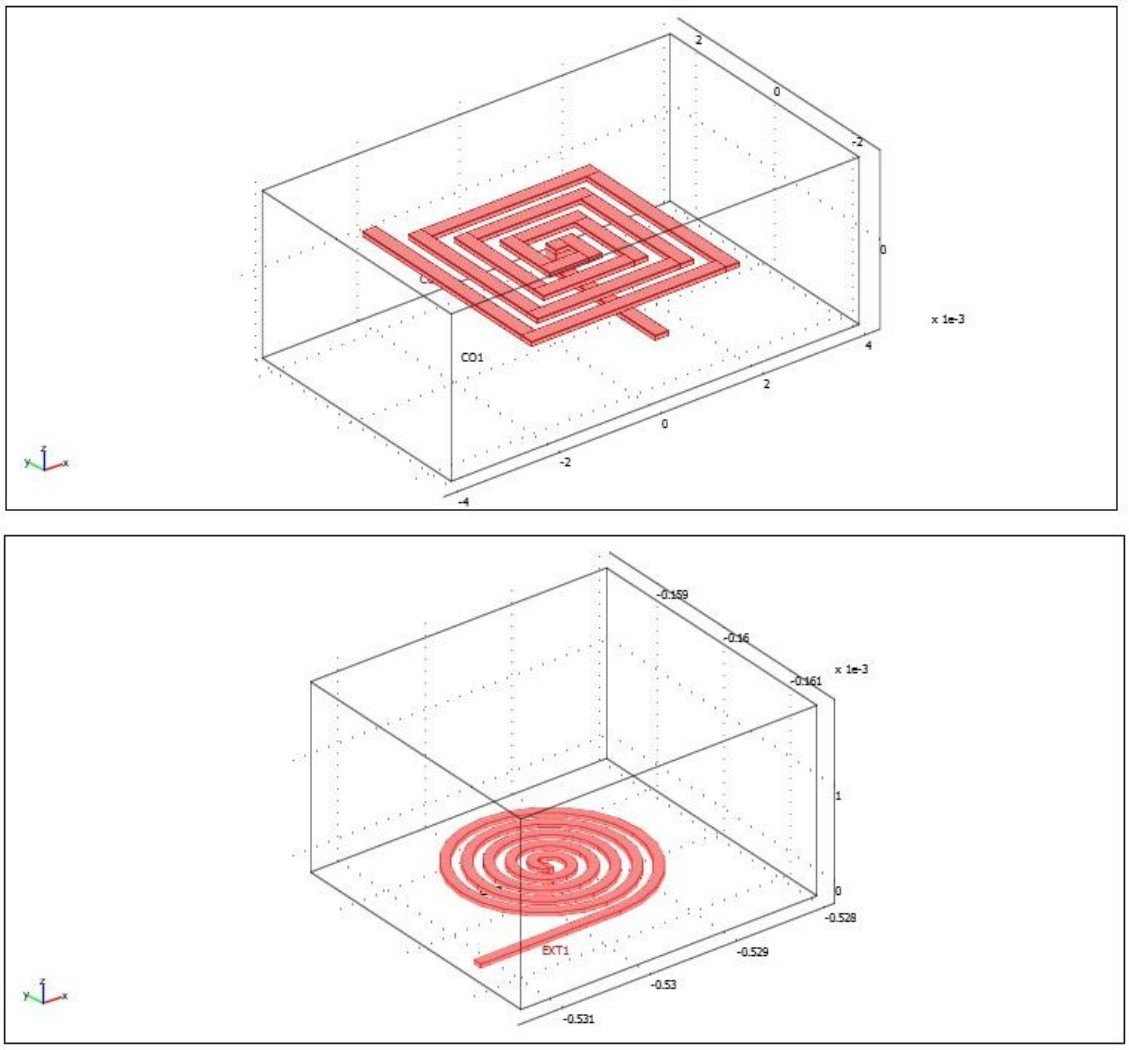


Figure 5-1: Designed geometries for the rectangular and spiral planar coils with 5 turns

Since the micromirror will be actuated in air the planar coils are enclosed in a cube represented by an air block. The material for the planar coil is chosen from the materials library to be copper with an electrical conductivity of $5.998\times10^{-7}$ S/m. The constitutive relation between the magnetic field $H$ and magnetic flux density $B$ is set to be $B = \mu_0\mu_r H$, as there is no external magnetic field or remanent

magnetic flux density in the coils. The relative permittivity for both the coils and the air block is set to be 1. The boundaries of the model require both magnetic and electric boundary condition due to the flow of current through the microcoils resulting in the generation of magnetic field. The sides of the air block that are in contact with the two terminals of the planar microcoils have electrical boundary condition of *ground* and *port* while the complete air block is set to *magnetic insulation* for the magnetic boundary conditions. The planar microcoil is set to have a *continuity* to magnetic potential and electric current. Each end of the planar microcoil is designated to be the *ground* and the *port*. The meshing of the model is performed using the free mesh parameters having a normal predefined tetrahedral mesh size. The model is solved with a parametric solver where the current is set to be the varying parameter in the range of 0 to 1 A with steps of 0.1 A. The postprocessing involves the predefined subdomain quantity of magnetic flux density which is plotted in complement to the geometry of the coil. Further probing of the magnetic flux density with measurements at varying height from the coil is also performed.

## 5.2 Resonant Frequency Simulations

Finite element simulations to predict the resonant frequency of the mirror structure is necessary to determine the single axis and dual axis operating scanning frequencies. Eigen frequency analysis determines the modes of actuation of the micromirror and enables the appropriate testing of the alpha and beta axis scanning. The resulting displacements at the different Eigen modes are used to calculate the angular displacement of the micromirror.

The geometries for the single axis straight torsion bar micromirror, single axis outer frame straight torsion bar micromirror and the dual axis with inner gimbal and outer frame straight torsion bar micromirror are designed. The third generation micromirror has the same design and dimensions as

the second generation micromirror and hence only the subdomain and boundary condition of the modeled were modified for simulation. The Figure 5-2 shows the geometries of the designs.

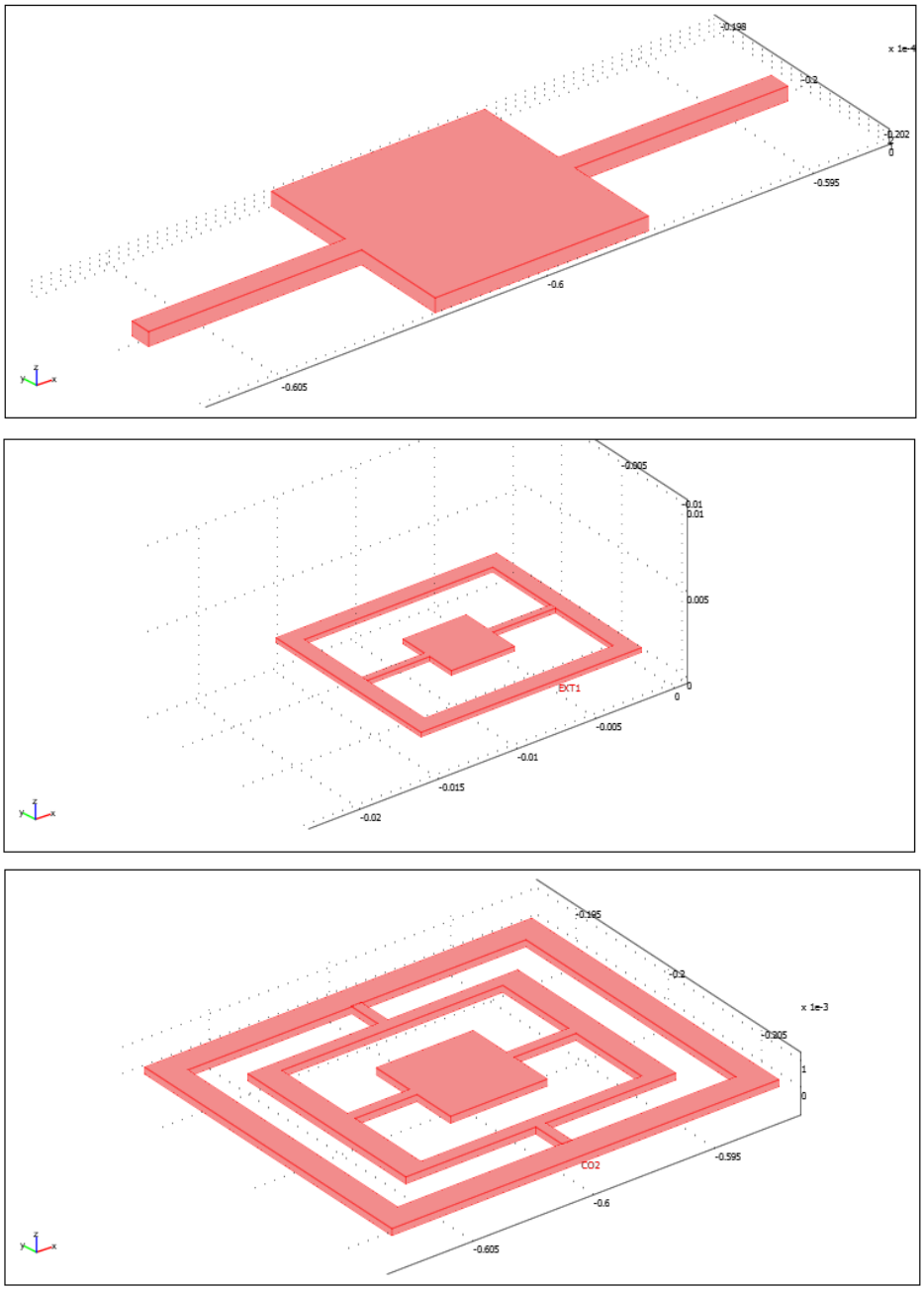


Figure 5-2: Designed geometries in COMSOL for the single and dual axis micromirrors

The *Solid, Stress-Strain* application mode under the *MEMS Module* of *Structural Mechanics* was chosen as the analysis module. Under this application mode Eigen frequency analysis was selected with the large deformations turned on, the weak constraints turned off and the constraint type was set to ideal. For the single axis straight torsion bar micromirror, the subdomain conditions of materials was manually entered since the parameters of the polymer composite was not found in the material library. The material parameters of Young's modulus, Poisson ratio, thermal coefficient of expansion and density was entered with the corresponding values of PDMS. The boundary conditions were set such that the flat edges on each end of the torsion bar are fixed while the rest of the structure is free.

The single axis outer frame straight torsion bar micromirror had two subdomains. The first being the mirror aperture and the torsion bars for which the material parameters were set corresponding to the values of PDMS and the second being the outer frame for which the material parameters of acrylic plastic or Plexiglas were set. This was done since the outer frame is glued onto the Plexiglas frame by the two-part epoxy. The boundary conditions were set such that the entire frame was fixed and the mirror and torsion bars were free. For the dual axis with inner gimbal and out frame, the outer frame was set with the material parameters of Plexiglas and the gimbal frame along with the mirror and torsion bars were set with the material parameters of PDMS. The boundary conditions of the outer frame were set to be fixed and the remaining structures were free.

The meshing of the model was similar to the previous planar microcoil simulation with normal tetrahedral mesh geometries. The solver was set to calculate for four desired number of Eigen frequencies. Post processing involved the measurement of the predefined boundary quantity of total displacement and the four Eigen mode shapes.

## 5.3 Magnetic flux density measurements

The magnetic field generated by the planar microcoils and the polymer magnetic micromirror is measured to relate the current versus the generated filed for the planar coil and to determine the location of maximum field of the micromirror in order to position the planar coils. The magnetic flux density of the polymer composite and the microcoils were measured using a Senis Linear Hall Probe Transducer [105].

The schematic of the magnetic measurement experimental setup is illustrated in the Figures 5-3 and 5-4. The measurement setup consisted of a THORLABS three-axis flexure stage on top of which a magnetic isolation of an inch of plastic is provided in the form of Lego ® blocks. The blocks house the microcoil connections for the coil magnetic measurements and the micromirrors for the mirror magnetic measurements. The linear hall probe transducer operates on the Hall magnetic principle. Accordingly a change in magnetic field brings about a change in the voltage level across the hall probe. The transducer is connected to a digital multimeter to record the change in the magnetic flux density. The microcoil is excited by a BK precision DC power supply. Since the magnetic field generated depends on the current flowing through the coil, a voltage of 3V is kept constant. This voltage selected limits the current to 1A which is the calculated ampacity for the planar microcoils. The current levels are set to be from 0.1 A to 0.9 A. The magnetic measurement of the planar coil is carried out by setting a current level and moving the flexure stage to record the magnetic flux density at every 400 microns (one turn of the micrometer). Magnetic measurements are initiated by locating the maximum magnetic flux density (at the center of the coil) and traversing the coil in all the three axes, one axis at a time. The image of the experimental set up is illustrated in Figure 5-5.

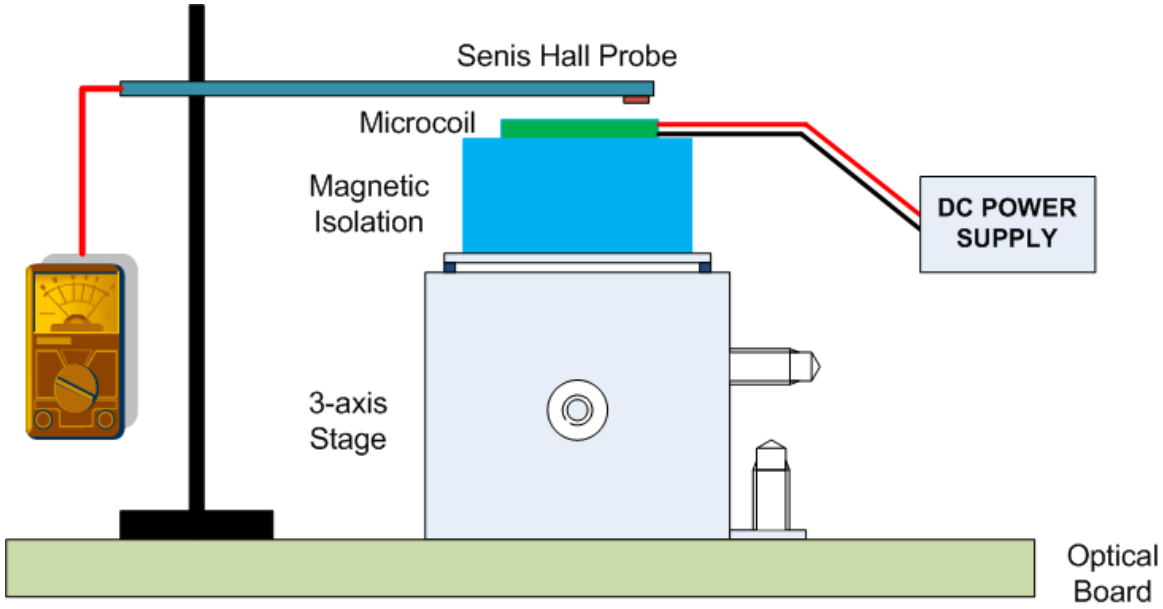


Figure 5-3: Schematic of the magnetic flux measurements for the planar microcoils

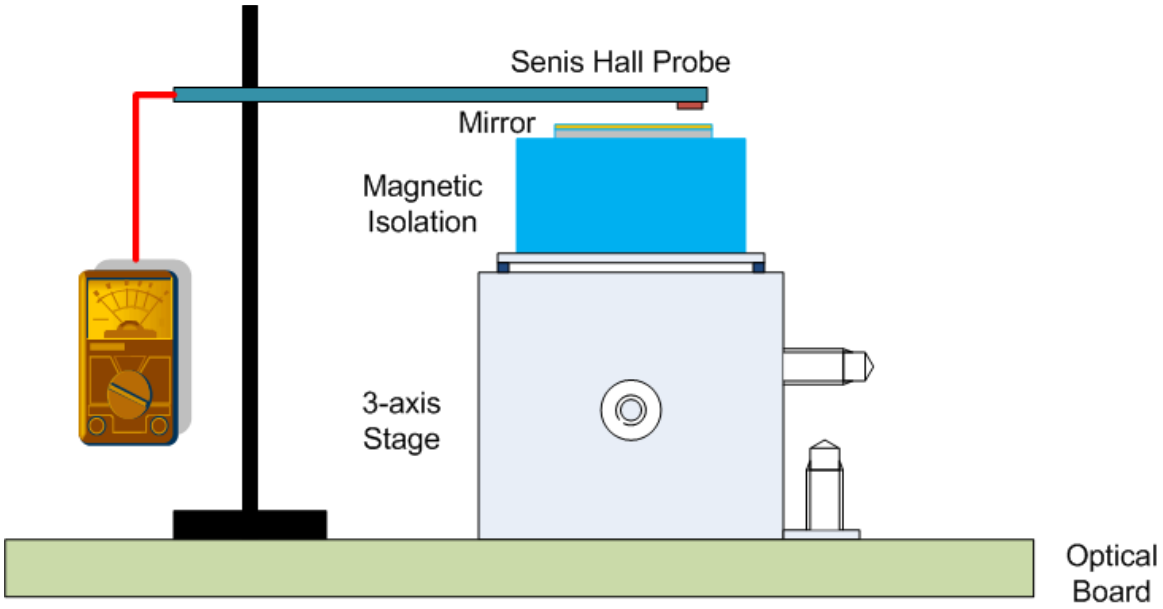


Figure 5-4: Schematic of the magnetic flux measurements for the polymer magnetic micromirrors

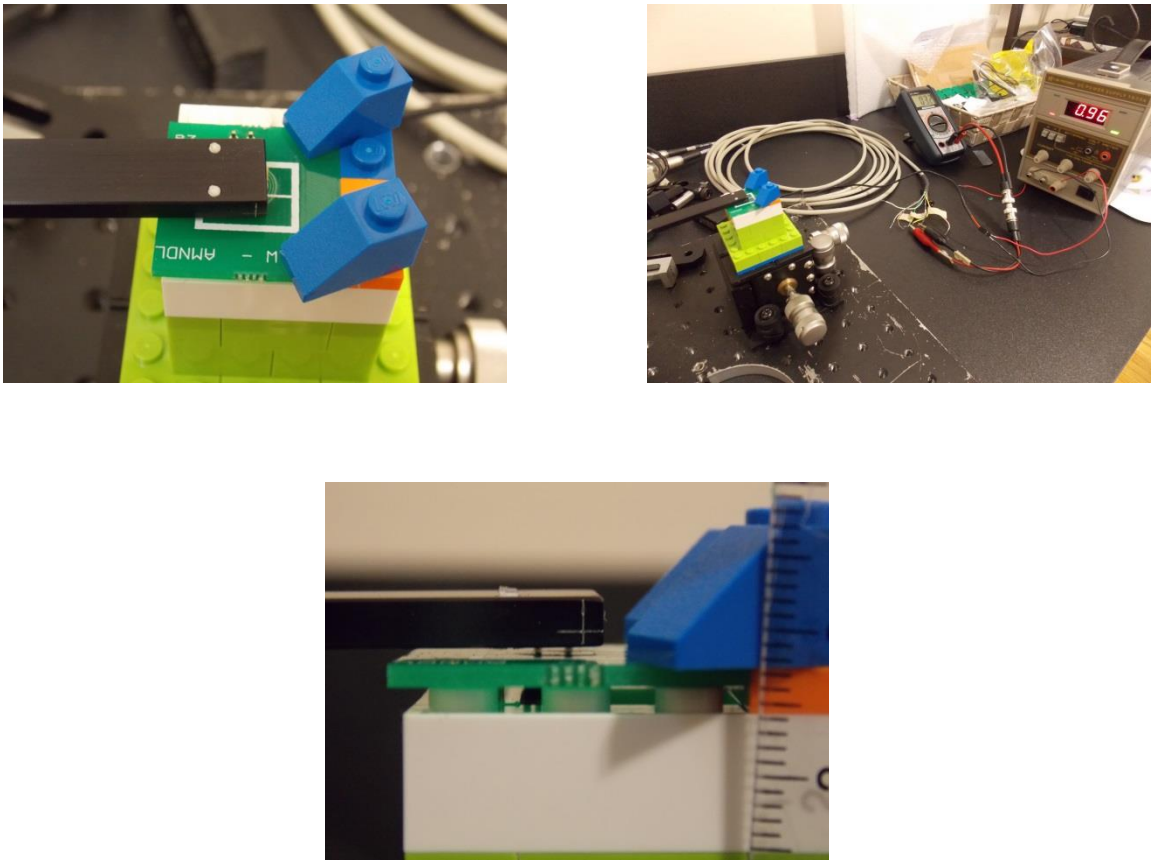

Figure 5-5: Experimental setup for magnetic flux measurement of microcoils and polymer magnetic micromirrors

## 5.4 Elasticity Measurements

Stress-strain experimentation to determine the breaking of the polymer composite with load and the Young's modulus was performed by an Instron 5548 Micro Tester [106]. Dog-bone structures of the polymer hard magnetic composite are fabricated according to the ASTM standard [107] using the laser machine to make the mold. The polymer magnetic composite is prepared and deposited into the mold and further demolded using precision tweezers. The testing was performed by clamping the ends of the dog-bone structure and pulling the structure along the gauge length. The machine outputs the load versus extension plot for each sample. Each test is carried out by pulling the sample at a

predefined load and strain rate on its ends till the sample breaks in the gauge length. The machine was set with a pretest load of 1.5 N/min/mm following a strain rate of 2.5 N/min/mm. The Figure 5-6 shows the microtensile tester and illustrates the fabricated polymer magnetic composite dog-bone structures.

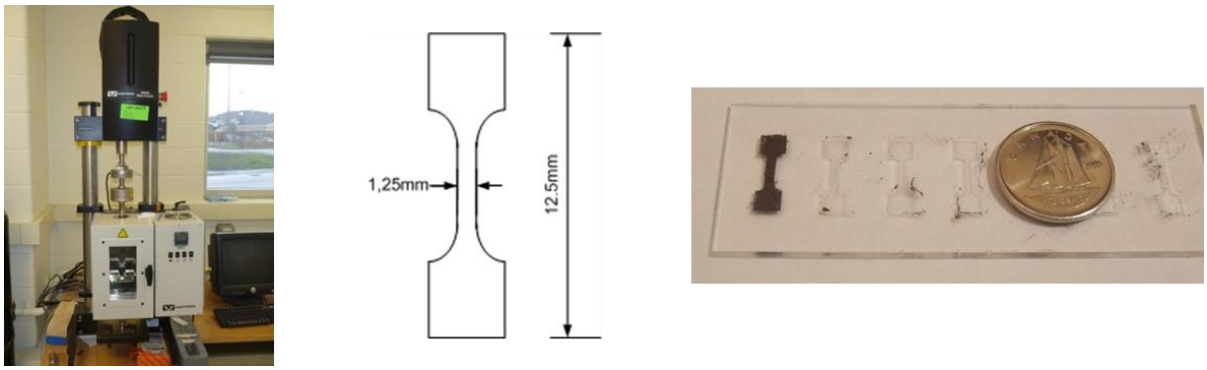


(a) (b) (c)

Figure 5-6: (a) Instron micro tensile tester; (b) ASTM standard Dog-bone schematic (c) Dog-bone polymer composite structures

## 5.5 Surface Roughness and Radius of Curvature Measurements

The square aperture mirror surface must be suitable to ensure the effective scanning of a target sample using an incident laser source. The surface roughness which influences the scanning clarity and resolution must be of acceptable optical standards. For laser applications, reflective surfaces must have a surface roughness less than $\lambda/10$ [108], where $\lambda$ is the wavelength of the incident laser beam. In addition the radius of curvature of the mirror affects the reflected angle of the incident laser beam. The presence of a low curvature presents a limitation on the linearity of the scanning angle and area of focus on the target sample.

Surface roughness measurements were performed using a WYKO NT1100 Optical Profiler [109]. The optical profiler is based on the principle of interference fringe patterns and can be used to

measure surface roughness on reflective surfaces that are nearly smooth such as metals or circuit boards. The optical profiler has range of 2mm with a vertical resolution of 3nm. The surface roughness measurements were performed on plain samples of cured polymer magnetic composite, samples deposited with undoped PDMS on top of the cured polymer magnetic composite and samples with PDMS and gold deposited on top of the cured polymer magnetic composite were performed.

Figure 5-7: WYKO NT1100 Optical Profiler

The radius of curvature measurements were performed using the National Instruments Vision Builder software [110]. Multiple images of the cross-sectional edge of the micromirror are obtained and processed through a user defined automated inspection program. The program step sequence consists of acquiring each image, performing the unit distance calibration, converting the image to grey scale using a grey scale filter, defining of the measurement area of interest, acquiring a straight edge and calculating the best circular fit on the area of interest. The automated inspection program performs the calculation for each image to provide the radius of curvature of the micromirror. From these calculations an average of the calculated radius of curvature measurements was obtained.

## 5.6 Micromirror actuation measurements

The actuation of the polymer magnetic mirror was performed both in the static conditions (DC mode) and the dynamic conditions (AC mode) to measure the actuation performance. An optical setup was built to measure the angular displacement of the polymer magnetic mirrors in both conditions. The optical setup was assembled on a 1’ × 1’ optical board and consisted of the mounted polymer composite micromirror with microcoil electrical connections, a laser card module as the illumination source of wavelength 635 nm with a beam spot of 1mm and a mounted grid sheet onto which the reflected beam spot is projected. The grid sheet onto which the reflected beam spot is projected is fixed at a measured distance from the micromirror for angular displacement measurements.

### 5.6.1 Static actuation measurements

A programmable power supply (BK Precision, Model 1788, Single output DC) was used to conduct static mode experiments to measure the angular displacement of the bidirectional scanner. The DC power supply is connected to the microcoil of resistance 0.05Ω. Six trials were performed at no load voltages levels of 1V, 2V, 4V, 6V, 8V and 10V, and in each case the current was increased from 0A to 0.95A in steps of 0.1A. The full load output voltage ranged between 0V to 132mV. The change in position of the reflected beam with change in current is observed and measured. The angular displacement is calculated by measuring the distance between the mirror and the grid sheet and the displacement of the reflected laser beam on the grid sheet. The tangent angle between the mirror and the displaced position of the laser beam gives the angular displacement.

### 5.6.2 Dynamic actuation measurements

A function generator (BK Precision, Model 4084, Arbitrary function generator) was used to conduct dynamic mode experiments to measure the angular displacement. This includes angular displacement

with varying frequency as well as determining the resonant frequency of the polymer magnetic micromirrors. Keeping a constant peak to peak voltage, the frequency was swept from 1 Hz to 90 Hz. Four trials were performed by setting peak to peak voltages of 5V, 10V, 15V and 20V ($V_{rms}$: 1.76V, 3.53V, 5.30V and 7.07V respectively). With the microcoil resistance of 0.05Ω and output impedance of 50Ω, the current through the microcoil is calculated to be 35.55 mA, 70.71 mA, 106.06 mA and 141.42 mA respectively. The mechanical resonant frequency for the structure was determined visually by varying the frequency of the function generator to observe the maximum increase in the length of the reflected laser scan pattern.

The schematic of the optical angle measurement is shown in the Figure 5-8. The optical angle is calculated by the equation, $a = \frac{1}{2} \times arctan \frac{l}{a}$.

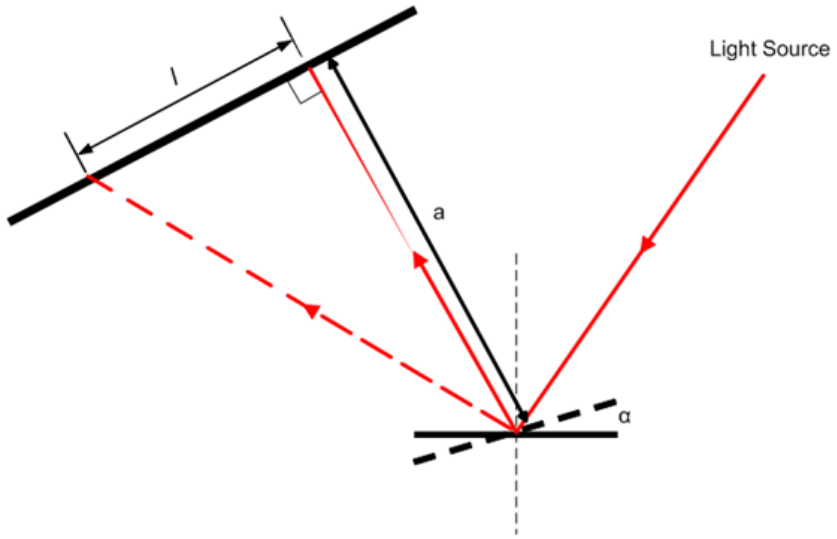


Figure 5-8: Schematic of optical angle measurement

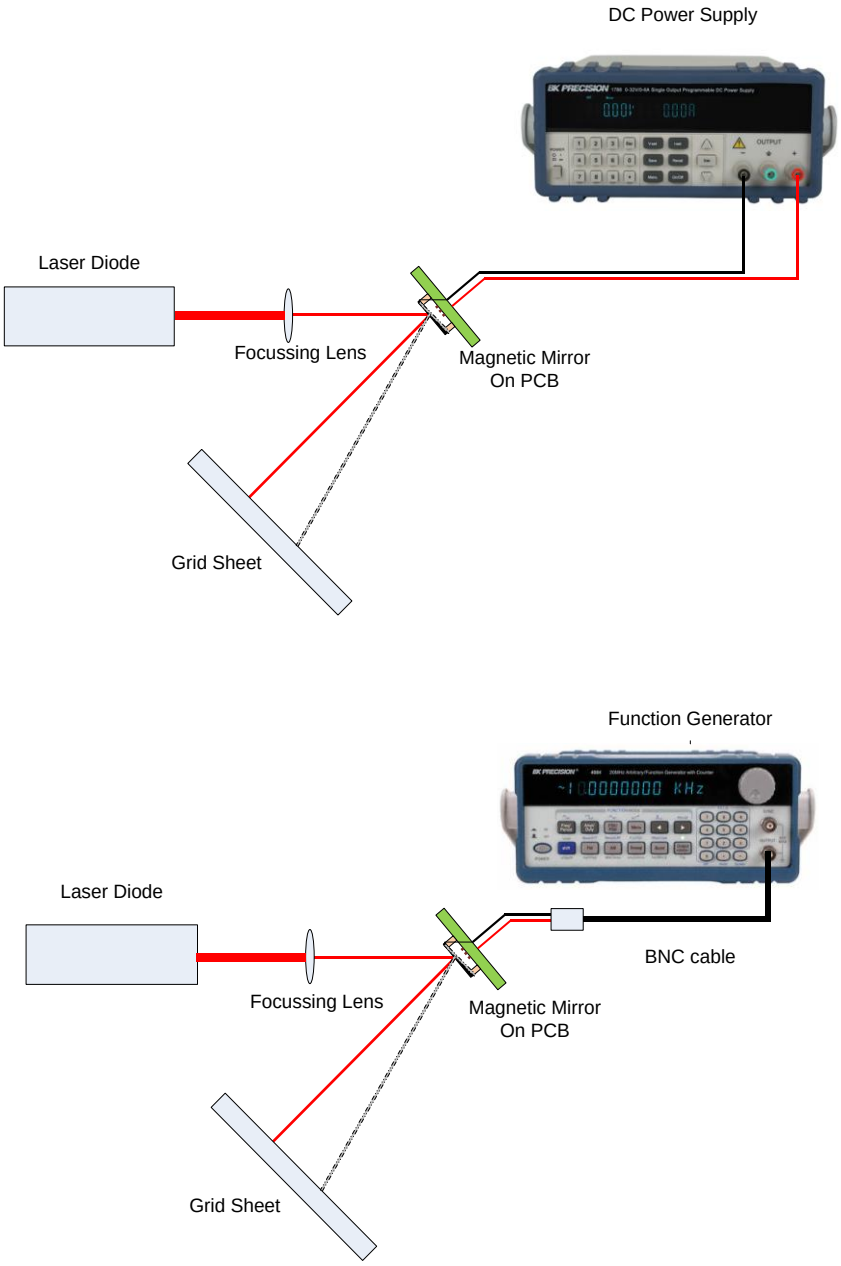


Figure 5-9: Schematic of dynamic angular displacement experimental setup

# Chapter 6: Results and analysis

## 6.1 Microcoil magnetic flux density simulation results

Magnetic flux density simulations were performed on both the rectangular and spiral planar coils. The lateral dimensions, the vertical dimensions and the number of turns were defined as per the aforementioned designs. Parametric simulations were performed varying the current flowing through the microcoils from 0.1 A to 1 A with a step of 0.1 A. The magnetic flux densities across the center of the coil with varying currents and vertical displacements were obtained. The Figure 6-1 shows the magnetic flux density distribution of the excited spiral planar coil.

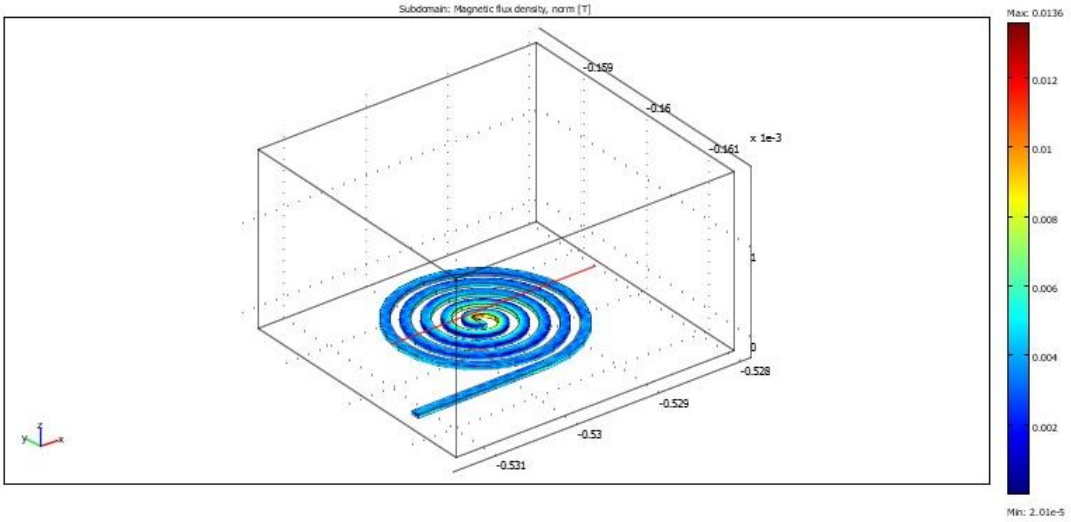


Figure 6-1: Magnetic flux density distribution of the excited spiral planar coil

The Figures 6-2 show the magnetic flux density across the center of the rectangular planar microcoil at different vertical distances from the surface of the microcoil. The x-axis represents the cross sectional length of the microcoil in millimeters and the y-axis represents the magnetic flux density in Tesla at each point of the z-plane. Each colored line plot represents the ten current levels from 0.1 A to 1 A in steps of 0.1 A.

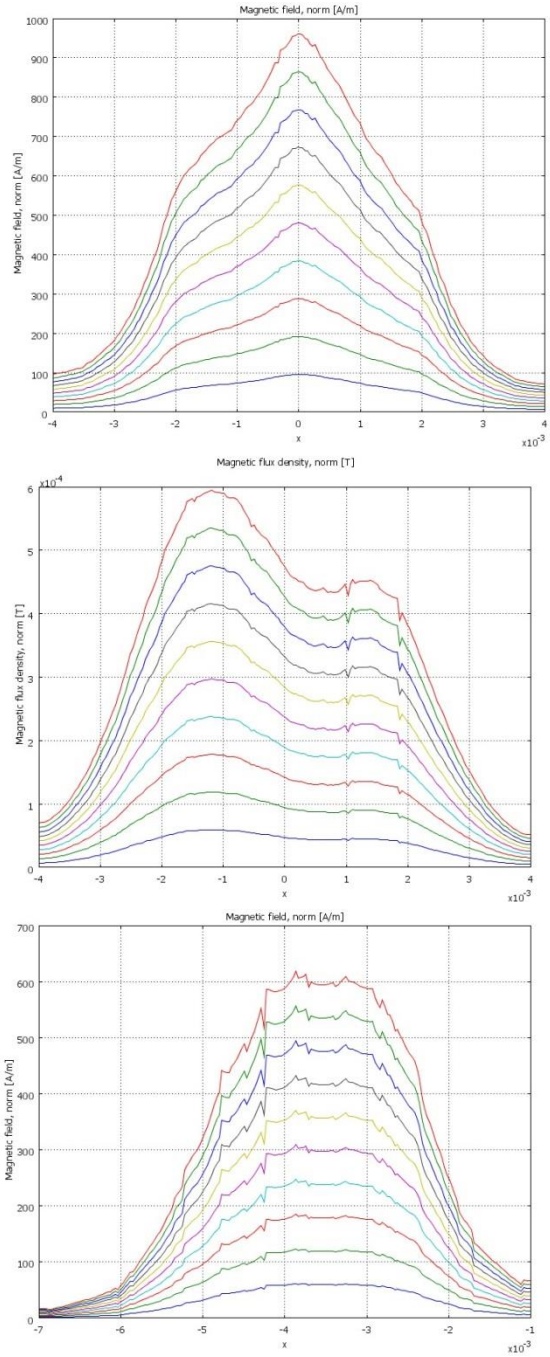


Figure 6-2: Magnetic flux density simulations on the rectangular planar microcoil; x-axis represents the position of the coil in mm and the y-axis represents the magnetic field in Tesla

The above plots show the inverse cubed relation of the magnetic flux density versus the vertical displacement from the microcoil. It can be observed that the magnetic flux density for the 5 turn microcoil is significantly lower than the 10 turn microcoil. Although this is an advantage, designing microcoils with several turns results in a larger real estate of the device. The maximum magnetic flux density at the optimum vertical displacement determines the gap spacing between the micromirror and the planar coil. The Figure 6-3 illustrates the magnetic flux density simulations on the spiral planar microcoils.

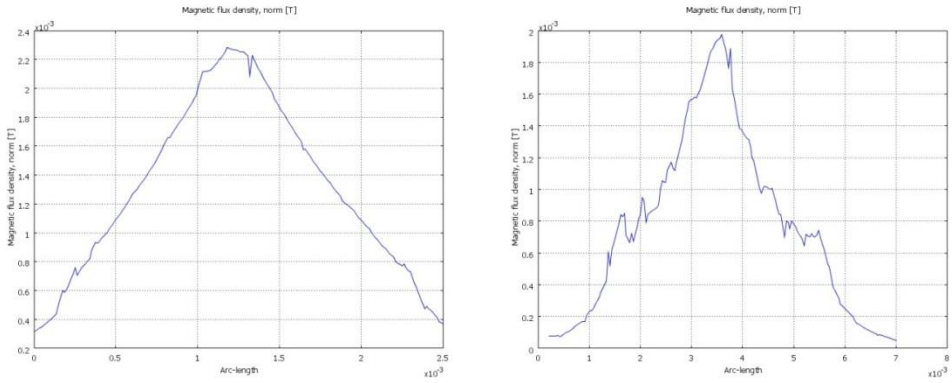


Figure 6-3: Magnetic flux density simulations on the spiral planar microcoil; x-axis represents the position of the coil in mm and the y-axis represents the magnetic field in Tesla

The results of the spiral planar microcoils show a lower magnetic flux density due to the smaller trace widths of the coils. In order to reduce the real estate of the device, 127µm trace width and 200 µm trace width microcoils with 5 turns and 10 turns were designed. The aforementioned spiral microcoil designs (1a, 1b, 2a, 2b, 3a, 3b and 4a) were simulated to obtain the magnetic flux density values at varying vertical displacements.

## 6.2 Resonant frequency simulation results

The geometries for the single axis straight torsion bar micromirror with no gimbal, single axis outer frame straight torsion bar micromirror and the dual axis with inner gimbal and outer frame straight

torsion bar micromirror were simulated to obtain the Eigen frequency modes which in turn determine the operation modes for the dynamic actuation of the polymer magnetic micromirror. The third generation micromirror has the same design and dimensions as the second generation micromirror and hence only the subdomain and boundary condition of the modeled were modified for simulation. Four desired Eigen frequencies were calculated for each design. The Figure 6-4 illustrates the mode shapes for the straight torsion bar micromirror.

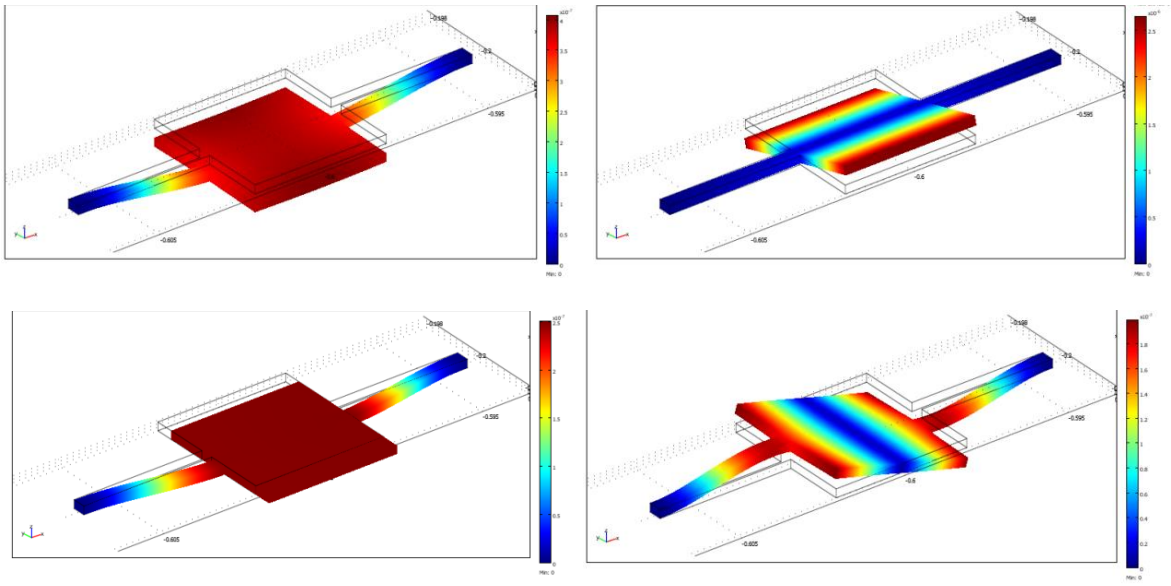

Figure 6-4: Mode shapes of the no gimbal straight torsion bar micromirror

The first mode shape represents the out-of-plane motion, the second mode shape represents the first torsional motion, the third mode shape represents the in-plane motion and the fourth mode shape represents the second torsional motion of the micromirror. Since the significant mode shape for the operation of the micromirror is the first torsional motion, the maximum displacement at the edge of the mirror was observed. The Figure 6-6 illustrates the six mode shapes of the dual axis outer frame inner gimbal micromirror. Six desired Eigen frequencies were calculated to visualize the out of plane mode shapes for both the mirror aperture and the inner gimbal frame.

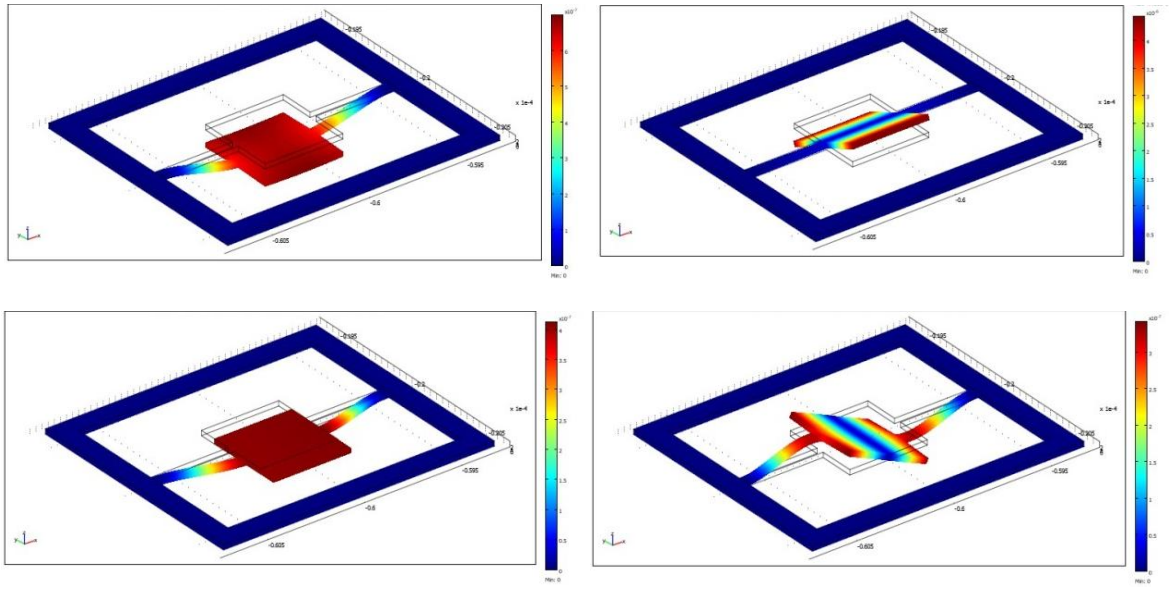

Figure 6-5: Mode shapes of the outer frame straight torsion bar micromirror

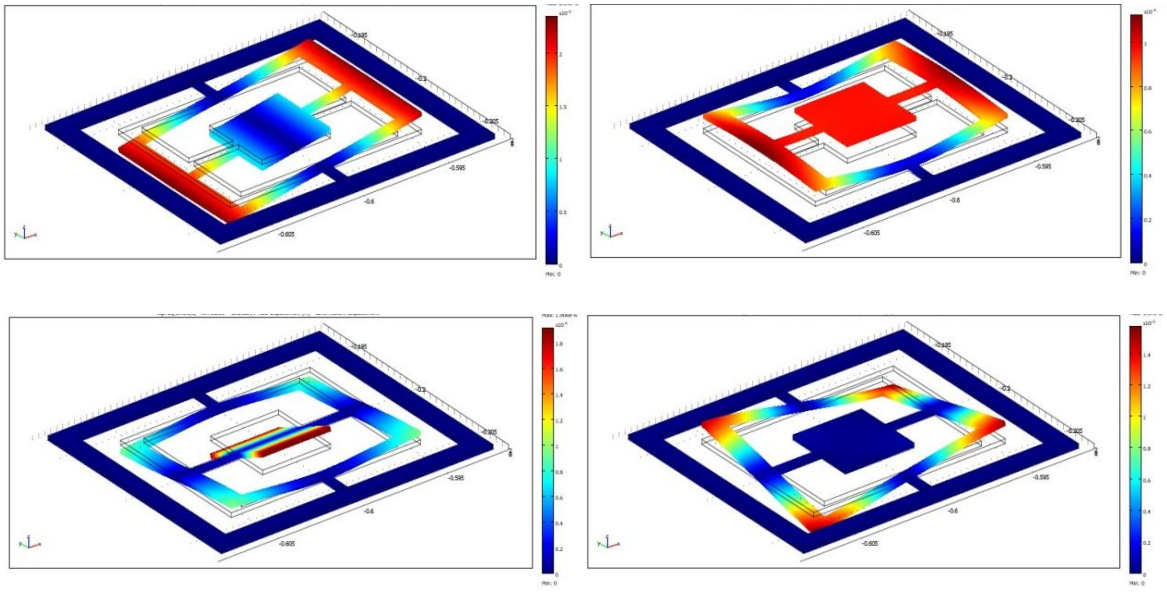

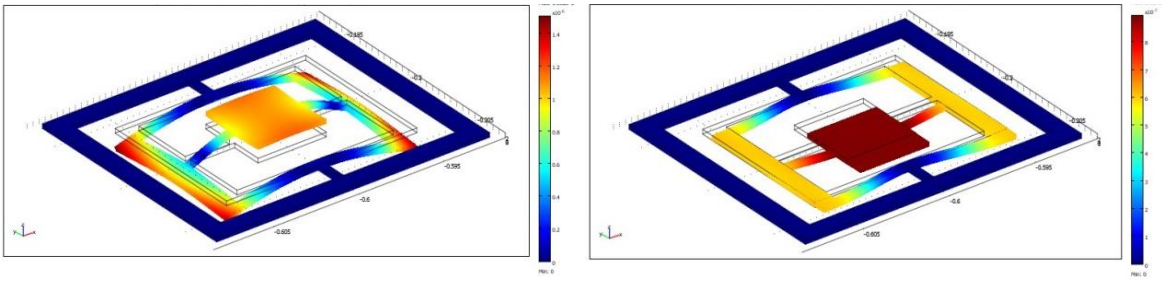

Figure 6-6: Mode shapes of the dual axis outer frame inner gimbal straight torsion bar micromirror

Among the six mode shapes that occur for the dual axis micromirror, the mode shapes of relevance for the operation of the micromirrors as a scanner are the first and third mode shape. The simulation results for the mode shapes provide an understanding of the deflection of the mirror with the change in frequency.

## 6.3 Magnetic flux density measurement results

### 6.3.1 Microcoil Measurement results

Lorentz force interaction between the magnetic field of the polymer mirror and the planar coil leads to the bidirectional actuation of the micromirror. The rectangular and spiral planar coils with the aforementioned design parameters were excited at various current levels as described in the previous chapter. The maximum field generated by the planar coil is limited by the ampacity of the planar coils which further determines the gap spacing between the coil and the mirror. The maximum magnetic flux densities for each design are provided in the table. The Figure 6-7 illustrates the magnetic flux density versus for the x, y and z directions of the spiral planar microcoil.

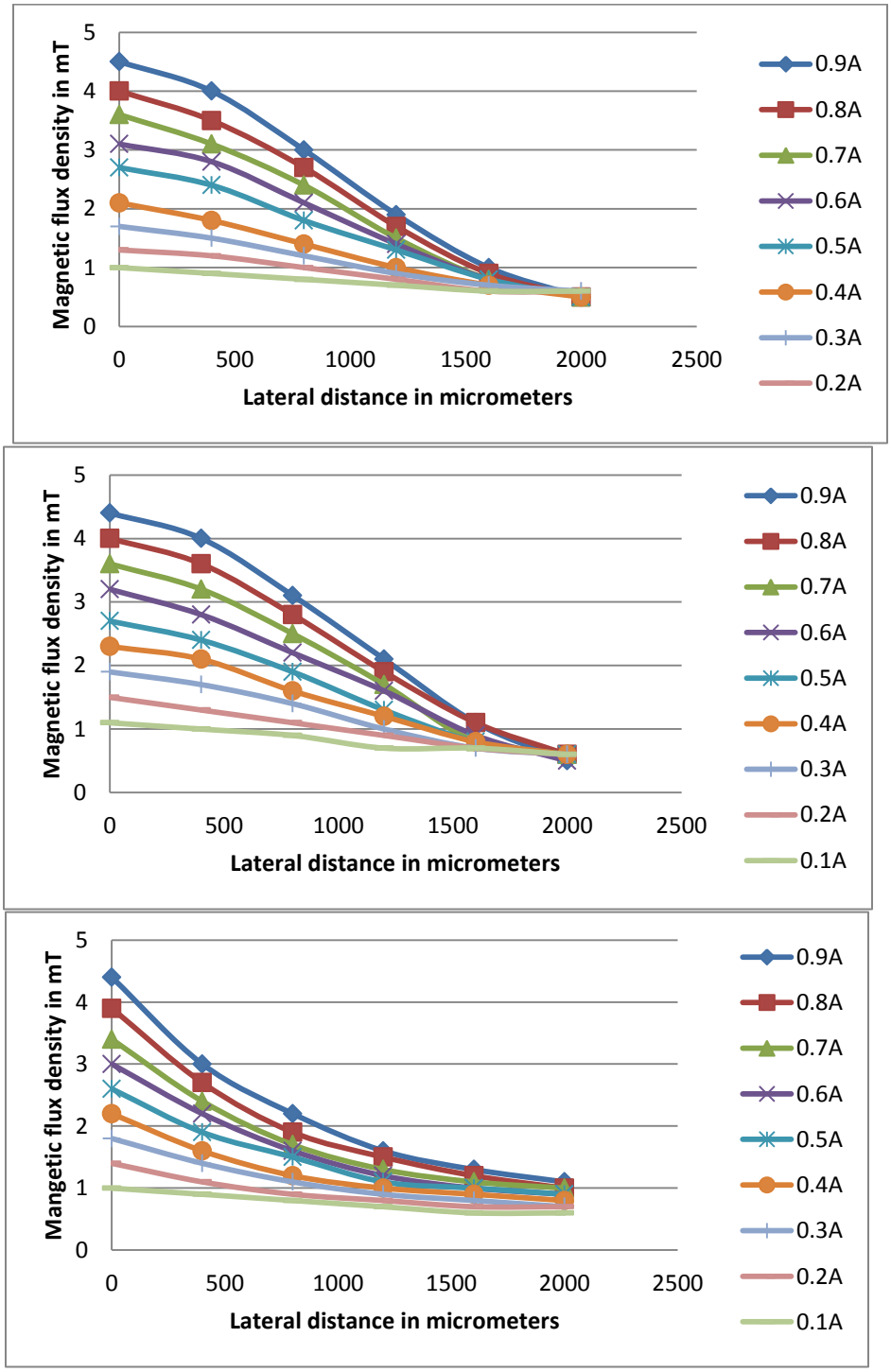


Figure 6-7: x, y and z axis magnetic flux density measurements for Design 1a spiral planar microcoil

In the above plots, the x axis represents the distance traversed by the Senis Linear Hall Probe Transducer. The origin is experimentally set to be the center of the microcoil where the magnetic flux density is maximum. Since the spiral planar microcoil is symmetric about the center of the coil, the origin is experimentally set as the center. The y axis represents the magnetic flux density in Tesla. The plot of the magnetic flux density in the z direction shows the inverse cubed relation of the magnetic flux density versus the vertical displacement.

### 6.3.2 Micromirror Measurement results

Following the squeegee coating, curing and demolding of the mirror structures, gold deposition was performed on all the micromirror designs. Further the micromirrors were magnetized using a GMW 3470 electromagnet at a magnetic field of 1.8 T. The remanent magnetic flux densities of the polymer hard magnetic structures must be measured in order to understand the Lorentz force actuation of the micromirror. The magnetic flux density measurements were performed at particular locations of the micromirror. For the single axis torsion bar micromirror, the measurements were performed at the four edges of the square aperture and the middle of the square aperture. For the single axis outer frame straight torsion bar micromirror, the measurements were performed same as the previous design but in addition measurements were also performed at the top left corner, top right corner, bottom left corner, bottom right corner of the outer frame and the four gaps around the torsion bar and square aperture. The distance at which the maximum magnetic flux density was observed was set to be the distance at which the measurements were performed. It can be observed that the magnetic flux densities in the gap between the frames and gimbal structures and around the square aperture are comparable to the values of the structures themselves. This is caused due to inherent magnetic field of the structures which causes the magnetic interaction in the gap spacing. This was also illustrated by the deformation of the dual axis micromirror at equilibrium condition. The micromirrors with

undoped PDMS as the outer frames show a significant decreases in the magnetic flux densities at the gap spacing.

## 6.4 Elasticity measurement results

The load tests performed on the polymer magnetic composite dog-bone structures using the Instron micro tensile tester provides the load versus extension plot for each sample. From this information, the Young`s modulus can be calculated. Three samples were tested and the results are presented below. Experimentation showed that all the three samples were elongated and were broken in the gauge length suggesting uniform thickness of the structure and the good fabrication of the polymer magnetic composite. The load tests were compared between magnetized samples and unmagnetized samples. The results obtained did not show any high variation in the curves and the breaking points. The Figure 6-8 illustrates the load vs extension plots of the three dog-bone samples.

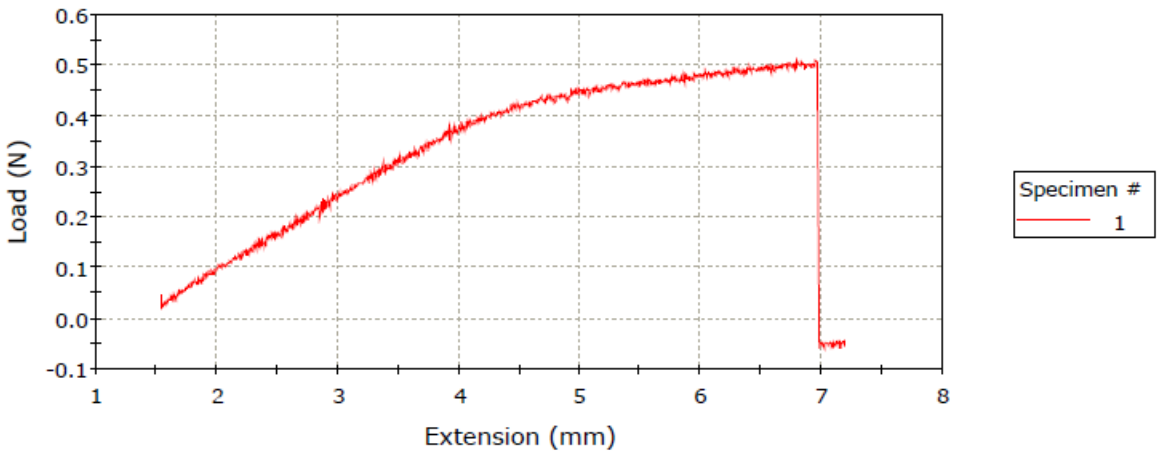


| | Load at Break (Standard) (N) | Time at Break (Standard) (sec) | Displacement (Strain 1) at Break (Standard) (mm) | Average strain at Break (Standard) (%) |
|---|---|---|---|---|
| 1 | -0.04552 | 135.80001 | 7.18585 | 359.29262 |

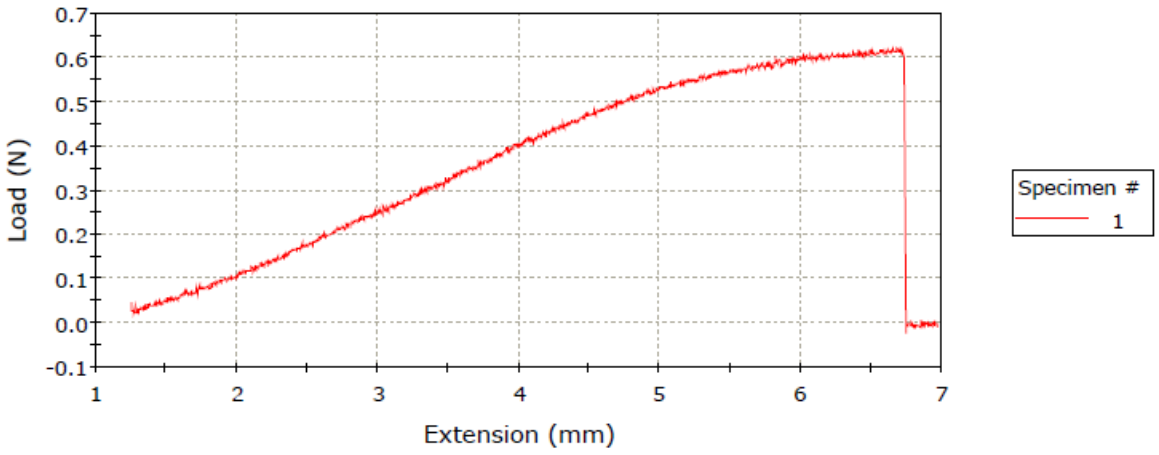


| | Load at Break (Standard) (N) | Time at Break (Standard) (sec) | Displacement (Strain 1) at Break (Standard) (mm) | Average strain at Break (Standard) (%) |
|---|---|---|---|---|
| 1 | -0.00999 | 137.52801 | 6.97451 | 348.72565 |

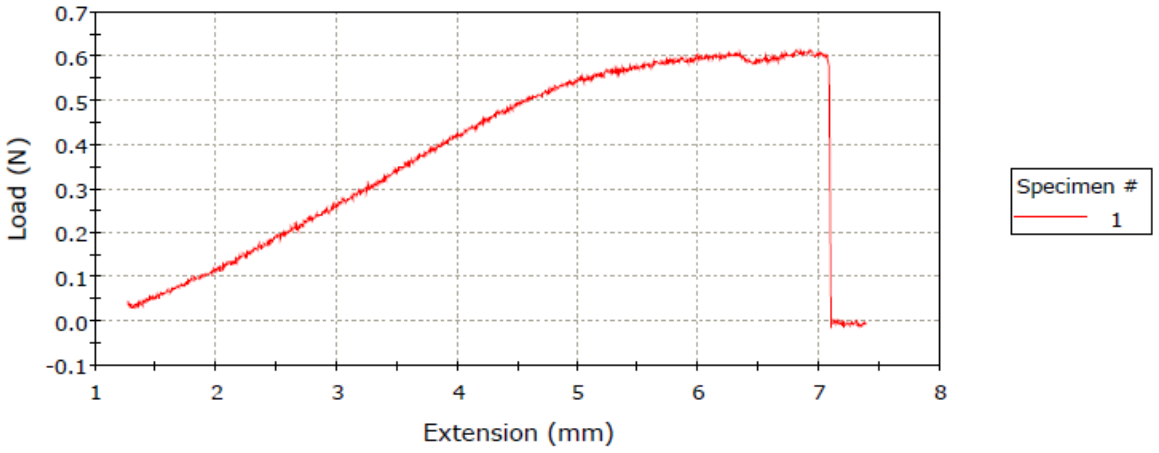


| | Load at Break (Standard) (N) | Time at Break (Standard) (sec) | Displacement (Strain 1) at Break (Standard) (mm) | Average strain at Break (Standard) (%) |
|---|---|---|---|---|
| 1 | -0.00556 | 147.06001 | 7.38811 | 369.40567 |

Figure 6-8: Microtensile stress strain experimental results

The breaking point of the polymer composite was at approximately 0.5N for the first sample while it was 0.6N for the second and third sample. The elongation before breakage was around 7 mm for all

the three samples. The Young's modulus for the samples was calculated from the stress strain relationship and was found to be 1.8 Mega Pascal. The load at break value in the plots represents the value of the load after the dog-bone structure is broken in the gauge length. The values of extension and load are used to calculate the Young's modulus. The stress is given by the ratio of the load and the cross-sectional area of the sample and the strain is given by the ratio of the extension of the sample and the original length of the sample.

## 6.5 Surface roughness measurement results

Initial surface profilometry of the mirror yielded an average surface roughness of 165 nm with a low radius of curvature of 75 mm. From the least square method, the peak-to-valley surface flatness should be less than $\lambda/10$, to be suitable for laser applications [108]. In order to reduce the surface roughness and increase the radius of curvature, a thin layer of PDMS was micropipetted on the square aperture prior to gold deposition. The modified fabrication process flow is illustrated in the Figure 6-9.

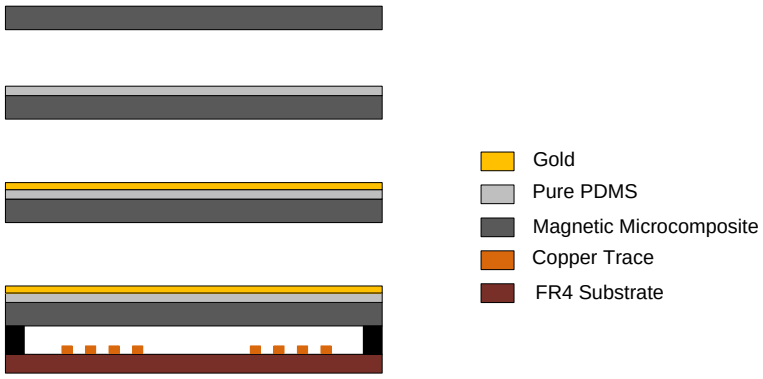


Figure 6-9: Surface modification process flow using PDMS

The Figure 6-10 shows plain samples with a surface roughness of 121.46 nm, samples with PDMS with a roughness of 83.14 nm and finally samples with PDMS and gold with a roughness of 66.24

nm. The overall curvature of the mirror after integration was measured to be 321.37 mm. This increase in the radius of curvature is a result of the PDMS surface smoothening layer that was micropipetted onto the mirror aperture.

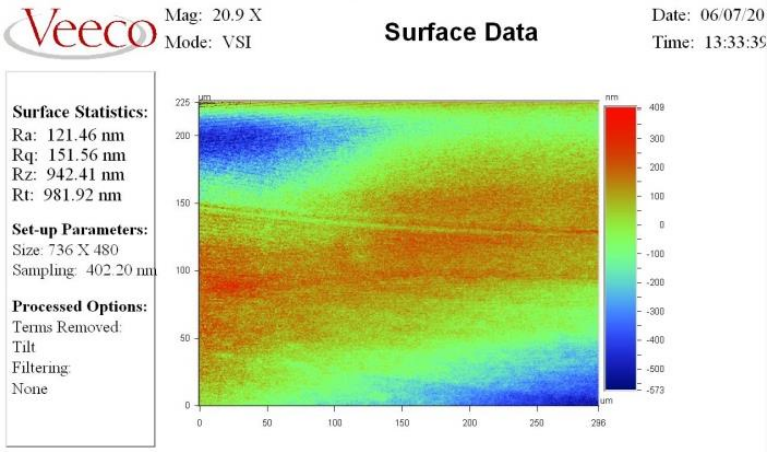


(a)

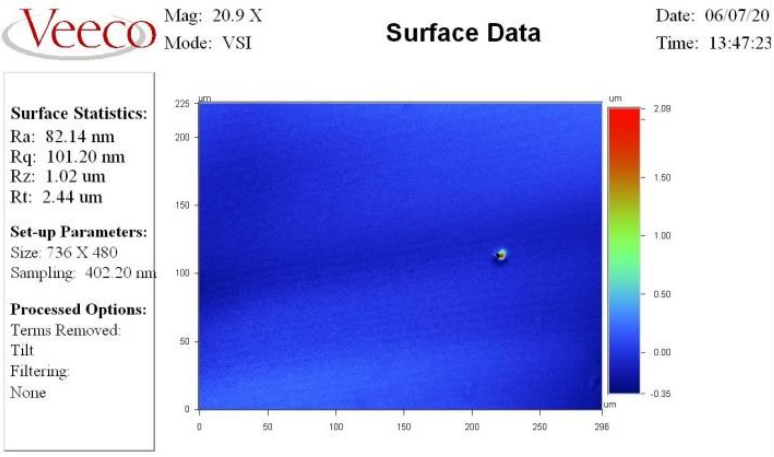


(b)

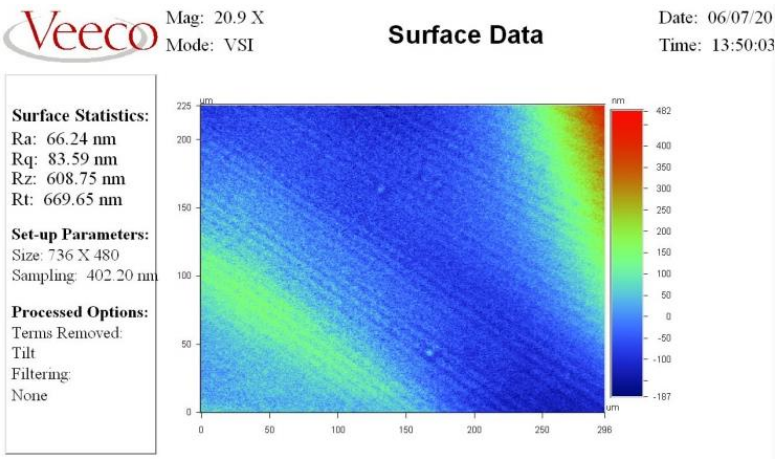


(c)

Figure 6-10: Surface roughness measurement data for (a) Plain polymer composite sample; (b) Polymer composite with PDMS layer; (c) Polymer composite with PDMS and gold layer

## 6.6 Micromirror actuation measurement results

### 6.6.1 Static actuation measurement results

The static mode actuation of the micromirrors was performed using a programmable DC power supply. The change in position of the reflected beam with change in current is observed and measured. The angular displacement is calculated by measuring the distance between the mirror and the grid sheet and the displacement of the reflected laser beam on the grid sheet. The tangent angle between the mirror and the displaced position of the laser beam gives the angular displacement. The plot below shows the angular displacement versus the current supplied for the first generation single axis straight torsion bar mirror. The maximum angular displacement of 18 degrees (mechanical) is observed at a voltage of 10 V and a current of 0.95 A. Increasing the gap spacing between the micromirror and planar coil shows a decrease in the angular displacement

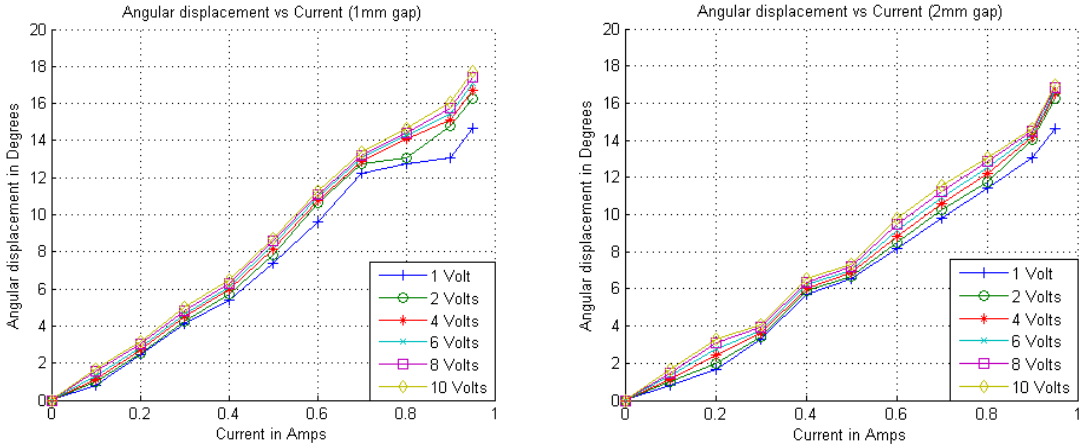


Figure 6-11: Static response of mirror angular displacement against current for gap of 1mm and 2mm

The Figure 6-12 shows the static response of the second and third generation single axis outer frame straight torsion bar micromirror. It can be observed that the angular displacement is lesser for the second generation micromirror than compared to the third generation micromirror due to the magnetic influence of the magnetic outer frame over the inner torsion bars and mirror aperture. Compared to the first generation, the angular displacement is lower due to the fixed constraint of the torsion bars and the lower magnetic flux density generated by the spiral microcoils of smaller trace widths.

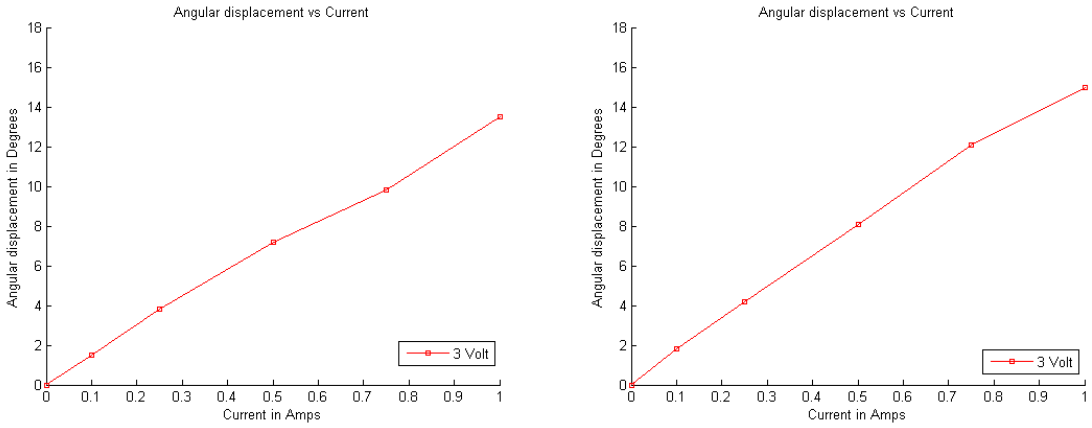


Figure 6-12: Static response of mirror angular displacement against current for the second generation and third generation single axis straight bar micromirror

The Figures 6-13 illustrate the alpha axis static response of the second and third generation dual axis outer frame inner gimbal straight torsion bar micromirror. As previous the angular displacement of the third generation micromirror is higher compared to the second generation micromirror due to the absence of magnetic interaction between the frame and the gimbal structure. The angular displacement is lower compared to the single axis micromirrors due to the increase in the overall mass and area of the micromirror.

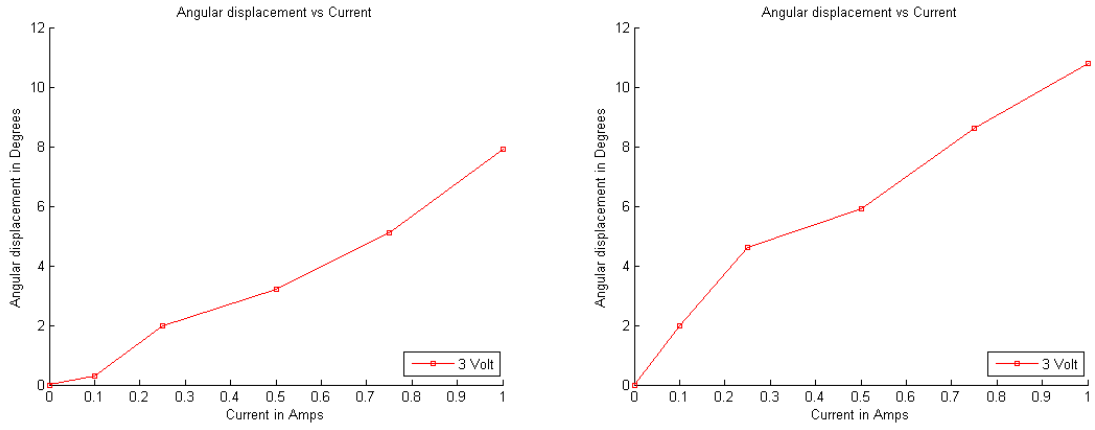


Figure 6-13: Static response of alpha axis angular displacement against current for the third generation dual axis outer frame inner gimbal straight torsion bar micromirror

The Figures 6-14 illustrate the beta axis static response of the second and third generation dual axis outer frame inner gimbal straight torsion bar micromirror. The angular displacement of the third generation micromirror is higher compared to the second generation micromirror due to the absence of magnetic interaction between the frame and the gimbal structure. The displacement in the beta axis is significantly lesser than the displacement in the alpha axis. The design of the dual axis micromirror affects the actuation since the entire gimbal frame, the torsion bars and the mirror is attracted by the planar coils. This significant increase in the mass of the structure upon which the Lorentz force is

acting results in a lower angular deflection for the same current levels. It can be observed that all the plots for the static response follow a similar trend suggesting the linear actuation of the micromirrors.

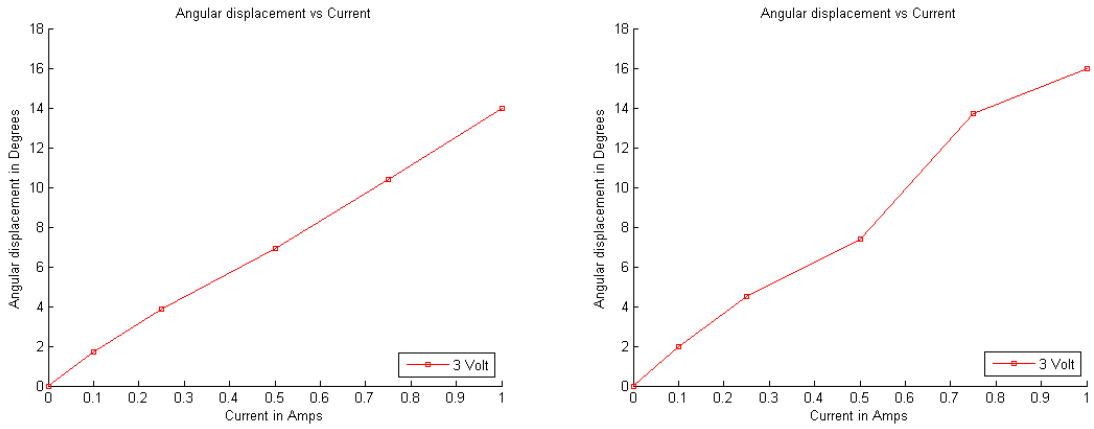


Figure 6-14: Static response of beta axis angular displacement against current for the third generation dual axis outer frame inner gimbal straight torsion bar micromirror

### 6.6.2 Dynamic actuation measurement results

The dynamic mode actuation of the micromirrors was performed using a function generator. The change in position of the reflected beam with change in frequency is observed and measured. The angular displacement is calculated by measuring the distance between the mirror and the grid sheet and the displacement of the reflected laser beam on the grid sheet. The tangent angle between the mirror and the displaced position of the laser beam gives the angular displacement. The plot below shows the angular displacement versus the change in frequency for the first generation single axis straight torsion bar mirror. The maximum angular displacement of 15 degrees (mechanical) is observed at a peak to peak voltage of 20 V. Increasing the gap spacing between the micromirror and planar coil shows a decrease in the angular displacement.

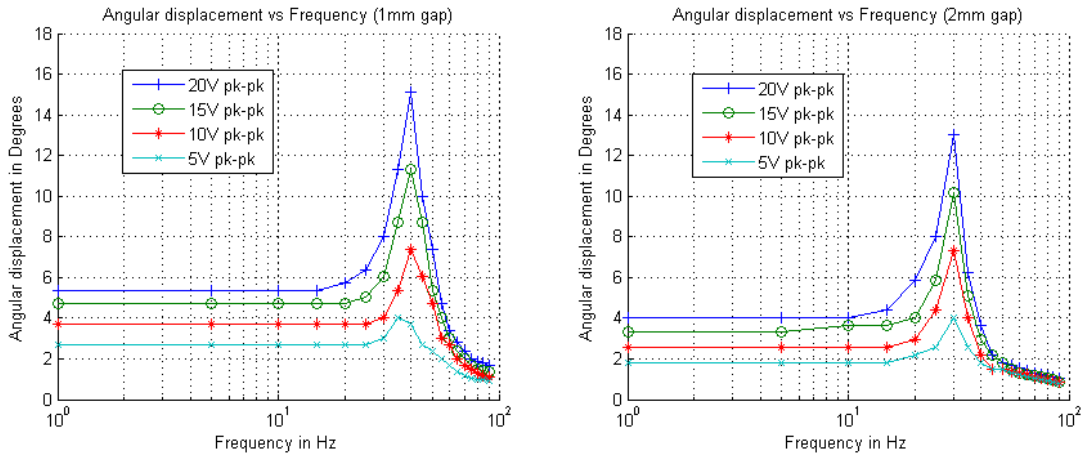


Figure 6-15: Dynamic response of mirror angular displacement against frequency for 1mm, 2mm gap

The Figure 6-16 shows the dynamic response of the second and third generation single axis outer frame straight torsion bar micromirror. The angular displacement is lesser for the second generation micromirror than compared to the third generation micromirror due to the magnetic influence of the magnetic outer frame over the inner torsion bars and mirror aperture. The resonant frequency is higher compared to the first generation due to the stiffness resulting from the fixed constraint of the torsion bars and the lower magnetic flux density generated by the spiral microcoils of smaller trace.

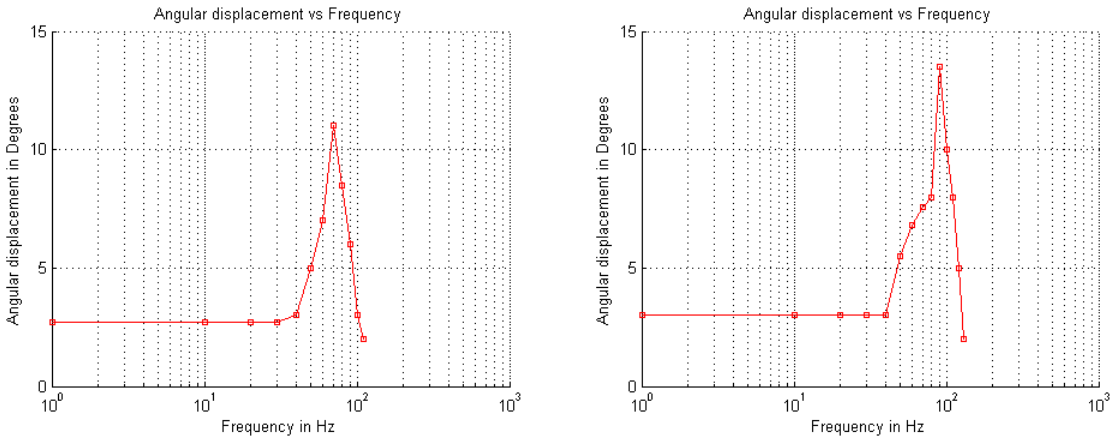


Figure 6-16: Dynamic response of mirror angular displacement against frequency for the second generation and third generation single axis straight bar micromirror

The Figures 6-17 illustrate the alpha axis dynamic response of the second and third generation dual axis outer frame inner gimbal straight torsion bar micromirror. As previous the angular displacement of the third generation micromirror is higher compared to the second generation micromirror due to the absence of magnetic interaction between the frame and the gimbal structure. The angular displacement is lower and the resonant frequency is higher compared to the single axis micromirrors due to the increase in the overall mass and area of the micromirror.

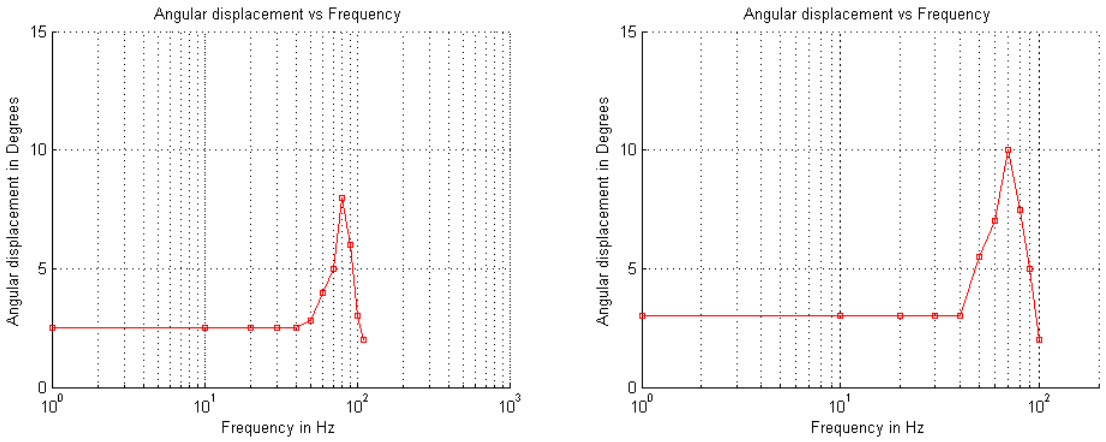


Figure 6-17: Dynamic response of alpha axis angular displacement against frequency for the third generation dual axis outer frame inner gimbal straight torsion bar micromirror

The Figures 6-18 illustrate the beta axis dynamic response of the second and third generation dual axis outer frame inner gimbal straight torsion bar micromirror. The angular displacement of the third generation micromirror is higher compared to the second generation micromirror due to the absence of magnetic interaction between the frame and the gimbal structure. This also explains the change in the resonant frequencies. The displacement in the beta axis is significantly lesser than the displacement in the alpha axis.

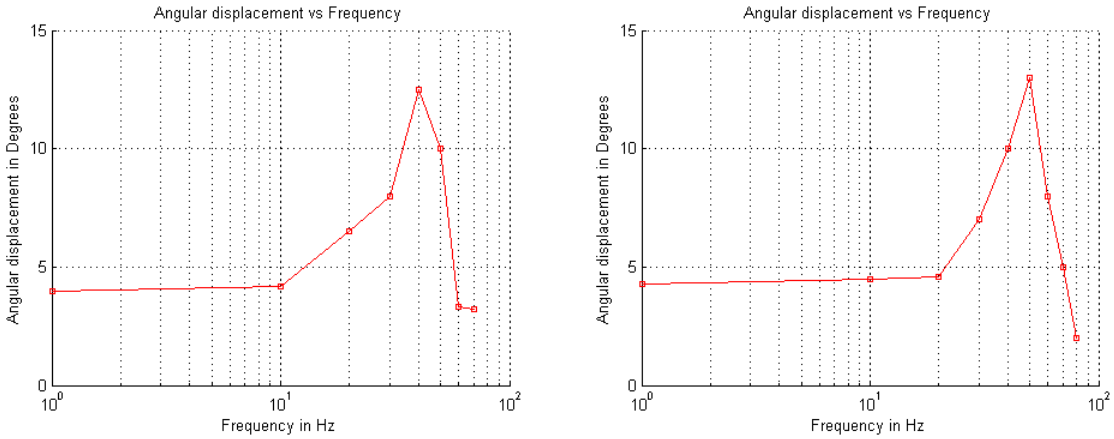


Figure 6-18: Dynamic response of beta axis angular displacement against frequency for the third generation dual axis outer frame inner gimbal straight torsion bar micromirror

# Chapter 7: Summary, Contributions and Future Work

## 7.1 Summary

Micromirror scanners have applications in projection displays, barcode scanners, optical switches and biomedical scanning applications such as confocal microscopy. While the earliest commercial micromirror scanners were based on electrostatic actuation, there is an increasing trend shift towards magnetic actuation of micromirrors. Magnetic actuation has the advantages of large scan angles, low power consumption and remote actuation over electrostatic actuation. These advantages result in the development of better and more efficient micromirror scanners especially in the health care arena where patient safety is a major concern in regards to in vivo diagnostics.

The implementation of magnetic actuation for micromirror scanners involves the selection of the appropriate energy conversion mechanism, the selection of high performance magnetic materials and the determination of a chemically and thermally compatible fabrication process. Although permanent magnetic materials offer the highest magnetic performance, the assimilation of these materials into conventional planar fabrication techniques poses several challenges thermally and chemically. This limitation is overcome by the development of hybrid fabrication techniques. Among the hybrid fabrication techniques replica molding and squeegee coating are most appropriate for the fabrication of polymer composite based micromirrors due to the ease of fabrication and the final yield of the micromolding of small structures. Filler materials in the form of bonded magnetic powders are loaded into polymer matrices inherently have low Young's modulus to aid in high angular displacement for micromirror scanners. Obtaining an optimum volume loading of the magnetic filler material and the polymer matrix provides a high force per energy density magnetic micromirror scanning device.

The Lorentz force actuation mechanism is the preferred energy conversion mechanism for MEMS actuation systems over Coulomb force mechanisms or Faraday force mechanisms where there is the

need for a wound coil. The requirement to generate Lorentz forces is achieved by using planar microcoils that are fabricated using standard PCB fabrication techniques. Spiral planar microcoils provide the highest magnetic flux density among existing planar microcoil designs. Effective spiral planar coil designs with single coil or dual coils can be used for the actuation of the micromirror in single axis or dual axis respectively. The FR-4 substrate doubles as the actuation mechanism and the integration platform for the micromirror scanners.

In this work we show the fabrication and testing of Lorentz force based polymer magnetic mirrors for scanning applications. The mirror structure is composed of a hard-magnetic polymer composite (PDMS + MQFP -12-5) with a reflective surface and no silicon. The advantages of high angular actuation using bonded hard magnetic micropowder, the flexibility of PDMS and standard PCB manufacturing are combined to bring about a micromirror scanner with very high scanning capabilities. Bi-directional actuation of the polymer magnetic mirrors is tested by both static and dynamic experimentation. Maximum angular displacements of ~ 18 degrees (optical) in static mode and ~16 degrees (optical) in dynamic mode are observed. Maximum angular displacement is limited by the maximum current thought the microcoil (1A) and gap between the coil and suspended mirror. Compared to conventional electrostatic mirrors, the polymer magnetic mirrors show far better scanning performance at voltages which are 2 orders lesser. A thin layer of PDMS is micro-pipetted to improve surface roughness and radius of curvature suitable for good reflectivity. For the mirror with surface smoothening PDMS layer, the maximum deflection observed at a 1mm gap was 13. 34 degrees (optical) and at 2 mm was (11.42) degrees (optical). Resonant frequency at 1mm gap was 100 Hz while the resonant frequency at 2mm gap was 80 Hz. The decrease in angular deflection and increase in resonant frequency can be accounted for the increase in mass of the mirror due to the surface smoothening PDMS layer.

Both static and dynamic tests imply that reduced gap spacing between the polymer magnetic mirror and the planar coil increases the angular displacement and scanning performance. Optimum gap spacing is determined by the maximum angular displacement to avoid contact of the mirror with the planar coil. Scan pattern tests determine the effective performance parameters for scanning. The raster length in x-axis was found to be shorter than the y-axis due to the presence of torsion bars in a fixed-fixed beam configuration. Typical raster scanning requires one of the axes to be operating at resonant frequency while the other axis is actuated with a low frequency. The experiments performed illustrate that a low voltage range (static: 14mV to 137mV and dynamic: 176mV to 7.0710 Volts) with moderate current (static: 0.1A to 1A and dynamic: 7.07mA to 141.42mA) can result in high angular scanning capabilities. Owing to the fact that the structural material of the mirror is has low Young's modulus, fatigue and stress induction parameters will be significantly low. Theoretically the maximum static angular displacement should be lower than the maximum dynamic angular displacement due to the actuation at resonant frequency, one of the designs suggest the converse. The reasoning behind this can be attributed to the inter-magnetic forces acting on the central mirror structure causing an attraction force and thereby reducing the angular displacement at resonance. Point by point magnetic field measurements during actuation is necessary to validate the claim by quantification.

## 7.2 Contributions

The major contributions of the work done in this project are

1. The development of a low-cost fabrication process to manufacture hard magnetic polymer micro actuators based on PDMS and isotropic bonded NdFeB micropowder using the squeegee coating micromolding technique.

2. The development of an all polymer magnetic structural micromirror scanner with single and dual axis actuation feature with large scan angle and low power consumption.
3. The development of the testing methodology for the operating conditions of the polymer hard magnetic polymer micromirror scanners
4. The mitigation of the high surface roughness and low radius of curvature problem using a surface modification technique based on the micropipetting of undoped PDMS.
5. The reduction of inter magnetic influence of close proximity magnetic structures by developing a part-PDMS part-polymer composite fabrication technique for dual axis micromirrors.
6. The experimental comparison of single axis no gimbal micromirrors, single axis outer frame micromirrors and dual axis outer frame inner gimbal straight torsion bar in regards to their static and dynamic responses for scanning applications.

The significance of the contributions is discussed in the following sections.

### 7.2.1 Advantages of hybrid fabrication for magnetic microdevices

The utilization of a hybrid fabrication offers the combination of permanent magnetic bonded powders into polymer matrices to form polymer magnetic composites. The processing challenges of conventional magnetic material deposition techniques such as sputtering, evaporation or electrochemical growth is eliminated by the hybrid techniques since the polymer matrix material into which the bonded magnetic powders are embedded can be prepared and deposited in a non-cleanroom lab environment under no thermal processing. Complex geometries and layers can be easily fabricated without the need for photomasks or any chemically selective wet and/or dry etching methods. The release of the deposited composites is simple and requires no chemical treatment. As the magnetization of the polymer magnetic structures is independent of the fabrication, there is no

need to modify or introduce exotic fabrication steps. The yield of MEMS magnetic elements developed through hybrid fabrication is high compared to standard MEMS fabrication which is severely affected by the numerous processing steps involved in standard MEMS fabrication. Specifically, in the development of micromirror scanners, there is no requirement of a substrate layer, a structural layer and an actuation circuit layer. The hybrid fabrication of replica molding and squeegee coating involves the simple steps of mold fabrication, deposition and demolding of the magnetic elements followed by the integration on a standard fabricated PCB that houses the electronics. Further complex geometries with thicker torsion bars and thinner mirror apertures

### 7.2.2 Advantages of polymer magnetic composite micromirror

The major advantage of the polymer composite micromirror is that the entire structural layer of the micromirror is the polymer composite. This offers high flexibility due to the low rigidity of the cured polymer composite resulting in large scan angles at lower power consumptions compared to the silicon based micromirror counterparts. The higher performance of permanent hard magnetic bonded powders that are embedded into the polymer matrix overshadows the force per energy density of conventionally used soft magnetic materials in silicon based MEMS fabrication. Due to the magnetic actuation of the micromirror, there is no pull-in failure mode for the mirror. Reduction in the gap spacing between the mirror and the coil might cause the mirror to have contact with the coil during actuation. This condition does not mitigate the structural or electromagnetic properties of the mirror, although scanning performance is limited. Even in the case that the frame upon which the mirror is integrated is thin enough for the mirror to make contact with the planar microcoil, there is no danger of the destruction of the micromirror, which is often associated with the pull-in of electrostatic micromirrors. If the mirror comes in contact with the mirror in the static attraction mode, the mirror cling on to the planar coil until the current flowing through the coil is turned off. In the dynamic

mode, the actuation of the mirror might be staggered as the attraction cycle of the AC signal will hold the mirror for a longer time than for the repulsion cycle.

### 7.2.3 Advantages of polymer magnetic composite micromirror designs

Each generation of the polymer magnetic micromirror designs have their own inherent advantages. The first generation straight torsion bar micromirror with no gimbal frame offers the highest angular displacement of the three generations of micromirrors. Though this design is the best to obtain maximum displacement, the stability of the integration method was not optimum. In order to mitigate this limitation, the second generation micromirror was designed with a rectangular frame around the torsion bar and mirror to provide structural stability. The improvement on the stability of the mirror was observed during the integration of the mirror although this addition reduced the range of angular displacement. The design of the dual axis micromirror consisted of a two wider edges on the gimbal frame. This provided individual addressing of the alpha and the beta axes in order to perform the scanning. Gimbal frame structures and mirror array structures offer scanning in more than one axis to enable the raster and vector scanning of target samples. The usage of undoped PDMS in the third generation fabrication for the outer frame of the polymer magnetic micromirror increased the scan angle compared to the second generation micromirrors due to the elimination of the intermagnetic interaction between the outer frame and the gimbal structure for the dual axis outer frame, inner gimbal straight torsion bar micromirror.

The device needs to be mounted on a non-magnetic substrate. The FR-4 which houses the planar coils acts as a substrate upon which the supporting frame made of Plexiglas and the polymer magnetic structure is mounted. The planar microcoils used to generate the Lorentz forces for the actuation of the polymer magnetic micromirror were design and positioned to optimize the force per energy density in the attraction or repulsion modes of the mirror. While the first generation of microcoils

designed with rectangular turns generated significant Lorentz forces, the second generation microcoils with spiral turns and thinner trace widths generated comparable forces for the actuation of the micromirror. The usage of thinner trace widths decreases the real estate of the final device and promotes the possibility of more compact designs and micromirror arrays.

## 7.3 Future work

### 7.3.1 Polymer Magnetic Micromirror Arrays

The polymer magnetic micromirror scanners that were designed and fabricated in this work were based on a single mirror aperture. Developing new designs for micromirror arrays would result in better scanning resolution of target samples. In order to achieve micromirror arrays, the dimensions of the torsion bars and mirror apertures is critical due to the effect of inter magnetic influence between the individual elements. Care must also be taken in designing the planar coils that provide the actuation force. The coils cannot be designed in close proximity due to the problem of induction between individual coils. Optimum coil spacing with no induction between adjacent coils will define the dimensions of the torsion bars and mirror apertures.

### 7.3.2 Design optimization of micromirror and planar coils

In order to obtain larger scan angles a suggestion can be made to modify the Plexiglas mold fabrication to have thicker torsion bars and thinner mirror apertures. This can be achieved by the step laser ablation process. The Plexiglas mold that is used for the micromolding of the polymer magnetic composite is laser ablated at higher power and speed settings for the frame and torsion bars and a lower power and speed settings for the mirror aperture. This leads to the formation of thinner mirror apertures that require lesser force per energy density for a given angular displacement. This implies that the microcoils that are required for actuation can be smaller and occupy lesser area on the PCB

substrate. The advantage of laser ablation of the master molds also offers the ability to create serpentine torsion bars. Serpentine torsion bars have been associated with higher deformability when compared with straight torsion bars. However extreme care must be taken during the demolding process as the design is more vulnerable to mechanical tear or breakage.

### 7.3.3 Miniaturization of the polymer magnetic micromirror for scanning applications

### 7.3.4 Control system for the polymer magnetic micromirror

To ensure effective performance of the magnetic mirror scanner, the mirror must be controlled by a closed loop control system. A proposed schematic of the closed loop control system is provided in the Figure 7-1.

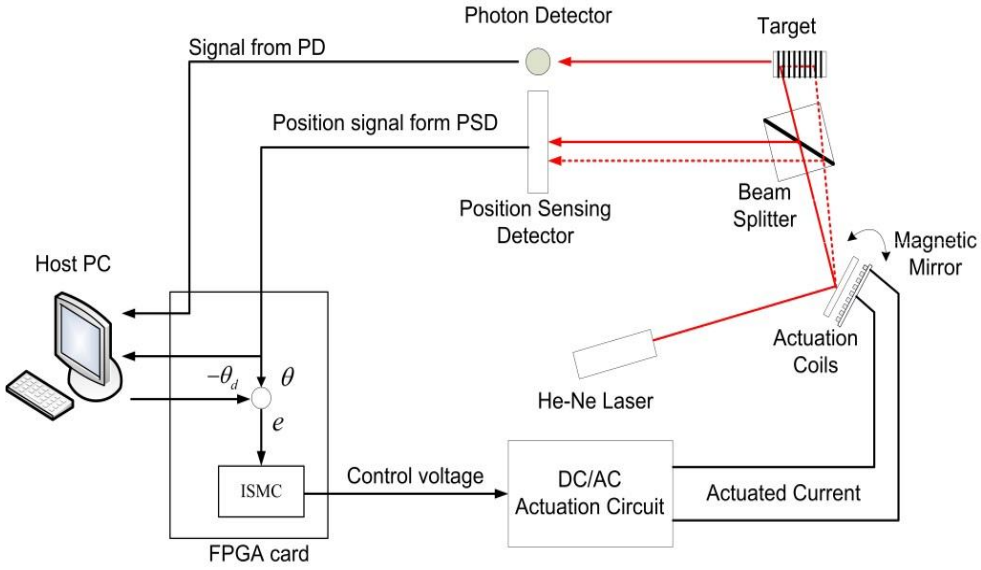


Figure 7-1: Schematic of the control system for the polymer magnetic micromirror

The experimental setup of the system consists of optical, mechanical and electrical blocks. The optical block consists of an illumination source He-Ne laser that is incident on the polymer magnetic

mirror aperture. The reflected beam is guided onto a beam splitter which diverts one beam onto a position sensing detector and the other beam is diverted onto the target sample. The x and y positional information and the light intensity information is fed into an FPGA card that processes the information reconstructs the image in real-time. The FPGA further controls the actuation of the micromirror via feedback using an actuation circuit. The circuit schematic of the actuation circuit is shown in the Figure 7-2.

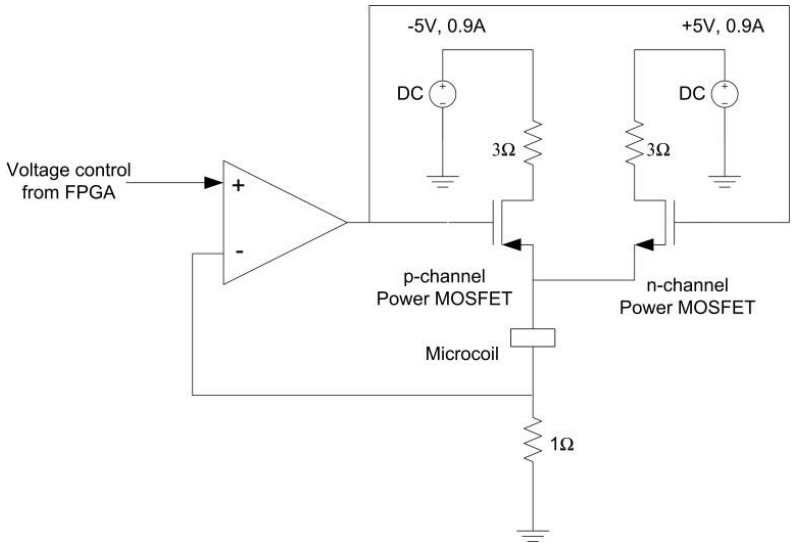


Figure 7-2: The voltage controlled current amplifier circuit

Since the FPGA outputs a very low current and the actuation of the mirror needs a current range of 0.1 to 0.95 A, a voltage controlled current amplifier circuit is designed. An AC sinusoidal AC voltage from the FPGA is fed into this DC circuit to output the required actuation signal to scan a target sample. This system is appropriate for the scanning of target samples either with the single axis micromirrors which provides a line scanning or with the dual axis micromirrors which provide the vector or raster scanning of the target samples with Lissajous scan patters.

# Appendix A

## MQFP-12-5 Isotropic Micropowder Information

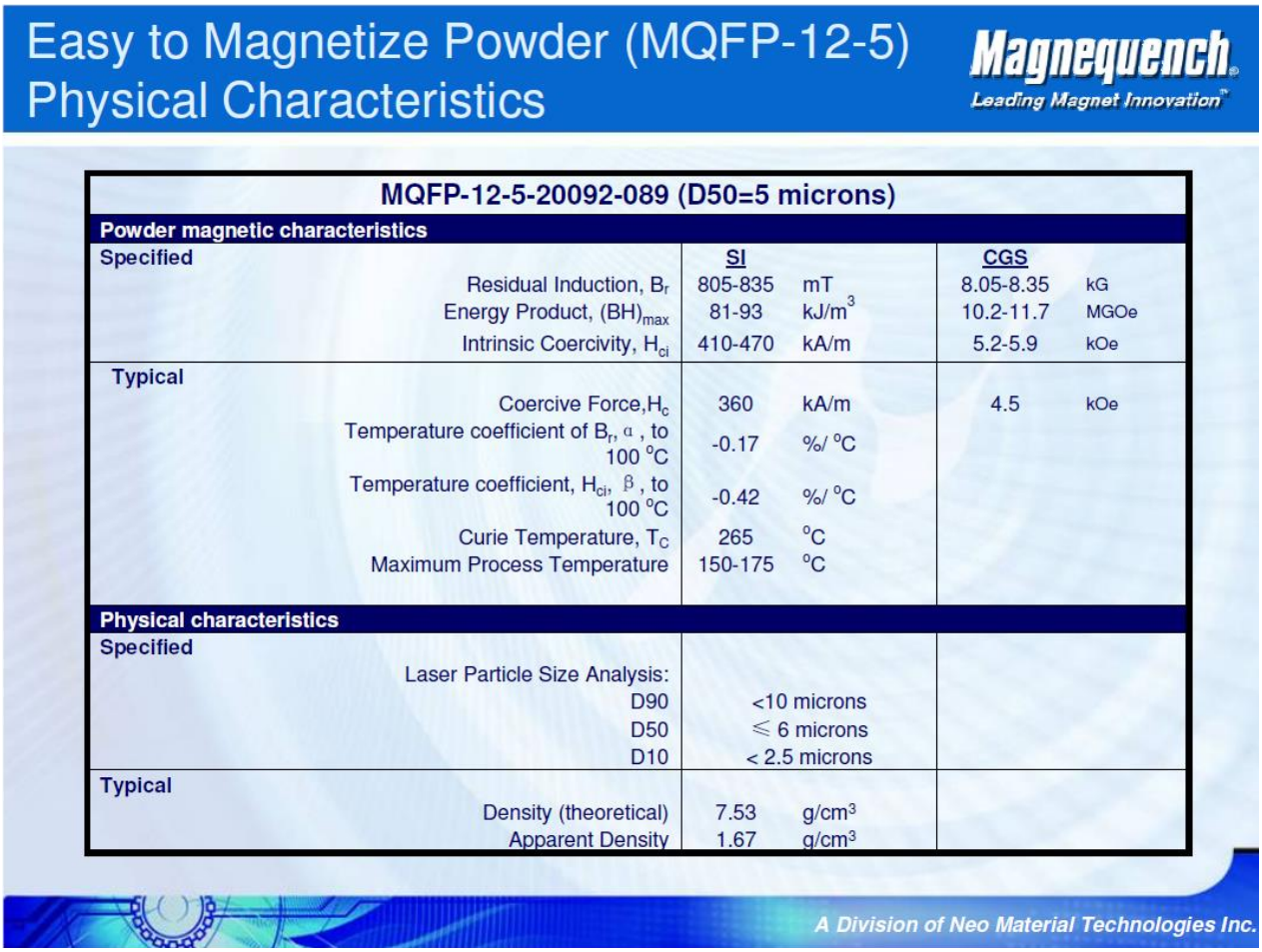

Easy to Magnetize Powder (MQFP-12-5)
Physical Characteristics

Magnequench
Leading Magnet Innovation

| MQFP-12-5-20092-089 (D50=5 microns) | | | | | |
|---|---|---|---|---|---|
| **Powder magnetic characteristics** | | | | | |
| **Specified** | | **SI** | | **CGS** | |
| | Residual Induction, $B_r$ | 805-835 | mT | 8.05-8.35 | kG |
| | Energy Product, $(BH)_{max}$ | 81-93 | $kJ/m^3$ | 10.2-11.7 | MGOe |
| | Intrinsic Coercivity, $H_{ci}$ | 410-470 | kA/m | 5.2-5.9 | kOe |
| **Typical** | | | | | |
| | Coercive Force, $H_c$ | 360 | kA/m | 4.5 | kOe |
| | Temperature coefficient of $B_r$, $\alpha$, to 100 °C | -0.17 | %/ °C | | |
| | Temperature coefficient, $H_{ci}$, $\beta$, to 100 °C | -0.42 | %/ °C | | |
| | Curie Temperature, $T_C$ | 265 | °C | | |
| | Maximum Process Temperature | 150-175 | °C | | |
| **Physical characteristics** | | | | | |
| **Specified** | | | | | |
| | Laser Particle Size Analysis: | | | | |
| | D90 | <10 microns | | | |
| | D50 | ≤ 6 microns | | | |
| | D10 | < 2.5 microns | | | |
| **Typical** | | | | | |
| | Density (theoretical) | 7.53 | $g/cm^3$ | | |
| | Apparent Density | 1.67 | $g/cm^3$ | | |

A Division of Neo Material Technologies Inc.

# Easy to Magnetize Powder (MQFP-12-5) VSM

Magnequench
Leading Magnet Innovation™

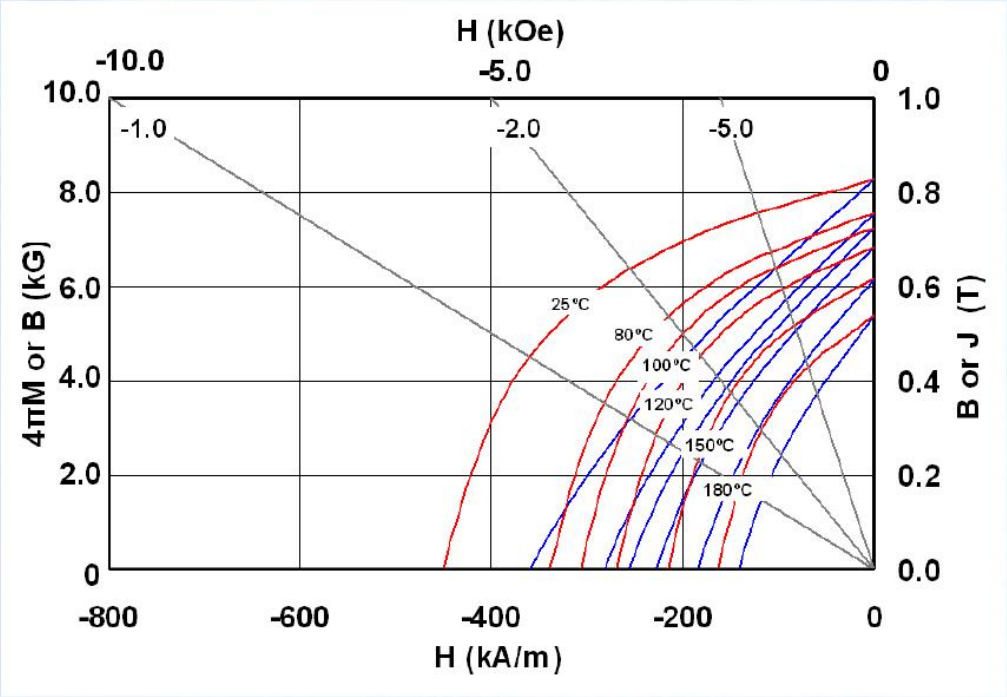


A Division of Neo Material Technologies Inc.

# Appendix B

## GMW 3470 Electromagnet Current versus Magnetic field curves

**GMW Associates**
**Electromagnet Excitation Plot**
**Field Vs Current**

| | | | | | |
|---|---|---|---|---|---|
| Contract No: | | Page: 2 of 3 | | Date: | Sept 22, 95 |
| Customer: | | | | Engr: | G.Douglas |
| Model: | 3470 | Power Supply: | | Set Current: | |
| Serial No: | 52 | Serial No: | | Target Field: | |
| Pole Face: | 20 | Position: | X=0, Y=0, Z=0 | | |
| Serial No: | None | Notes: | Coil position set to minimum gap | | |
| Pole Gap: | As per table below | | | | |
| Pole Spacers: | None | | | | |

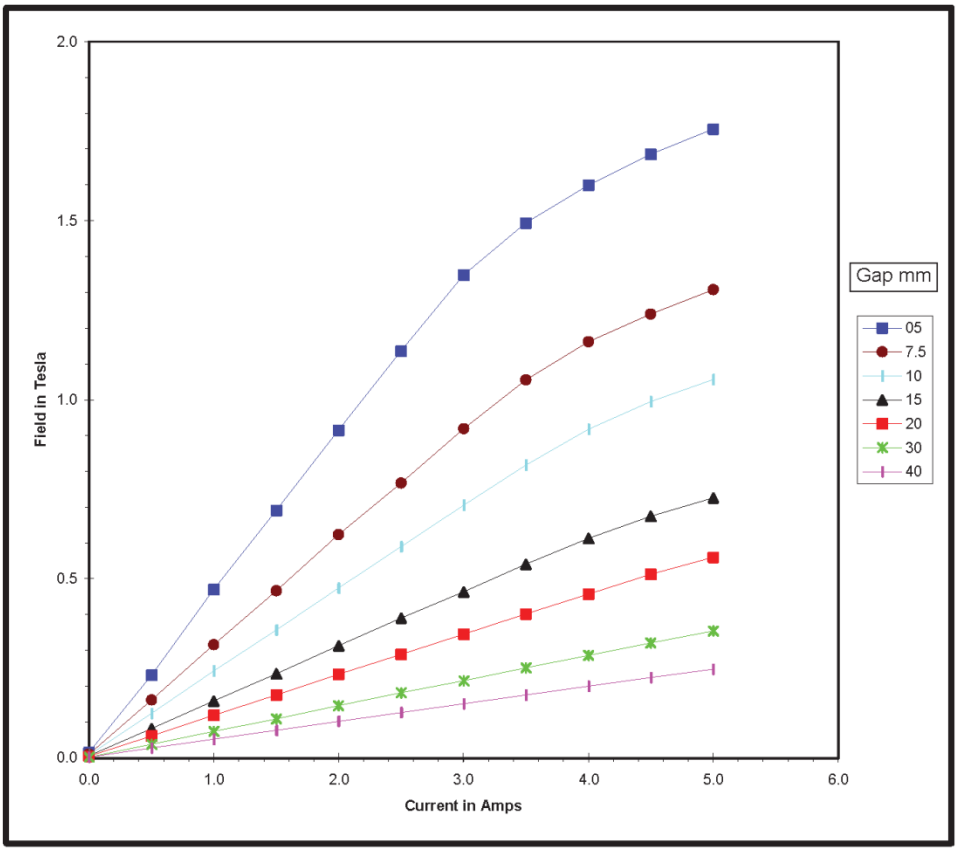


Filename: 3470 Ex 20-05-40.xls

# Bibliography


[1] J. Kim, H. Choo, L. Lin and R. S. Muller, Microfabricated torsional actuators using self-aligned plastic deformation of silicon, *J. Microelectromech. Syst.*, **15**, 553–562 (2006)

[2] T. Kawabata, M. Ikeda, H. Goto, M. Matsumoto and Y. Tsuneji, The 2-Dimentional micro scanner integrated with PZT thin film actuator, *Proceedings of the IEEE International Conference on Solid-State Sens. Actuators*, **1**, 339-342, (1997)

[3] Y. Eun and J. Kim, 1-DOF and 2-DOF torsional micromirrors driven by in-plane thermal actuators, *4th Asia-Pacific Conf. on Transducers and Micro/Nano Technologies 2008*, APCOT 2008

[4] H. Miyajima, N. Asaoka, M. Arima, Y. Minamoto, K. Murakami, K. Tokuda and K. Matsumoto, A durable,shock-resistant electromagnetic optical scanner with polyimide-based hinges, *J.Microelectromech. Syst.*, **10**, 418–424, (2001)

[5] R. Osiander, S.A. Ecelberger, R.B. Givens, D.K. Wickenden, J.C. Murphy, J.C. and T. J. Kistenmacher, A microelectromechanical-based magnetostrictive magnetometer, *Applied Physics Letters* , **69**, 2930-2931 (1996)

[6] Fukuta, Y.; Chapuis, Y.A.; Mita, Y.; Fujita, H., A MEMS array for pneumatic conveyor and its control based on distributed system, *Micro Electro Mechanical Systems, 2005. MEMS 2005. 18th IEEE International Conference on*, **30,** 40-43, (2005)

[7] M. De Volder, F. Ceyssens, D. Reynaerts, and R. Puers, *Micro Electro Mechanical Systems, 2009. MEMS 2009. IEEE 22nd International Conference on*, (2009).

[8] H Guckel, K J Skrobis, T R Christenson, J Klein, S Han, B Choi, E G Lovell and T W Chapman , Fabrication and testing of the planar magnetic micromotor, *J. Micromech. Microeng.*, **1** 135 (1991).

[9] B. Wagner and W.Benecke, Magnetically driven micro-actuators: Design considerations in Microsystem Technologies *90, H. Reichl, Ed. Berlin, Germany: Springer-Verlag,* 838, (1990)

[10] W. Benecke, Scaling behaviour of microactuators, *in Proc. ACTUATOR, Bermen, Germany*, 19-24, (1994)

[11] H. Guckel et al., Fabrication and testing of the planar magnetic micro-motor, *J. Micromech. Microeng.*, **1**, 135-138, (1991)

[12] I. J. Busch-Vishniac, The case for magnetically driven microactuators, *Sensors and actuators A*, **3**, 207 – 220, (1992)

[13] O. Cugat, J. Delamare and G. Reyne, Magnetic Micro-Actuators and Systems (MAGMAS), *IEEE Transactions on Magnets*, **39**, (5), 3607-3612, (2003)

[14] C. H. Ahn, Y. J. Kim and M. G. Allen, A planar variable reluctance magnetic micromotor with fully integrated stator and coils, *J.Microelectromech. syst.*, **2**, 165-173, (1993)

[15] A. Cao et al., Bi-directional electrothermal electromagnetic actuators, *J.Micromech. Microeng.*, **17**, 975-982, (2007)

[16] K. Fisher et al., A latching bistable optical fiber switch combining LIGA technology with micro-machined permanent magnets, *in Proc. Transducers*, (2001)

[17] M. Capanu, J. G. Boyd and P. J. Hesketh, Design, fabrication and testing of bistable elctromagnetically actuated microvalve, *J.Microelctromech.Syst.*, **9**, 181-189, (2002)

[18] M. Ruan, J. Shen and C. B. Wheeler, Latching micromagnetic relays, *J.MEMS*, **10** (4), 511-517, (2001)

[19] T. Iizuka and H. Fujita, Precise positioning of a micro-conveyer based on superconducting magnetic levitation, *in Proc. IEEE Int. Symp. Micromechatronics and Human Science*, 131-135, (1997)

[20] H. Hashimoto et al., Thermally controlled magnetization actuator (TCMA) using thermosensitive magnetic materials, *in Proc. MEMS*, 108, (1994)

[21] H Nagaoka et al., Micro-magnetic alloy tubes for switching and splicing single mode fibers, *in Proc. MEMS*, 86, (1991)

[22] Q. Zhou, P. Ben-Tzvi, A Iqbal and D. Fan, Design, analysis and optimization of magnetic microactuators, *IMECE2009-12765*, 1-10, (2009)

[23] T. Ueno, J. Qiu and J. Tani, Self-sensing magnetic force control by composite element of a giant magnetostrictive and piezoelectric materials, *in Proc. Movic, Saitama, Japan*, (2002)

[24] S. Forouzanfar Thesis: Micro-electro-thermo-magnetic actuators for MEMS applications, 2006

[25] B. Bae, N. Kim, H. Kee, S. Kim, Y. Lee, S. Lee and K. Park, Feasibility test of an electromagnetically driven valve actuator for glaucoma treatment, *J.Microelectromech. Syst.*, **11**, 344-354, (2002)

[26] H. J. Cho and C. H. Ahn, A bidirectional magnetic microactuator using electroplated permanent magnet array, *J. Microelectromech. Syst.*, **11**, 78-84, (2002)

[27] J. Groom, Design considerations for air core magnetic actuator, *Tech. Memorandum 104229, NASA*, (1992)

[28] T.-S. Chin, Permanent magnet films for applications in microelectromechanical systems, *J. Magn. Magn. Mater*., **209**, (1–3), 75-79, (2000)

[29] B. D. Cullity and C. D. Graham, *Introduction to Magnetic Materials. London*, U.K.: Oxford Univ. Press, (2008)

[30] R. J. Parker, *Advances in permanent magnetism* New York, USA, Wiley Interscience publication, (1990)

[31] R. Skomski and J. M. D. Coey, *Permanent Magnetism* Bristol, U.K.: Inst. Phys. Pub., (1999)

[32] C. Pu, S. Park, P. B. Chu, S. Lee, M. Tsai, D. Peale, N. H. Bonadeo, and I. Brener, Electrostatic actuation of three-dimensional MEMS mirrors using sidewall electrodes, IEEE Journal of Selected Topics in Quantum Electronics, **10**, (3), 472-477, (2004)

[33] H. Miyajima, N. Asaoka, T. Isokawa, M. Ogata, Y. Aoki, M. Imai, O. Fujimori, M. Katashiro and K. Matsumoto, A MEMS electromagnetic optical scanner for a commercial confocal laser scanning microscope, *Journal of MEMS*, **12**, 243-251, (2003)

[34] J. Singh, T. Gan, A. Agarwal, Mohanraj, and S. Liw, 3D free space thermally actuated micromirror device, *Sens. Actuators A*, **123**, 468-475, (2005)

[35] A. Garnier, T. Bourouinna, H. Fujita, E. Orsier, T. Masuzawa, T. Hiramoto, J. Peuzin, A Fast, Robust and Simple 2-D Micro-Optical Scanner Based on Contactless Magnetostrictive

Actuation, *The 13th IEEE International Micro Electro Mechanical Systems Conference (MEMS 2000), Miyazaki, Japan*, 715-720, (2000)

[36] T. Bourouina, E. Lebrasseur, G. Reyne, A Debray, H. Fujita, A. Ludwig, E. Quandt, H. Muro, T. Oki, and A. Asaoka, Integration of Two Degree-of-Freedom Magnetostrictive Actuation and Piezoresistive Detection: Application to a Two- Dimensional Optical Scanner, *IEEE J. Microelectromech. Syst.*, **11**, (4), 355-361, (2002)

[37] T. Kawabata, M. Ikeda, H. Goto, M. Matsumoto and Y. Tsuneji, The 2-Dimentional micro scanner integrated with PZT thin film actuator, *Proceedings of the IEEE International Conference on Solid-State Sens. Actuators*, **1**, 339-342, (1997)

[38] P. Krulevitch, A.P. Lee, P.B. Ramsey, J.C. Trevino, J. Hamilton and M.A.M.A. Northrup, Thin film shape-memory alloy micro-actuators, *J. MEMS*, **5**, 270–282, (1996)

[39] M. Volder and D. Reynaerts, Pneumatic and hydraulic microactuators: a review, *J. Micromech. Microeng.*, **20** 043001, (2010)

[40] N. Asada, H. Matsuki, K. Minami and M. Esashi, M., Silicon Micromachined Two-Dimensional Galvano Optical Scanner, *IEEE Trans. on Magnetics*, **30**, (6), 4647-4649, (1994)

[41] R. Miller and Y. Tai., Electromagnetic MEMS Scanning Mirrors, *Optical Engineering*, **36**, (5), 1399-1407, (1997)

[42] J. W. Judy and R. S. Muller, Magnetically actuated, addressable microstructures, *J. Microelectromech. Syst*., **6**, 249-256, (1997)

[43] H. Miyajima, N. Asoaka, T. Isokawa, M. Ogata, Y. Aoki, M. Imai, O. Fujimori, M. Katashiro and K. Matsumoto, Product Development of a MEMS Optical Scanner for a Laser Scanning Microscope, *The 15th IEEE International Micro Electro Mechanical Systems Conference (MEMS 2002)*, 552-555, (2002)

[44] S. Ahn and Y. Kim, Galvanometric silicon scanning mirror with 2 DOF, *Optical MEMs*, 2002, *Conference Digest 2002, IEEE/LEOS International Conference 2002*, 87-88, (2002)

[45] R. A. Conant, J. T. Nee, K. Y. Lau and R. S. Muller, Dynamic Deformation of Scanning Mirrors, *IEEE/LEOS International Conference on Optical MEMS*, 49-50, (2000)

[46] D. W. Wine, M. P. Helsel, L. Jenkins, H. Urey and T. D. Osborn, Performance of a Biaxial MEMS-Based Scanner for Microdisplay Applications, *Proceedings of the SPIE, MOEMS and Miniaturized Systems*, 186-196, (2000)

[47] J. S. Bintoro, A. D. Papania, Y. H. Berthelot and P. J. Hesketh, Bidirectional electromagnetic microactuator with microcoil fabricated on a single wafer: static characteristics of membrane displacements," *J.Micromech, Microeng*, **15**, 1378-1388, (2005)

[48] J. J. Bernstein, T. W. Lee, F. J. Rogomentich and M. G. Bancu, K. H. Kim, G. Maguluri, B. E. Bouma and J. F. DeBoer, Scanning OCT endoscope with 2-axis magnetic micromirror, *Endoscopic Microscopy II, Proc*., **6432**, 1-10, (2007)

[49] Z cui et al., Fabrication of micromirror-based magnetic sensor, *J. Physics*: **76**, 1-5, (2007)

[50] C. Ji et al., Two dimensional electromagnetic scanning micromirror actuated by radial magnetic field, *J. Microelectromech. Syst*., **16** (4), 989-996, (2007)

[51] H. Urey, S. Holmstrom and A. D. Yalcinkaya, Electromagnetically Actuated FR4 Scanners, *IEE Photonice Technology Letters*, **20**, (1), 30 – 32, (2008)

[52] I. Cho and E. Yoon, A low-voltage three-axis electromagnetically actuated micromirror for fine alignment among optical devices, *J. Micromech. Microeng.*, **19**, 1-8, (2009)

[53] T. Lai and C. Tsou, A novel electromagnetic microactuator with lateral magneto-static force for scanning micromirror device, *Transducers*, 542-545, (2011)

[54] Arnold Magnetic Technologies, [Online]. Available: http://www.arnoldmagnetics.com

[55] M. Drak and L.A, Dobrzanski, Hard magnetic materials Nd-Fe-B/Fe with epoxy resin matrix, *Journal of achievements in materials and manufacturing engineering*, **24**, 2, 63-66, (2007)

[56] W. F. Liu, S. Suzuki, D. S. Li, and K. Machida, Magnetic properties of Fe-Pt thick-films magnets prepared by RF sputtering, *J. Magn. Magn. Mater*., **302**, 1,201-205, (2006)

[57] F. Ruiyi, F. Qingqing, Z. Sheng, P. Chubing, and Dai Daosheng, New permanent magnetic MnBiDy alloy films, *Journal of Applied Physics*, **76**, 10, 6769, (1994)

[58] M. Nakano, S. Shibata, T. Yanai, and H. Fukunaga, Anisotropic properties in Fe-Pt thick film magnets, *J. Appl. Phys*., **105**, 7, 07A729, (2009)

[59] F. J. Cadieu, L. Chen, and B. Li, Enhanced magnetic properties of nanophase $SmCo_5$ film dispersions, *IEEE Trans. Magn*., **37**, 4, 2570-2572, (2001)

[60] F. M. F. Rhen, G. Hinds, C. O'Reilly, and J. M. D. Coey, Electrodeposited FePt films, *IEEE Trans. Magn*., **39**, 5, (2003)

[61] K. Leistner, J. Thomas, H. Schlörb, M. Weisheit, L. Schultz, and F. Fähler, Highly coercive electrodeposited FePt films by postannealing in hydrogen, *Appl. Phys. Lett*., **85**, 16, 3498, (2004)

[62] S. Thongmee, J. Ding, J. Y. Lin, D. J. Blackwood, J. B. Yi, and J. H. Yin, FePt films fabricated by electrodeposition, *J. Appl. Phys*., **101**, 9, 09K519, (2007)

[63] O. Berkh, Y. Rosenberg, Y. S. Diamand, and E. Gileadi, Electrodeposited Near-Equiatomic CoPt Thick Films, *Electrochem. Solid-State Lett*., **11**, 4, D38-D41, (2008)

[64] C. Prados, A. Hernando, G. C. Hadjipanayis, and J. M. Gonzalez, Coercivity analysis in Sm-Co thin films, *J. Appl. Phys*., **85**, 8, 6148, (1999)

[65] T. Budde and H. H. Gatzen, Thin film SmCo magnets for use in electromagnetic microactuators, *J. Appl. Phys*., **99**, 8, 08N304, (2006)

[66] D.P. Arnold, N. Wang, Permanent magnets for MEMS, *Microelectromechanical Systems, Journal of*, **18**, 6, 1255-1266, (2009)

[67] X-M. Zhao, P.S. Smith, S.J. Waldman, G.M Whitesides, and M. Prentiss, Demonstration of waveguide couplers fabricated using microtransfer molding, *Applied Physics Letters*, **71**, 8, 1017, (1997)

[68] K. Kobayashi and K. Ikuta, Development of free-surface microstereolithography with ultra-high resolution to fabricate hybrid 3-D microdevices, *Micro-NanoMechatronics and Human Science, 2005 IEEE International Symposium on*, 273-278, (2005)

[69] W. Voit, W. Zapka, L. Belova, and K.V. Rao, Application of inkjet technology for the deposition of magnetic nanoparticles to form micro-scale structures, *Science, Measurement and Technology, IEE Proceedings*, **150**, 5, 252-256, (2003)

[70] M. Khoo and L. Chang, A novel micromachined magnetic membrane microfluid pump, *Engineering in Medicine and Biology Society, 2000. Proceedings of the 22nd Annual International Conference of the IEEE,* **3**, 2394-2397, (2000)

[71] Gwent Group Advanced Material Systems, [Online]. Available: http://www.gwent.org/gem_screen_printing.html

[72] Z.C Yuan, A.J Williams, T.C Shields, S Blackburn, C.B Ponton, J.S Abell and I.R Harris, The production of Sr hexaferrite thick films by screen printing, *Journal of Magnetism and Magnetic Materials*, **247**, 3, 257-269, (2002)

[73] L.K. Lagorce and M.G. Allen, Magnetic and mechanical properties of micromachined strontium ferrite/polyimide composites, *Microelectromechanical Systems, Journal of*, **6**, 4, 307-312, (1997)

[74] L.K. Lagorce, O. Brand and M.G. Allen, Magnetic microactuators based on polymer magnets, *IEEE/ASME J. Microelectromech. Syst*. **8**, 2-9, (1999)

[75] H.J. Cho and C.H. Ahn, Microscale resin-bonded permanent magnets for magnetic micro-electro-mechanical systems applications, *Journal of Applied Physics*, **93**, 8674-8676, (2003)

[76] M. Feldmann and S. Buttgenbach, Novel microrobots and micromotors using Lorentz force driven linear microactuators based on polymer magnets, *Magnetics, IEEE Transactions on,* **43**, 10, 3891-3895 (2007)

[77] M. Feldmann and S. Buttgenbach, A novel monolithically fabricated Lorentz force actuator using polymer magnets, *Magnetics Conference, 2005. INTERMAG Asia 2005. Digests of the IEEE International*, 1955-1956, (2005)

[78] C. Ruffert, M. Feldmann, S. Buttgenbach, and H.H. Gatzen, Fabrication of functional components for electromagnetic microactuators, *Microsystem Technologies,* **12**, (7), 670-675, (2006)

[79] Y. I. Rozenberg, Y. Rosenberg, V. Krylov, G. Belitsky and Y. S.-Diamand, Resin-bonded permanent magnetic films with out-of-plane magnetization for MEMS applications, *Journal of Magnetism and Magnetic Materials*, **305**, 2, 357-360, (2006)

[80] R. Delille, M.G. Urdaneta, S.J. Moseley and E. Smela, Benchtop Polymer MEMS, *Microelectromechanical Systems, Journal of*, **15**, 5, 1108-1120, (2006)

[81] B.M. Dutoit, P.-A. Besse, H. Blanchard, L Guérin and R.S. Popovic, High performance micromachined $Sm_2Co_{17}$ polymer bonded magnets, *Sensors and Actuators A: Physical* **77,** **(**3), 178-182, **(**1999)

[82] B. Pawlowski and J. Töpfer, Permanent magnetic NdFeB thick films, *Journal of Materials Science*, **39**, (4), 1321-1324, (2004)

[83] B. Pawlowski, S. Schwarzer, A. Rahmig and J. Töpfer, NdFeB thick films prepared by tape casting, *Journal of Magnetism and Magnetic Materials*, **265**, (3), 337-344, (2003)

[84] W. Wang, Z. Yao, J.C. Chen and J. Fang, Composite elastic magnet films with hard magnetic feature, *J. Micromech. Microeng.* **14**, (10), 1321-1327, **(**2004)

[85] J.J. Romero, R. Sastre, F.J. Palomares, F. Pigazo, R. Cuadrado, F. Cebollada, A. Hernando and J.M. González, Polymer bonded anisotropic thick hard magnetic films for micromotors/microgenerators, *Journal of Iron and Steel Research, International*, **13**, (1), 240-251, (2006)

[86] E. Pina, F.J. Palomares, M.A. García, F. Cebollada, A. de Hoyos, J.J. Romero, A. Hernando and J.M. González, Coercivity in SmCo hard magnetic films for MEMS applications, *Journal of Magnetism and Magnetic Materials*, **290–291**, (2), 1234-1236, (2005)

[87] E. Pina, M.A. García, I. Carabias, F.J. Palomares, F. Cebollada, A. De Hoyos, R. Almazán, M.I. Verdú, M.T. Montojo, G. Vergara, A. Hernando and J.M. González, Temperature dependence of the hysteretic properties in SmCo films, *Journal of Magnetism and Magnetic Materials*, **272-276,** (1), E833-E835, (2004)

[88] N. Wang, B.J. Bowers, and D.P. Arnold, Wax-bonded NdFeB micromagnets for microelectromechanical systems applications, *Journal of Applied Physics* **103 (07)**, 109, (2008)

[89] B.J. Bowers, J.S. Agashe and D.P. Arnold, A method to form bonded micromagnets embedded in silicon, *Transducers '07: 14th Int. Conf. on Solid-State Sensors, Actuators, and Micro-Systems (Lyon, France)*, 1585-1588, (2007).

[90] T.S. Yang, N. Wang and D.P. Arnold, Fabrication and characterization of parylene-bonded Nd-Fe-B powder micromagnets, *J. Appl. Phys.* **109,** (7), 07A753-07A753-3, (2011)

[91] O.D. Oniku and D.P. Arnold, High-energy-density permanent micromagnets formed from heterogeneous magnetic powder mixtures, *Proc. 25th Int. Conf. on Micro Electro Mechanical Systems (Paris, France)*, 436-439, (2012)

[92] A. Khosla, J.L. Korčok, B.L. Gray, D.B. Leznoff, J. Herchenroeder, D. Miller and Z. Chen, Fabrication of UV-micro-patternable permanent micro magnets for lab on a chip and MEMS, *Proc. SPIE 7646, Nanosensors, Biosensors, and Info-Tech Sensors and Systems*, 76461L-1-7, (2010)

[93] D.D. Hilbich, A. Khosla, B.L. Gray, and L. Shannon, Bidirectional magnetic microactuators for uTAS, *Proc. SPIE 7929, Microfluidics, BioMEMS, and Medical Microsystems IX*, 79290H-1-11, (2011)

[94] N. Weber N, D. Hertkorn, H. Zappe and A. Seifert, Polymer/Silicon hard magnetic micromirrors, *J Microlectromech. Syst.* **21**, (5), 1098-1106, (2012)

[95] Y. I. Rozenberg, Y. Rosenberg, V. Krylov, G. Belitsky and Y. S.-Diamand, Resin-bonded permanent magnetic films with out-of-plane magnetization for MEMS applications, *Journal of Magnetism and Magnetic Materials*, **305**, 2, 357-360, (2006)

[96] J.M. Coey and K. O'Donnell, New bonded magnetic materials, *J. Appl. Phys*., **81,** 8, 4810, (1997)

[97] A.H.M Andreasen and J. Anderson. Uber die Beziehung zwischen Kornabstufung und Zwischenraum in Produckten aus losen Kornern (mit einigen Experimenten) *Kolloid-Z*, **50**, 217-228 (1930).

[98] SU-8 2000 Permanent Epoxy Resists, [Online]. Available: http://www.microchem.com/Prod-SU82000.htm

[99] Sylgard® 184 Silicone elastomer kit, [Online]. Available: http://www.dowcorning.com/applications/search/default.aspx?R=131EN

[100] Isotropic – Small particle size grades (MQFP), [Online]. Available: http://www.mqitechnology.com/isotropic-small-particle-size-grades.jsp

[101] Generic standard on printed board design, [Online]. Available: http://www.ipc.org/toc/ipc-2221a.pdf

[102] GMW dipole electromagnet, 45 mm, 3470, [Online]. Available: http://www.gmw.com/electromagnets/dipole/3470/3470.html

[103] Universal Laser Systems VLS3.50, [Online]. Available: http://www.ulsinc.ca/products/vls350/

[104] MyRO Electronic Control Devices Inc., [Online]. Available: http://www.myropcb.com/

[105] Senis magnetic field transducers, Three-axis, [Online]. Available: http://www.gmw.com/magnetic_measurements/Senis/3-axis.html

[106] Instron micro testers models 5547 and 5548, [Online]. Available: *www.instron.com/wa/library/StreamFile.aspx?doc=809*

[107] ASTM STP1120 Composite materials: Testing and Design (Tenth Volume), [Online]. Available: http://www.astm.org/DIGITAL_LIBRARY/STP/SOURCE_PAGES/STP1120.htm

[108] T. Yoshizawa, *Handbook of optical metrology*, Boca Raton: CRC Press (2009)

[109] Wyko NT1100 Optical Profiling System, [Online]. Available: http://www.veeco.com/pdfs/datasheets/NT1100%20RevA5%20Final_394.pdf

[110] National Instruments Vision Builder for Automated Inspection (AI), [Online]. Available: http://www.ni.com/vision/software/vbai/